On the Electrochemical Discharges for Nanoparticles Synthesis

Anis Allagui

A Thesis
In the Department of
Mechanical and Industrial Engineering

Presented in Partial Fulfillment of the Requirements
For the Degree of Doctor of Philosophy (Mechanical Engineering) at
Concordia University
Montreal, Quebec, Canada

Concordia University
School of Graduate Studies

This is to certify that the thesis prepared

By: Anis Allagui

Entitled: On the Electrochemical Discharges for Nanoparticles Synthesis

and submitted in partial fulfillment of the requirements for the degree of

Doctor of Philosophy (Mechanical Engineering)

complies with the regulations of the University and meets the accepted standards with respect to originality and quality.

Signed by the final examining committee:

Dr. L. Rodrigues	______________________	Chair
Dr. A. Dhirani	______________________	External Examiner
Dr. C. DeWolf	______________________	External to Program
Dr. M. Packirisamy	______________________	Examiner
Dr. P. Wood-Adams	______________________	Examiner
Dr. Rolf Wüthrich	______________________	Thesis Supervisor

Approved by

____

Chair of Department or Graduate Program Director

____

Dean of Faculty

Abstract

On the Electrochemical Discharges for Nanoparticles Synthesis

Anis Allagui, Ph.D

Concordia University, 2011

The electrochemical discharge phenomenon is a high current density electrochemical process with intrinsic physicochemical properties suitable for the synthesis of nano-sized materials. At this mesoscopic range of physics, matter takes on drastically new properties and activities different from its bulk counterpart, which explains the dynamic research activity in building nano-structures. This thesis focuses on the macroscopic and microscopic descriptions of the electrochemical discharges and on the application of the phenomenon for the synthesis of nanoparticles.

It starts by establishing the leading variables to control the process from the perspective of entropy production. The nonequilibrium thermodynamics analysis is successfully adapted to the process to extract a global expression for its entropy balance. Based on the excess entropy production in the system, the conjugated thermal and electrochemical fluxes and forces are the hierarchically top constraints affecting the process and its stability. This approach is supported by experimental evidences on the dynamic analysis of the electrochemical system which is performed through a designed wavelet-based signal processing algorithm. The gas film, covering and insulating the electrode during the process from the rest of the solution, has a life-time and building-time which are respectively an increasing and decreasing positive definite functions of the applied terminal voltage and the bulk temperature.

With the successful synthesis of nickel and platinum nanoparticles, characterized morphologically, chemically and electrochemically, the second part of this thesis presents a comprehensive methodological procedure to apply the process in nanoparticles manufacturing. Two synthesis mechanisms of nano-materials by the electrochemical discharges and supported by the experiment are treated in detail. The first one involves the continuous competition of direct reduction of metal ions by the hydrated electron, e^{-}_{aq}, the hydrogen radical, $H^{\cdot}$, and secondary generated species, versus the back reaction of oxidation by the hydroxide radical $OH^{\cdot}$. The second mechanism is based on electrode sputtering physics by which the positively charged ions are accelerated in the gas film gap and strike the outermost atoms at the electrode surface to be diffused afterwards in the bulk solution. Zero-valent atoms will then undergo time-dependent nucleation and crystal growth processes to form colloidal suspension of nano-sized particles in the bulk solution. The performances of the synthesized nickel oxide nano-materials by electrochemical discharges as supercapacitors for energy storage applications are investigated and discussed. It is shown that the pseudocapacitance behavior and consequently the energy and power densities are size-dependent.

Acknowledgements

بسم الله الرّحمٰن الرّحيم
الحمد لله و الشّكر لله. ازكَى صلَاتي و سلَامي علَى رسول الله.

Many people have helped me in the course of my research, and any merit on its behalf is in large measure due to them. First and foremost, I gladly acknowledge my debt to Rolf Wüthrich who taught me the little I know in the fields of electrochemistry and nanotechnology. Without his constant friendship, generous encouragement and concise advice over those years, this original thesis would never have been completed.

Additionally, I am grateful to a host of correspondents whose help should be acknowledged; in particular, to Elena Baranova, because she kindly gave me much information and suggestions relating to my research direction. I would also especially like to recognize Paula Wood-Adams, Mamoun Medraj and Lyes Kadem, for permitting me to use their facilities and equipment, in addition for giving me helpful critics and recommendations. I am also thankful for the opportunity to have met and worked with many talented and friendly researchers and students over those years, such as Mohamed, Yun, Mazen, Mohsen, Imam, Birming, Malek, Tohid, Kishor, Andrew, Maniya, Zahra, Farzad, Marie-Paule, Jean-Briac, Jong Min, and many others.

Last but not least, many thanks are due to some very special people in my life. First, to my parents, Mohamed and Sihem, whose infinite generosity and profound admiration for research and science offered a great deal of support, while overcoming most of the difficulties encountered during this work. Finally, special thanks go to a special person, to Bevin, and to her continuous and growing support since the first day I had her in my life.

Anis Allagui

Dedicated with much love, affection and gratitude
to my father, my mother and to my wife.

Table of Contents

List of Figures

List of Tables

List of Symbols

Latin Symbols

a	Scaling number
c	Speed of light
c_k	Mass fraction of component k
c_{sc}	Specific capacitance
d	Thickness
d_e	Energy per unit mass
d_p	Power per unit mass
e	Total energy per unit mass
f	Frequency
f_{ji}^{α}	Transition probability
g_i^{α}	Degeneracy factor
$g_{p,a}$	Functional for wavelet analysis of position p and scaling number a
h_k	Enthalpy per unit mass of component k
i	Electric current density
k	Heat conductivity constant
k_B	Boltzmann constant
m_k	Total mass of component k
n_c	Number of molecules in critical size nucleus

n_g	Number of moles of gas
n_l	Number of moles of liquid
n_s	Normalized cluster number
p	Position or translation
p_c	Percolation threshold
r	Radius
r_c	Critical radius
s	Entropy per unit mass
s_r	Voltage scan rate
t_0	Time of perturbation
t_e	Time of end of perturbation
u	Total internal energy per unit mass
v	Specific volume
$\mathbf{v}$	Barycentric velocity
$\mathbf{v}_k$	Velocity of component k
z	Valence number
z_k	Charge per unit mass of component k
A	Area
B	Experimental constant
$\mathbf{B}$	Magnetic field
C	Experimental constant
C_Φ	Pseudocapacitance
C_{dl}	Electric double-layer capacitance
C_p	Heat capacity
D	Diffusion coefficient
E	Total energy
$\mathbf{E}$	Electric field

E°	Standard potential
E_F	Fermi energy
E_j^{α}	Energy at level j
F	Faraday constant
$\mathbf{F}_E$	Electrostatic or coulombic forces
$\mathbf{F}_M$	Magnetic dipole-dipole forces
$\mathbf{F}_S$	Steric forces
$\mathbf{F}_W$	van der Waal forces
$\mathbf{F}_k$	Force per unit mass acting of component k
G	Gibbs energy function
H_v	Heat of vaporization
I_C	Critical current
I_{ji}^{α}	Relative intensity
J_0	Rate of nucleation
$\mathbf{J}_e$	Total energy flux
$\mathbf{J}_k$	Diffusion flux per unit mass of component k
$\mathbf{J}_q$	Total heat flux
$\mathbf{J}_q'$	Total measurable heat flux
$\mathbf{J}_{s,tot}$	Total entropy flux per unit mass
K	Shape factor
M	Molar mass
N	Number of valence electrons
N_k	Number of moles of component k
P	Pressure
Q	Total electric charge
R	Universal gas constant
R_f	Faradic reaction resistance

R_s	Ohmic resistance of an electrochemical solution
S	Total entropy
S_e	Total entropy at equilibrium
T	Temperature
T_f	Random variable of the gas film life-time
T_g	Random variable of the gas film building-time
T_m	Melting temperature
U	Voltage
$\mathcal{U}$	Normalized voltage
U_A	Water decomposition potential
U_C	Critical voltage
U_D	Mid-point voltage
V	Volume
W	Wagner number
$\mathbb{W}_g s$	Wavelet coefficients of function s with respect to the wavelet function g

Greek Symbols

α	Degree of ionization
β	Full width at half-maximum
γ	Surface tension
δ	Small deviation in a quantity or variable
δ_E	Average spacing between two successive levels of energy
ϵ	Dielectric constant
η	Overpotential
$\hat{\phi}$	Meyer scaling function
$\hat{\psi}$	Meyer wavelet function
κ	Experimental constant
λ	Mean free path

λ	Wavelength
λ_{ji}^{α}	Wavelength of emission
μ_k	Chemical potential of component k
ν	Frequency factor
ν	Stochiometric number
ψ	Total potential energy per unit mass
ψ_k	Potential function of component k
ρ	Total mass density
ρ_k	Mass density of component k
σ	Entropy production per unit mass
θ	Angle
θ	Bubble coverage fraction on gas evolving electrode
ΔG	Gibbs free energy
ΔG_c	Critical Gibbs free energy
ΔG_{des}	Energy of desolvation
$\Delta\mu$	Degree of supersaturation
Γ	Zeldovich factor
Φ	Total entropy production

Chapter 1

Introduction

> *The whole history of science has been the gradual realization that events do not happen in an arbitrary manner, but that they reflect a certain underlying order, which may or may not be divinely inspired.*
>
> *(Stephen Hawking)*

When the applied terminal voltage in a two-electrode cell is higher than a critical value, the conventional electrolysis process is perturbed. The continuous coalescence of adjacent bubbles leads to the formation of a gas film formed around and insulating the electrode from the rest of the solution. Typically, this happens when the surface of the working electrode is much smaller than that of the counter electrode, and is subject to current densities in the order of 1 A/mm^2. Electrical discharges emitted from the surface of the working electrode leads to visible light, as illustrated in Figure 1.1.

Historically, this process, called electrochemical discharges, was the subject of interest of different scientific communities (*2*, *3*). Depending upon the contemporary research orientations and needs, the electrochemical discharge phenomenon was studied firstly by physicists in the 19th century as a physicochemical system with the property of light emission. Not much later, in the beginning of the 20th century,

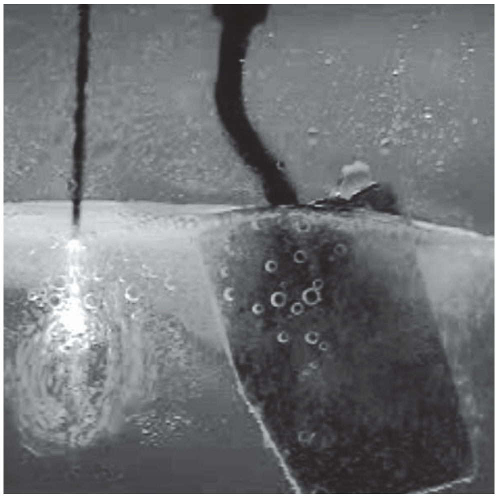

Figure 1.1.: Electrochemical discharges in NaOH 30% wt. aqueous solution at 30 V; cathode (left electrode) made of stainless steel 316 L and anode made of carbon steel, adapted from Wüthrich and Fascio (*1*).

electrical engineers exploited the electrochemical discharges for the development of non-linear electrical components. Later on, in the middle of the century, the chemical and especially the electrochemical community started to get involved and applied the electrochemical discharges as a source of non-faradic electrochemical reactions. As such, micro-precision machining of non-conductive materials (*2*), wastewater treatment (*4*), surface engineering (*5*) and recently the fabrication of ultra-fine particles (*6*–*9*) have been reported by electrochemists as promising applications of this fascinating phenomenon.

1.1. Problem Statement

When the electrochemical discharges are applied to synthesize nano-sized materials, there are very few reports in the literature related to the topic (*6*–*8*) and just one similar to the cathodic electrochemical discharges (*9*), which is the subject of this work. Additionally, none of the aforementioned studies tackle the stability and reproducibility of the manufacturing process and its connection with the electric conditions and other thermodynamic variables. Therefore, the first part of this thesis is on the stability issues and dynamic behavior of the phenomenon which are key parameters for its understanding. Thus, a predictive model based on measurable thermodynamic variables is very desirable, and even essential, in order to apply the phenomenon in repeatable and controllable manners. On the other hand, there is a lack of information on the mechanism of the process for the synthesis of nano-materials which has not been explicitly set. The second part of this thesis focuses on the upstream of the electrochemical discharges and its mechanism, which could be another starting point to fully explore this technology and especially its application in nanoscience.

1.2. Motivation and Challenges

The continuity of the electrochemical process is related to the stability of the gas film, knowing that the general laws of low current electrochemistry can not describe the electrochemical discharge system because it is driven far beyond its thermodynamic equilibrium. Formulating a general mechanistic model is not trivial to do and requires formulations borrowed from the field of nonequilibrium thermodynamics to compact the description of its energy and matter exchange analysis. As for the study of the gas film dynamics, its time-parameters are stochastic from the frequency, time and magnitude viewpoints and require specific algorithms to properly analyze the statistical behavior of the phenomenon.

On the other hand, by applying the electrochemical discharges to the synthesis of nanoparticles, the main challenges at the present are enumerated as *i)* prepare the right electrochemical solution suitable for the discharge regime and also for the stability of the metal ions and for the synthesized products, *ii)* ensure the continuity and repeatability of the manufacturing process based on macroscopic measurable variables, and *iii)* understand and set the overall picture of the nanoparticles synthesis to better improve and optimize the technique.

1.3. Contributions

The contributions of this research work are as follows:

1. **Stability analysis of the gas film during the electrochemical discharges**

   This part of the thesis aims to contract the description of the steady-state discharge regime and the stability of the phenomenon to a set of principal thermodynamic state variables. From the condensed expression of the entropy production in the gas film, it is concluded that the conjugated or associated thermal, electrical and mass transport forces and fluxes should suffice to study the process. Additionally, by applying the Lyapunov sense of stability, the electrochemical discharge phenomenon is found to be more stable at higher voltages and higher bulk temperatures.

   The stability conditions have been verified by the experiment with a simple wavelet-based algorithm for the study of the gas film dynamics from its time-series signal, which is essential to all of the applications of the electrochemical discharge phenomenon. It is found that the gas film life-time increases with the voltage and temperature confirming the theoretical results of this work.

2. **Procedure to successfully manufacture nano-sized materials using the electrochemical discharges**

   A methodological and comprehensive procedure is developed and tailored to apply the electrochemical discharges for the synthesis of nanoparticles, in which the following recommendations are to be taken into account:

- use the metal’s Pourbaix diagram to study the stability of the metal phases,
- add primary or secondary alcohols to the solution to prevent the back oxidation reaction,
- add stabilizing agents to the solution,
- chose the operating voltage from the current-voltage characteristics of the electrochemical cell,
- adjust the average current density from the penetration depth of the cathode into the solution and the current timeseries signal,
- make the compromise between the targeted size and quantity of the products when choosing the duration of the manufacturing process.

3. **Mechanisms of synthesis of nano-sized materials by electrochemical discharges**

   With a series of experimental tests and results, it is proposed that the obtention of zero-valent metal atoms is actuated by a combination of the following two mechanisms:

   - reduction of metal cations by the hydrated electron, the hydrogen radical and secondary generated reducing species from the irradiation of the aqueous solution, and
   - electrode material sputtering by positively charged ions.

   Zero-valent atoms constitute the building units of the electrochemical discharge technique, which undergo nucleation and crystal growth by coalescence, yielding to the colloidal nano-sized aggregates.

4. **Application of nickel oxide synthesized by electrochemical discharges for energy storage purposes**

> Nickel oxide nanoparticles manufactured by electrochemical discharges are tested and characterized as supercapacitor types for energy storage purposes. The pseudocapacitance of the synthesized materials is size-dependent and it is shown that NiO of 70 nm average diameter exhibit high specific capacitance of 218 F/g corresponding to an energy density of almost 100 Wh/kg and 0.7 kW/kg power density.

1.4. Outline of Thesis

This prelude has introduced the process of high current density electrolysis and highlighted some of its challenging points. This thesis manuscript is structured in two main parts. The first one is on the contributions to the physics and fundamentals of the electrochemical discharge phenomenon, while the second part is about the usage of the discharges to manufacture colloidal nano-sized materials and its mechanisms.

From its discovery back in 1844 by Fizeau and Foucault (*10*) to the recent application in nanoscience and nano-sized materials synthesis, Chapter 2 starts by a short review of some key dates in the history of the electrochemical discharge phenomenon. A summary of the current knowledge, as it stands today, essentially from the chemical and electrochemical viewpoints is also outlined and mainly focuses on the electric conditions of the phenomenon, its chemical yield of active radicals and gases, and the spectrochemical analysis of its light emission. This vast field has many other properties outside of the scope of this work which will not be discussed in the interest of brevity.

Chapter 3 is on the application of nonequilibrium thermodynamics analysis of macroscopic trends to the electrochemical discharges. Starting from the basics of conservation laws and the second principle of thermodynamics, the local form of the entropy production in the gas film is developed. From Glansdorff and Prigogine (*11*), the entropy production relation, when combined with Gibbs equation, gives a remarkable compact form as a sum product of conjugated flows and forces of thermal and electrochemical nature, for the stability discussion based on the excess entropy production criterion (*11*).

Chapter 4 is on the dynamics of high current densities electrolysis by presenting and optimizing a robust wavelet analysis algorithm of the current signal during the discharges regime. Statistical random variables representing the gas film formation-time and gas film life-time are introduced and analyzed in real signals acquired under several experimental conditions. Results and conclusions of this Chapter give valuable quantitative information on the stability of the phenomenon.

The second part of this thesis is concerned with the synthesis of nano-sized materials by electrochemical discharges. Prior to the application of the phenomenon in nanoscience, Chapter 5 reviews some examples of known properties of nanomaterials such as the electronic, magnetic, catalytic, mechanical and optical properties and their direct applications in science and engineering. It also describes a selected ensemble of existing synthesis methods, mostly with connection to electrochemistry and discharge physics including the two- and three-electrode electrochemical methods, radiolysis technique and electric discharges.

Chapter 6 constitutes the sequential experimental procedure designed and tailored for the synthesis of nano-sized materials using the electrochemical discharges. It includes the series of preliminary experiments conducted on the electrochemical cell, morphological and chemical characterization by electron microscopy, powder X-ray diffraction, energy dispersive X-ray spectroscopy and cyclic voltammetry. Comparison between the output of the different imposed experimental conditions such as discharging time and voltage are shown and discussed.

Chapter 7 is a continuation of Chapter 6 and presents a comprehensive picture of the overall physicochemical process leading to the manufacture of nano-materials. From the cathode effect and water irradiation to the nucleation and crystal growth of colloidal particles in solution, this Chapter enumerates the possible competing reduction/oxidation reactions of metal ions and the disintegration of the electrode material believed to be behind the synthesis process.

The manufactured nickel oxide nanoparticles by electrochemical discharges are used and tested for electrochemical energy storage purposes. Chapter 8 compares the specific capacitances, the energy and power densities of the synthesized nano-materials with conventional capacitors and with batteries.

Chapter 9 concludes this thesis by providing a review of the highlights and contributions of this research work to the field of the electrochemical discharge phenomenon, and proposes some ideas for future work and investigations.

Part I.

On the Electrochemical Discharges

Chapter 2

Physicochemical Properties

It is a magnificent feeling to recognize the unity of complex phenomena which appear to be things quite apart from the direct visible truth.

(Albert Einstein)

A two-electrode cell under high enough terminal voltage deviates from the traditional electrolysis and gives birth to light emission from the surface of the electrode. A brief introduction to the history of the over 150-year old electrochemical discharge phenomenon is outlined in this Chapter. It is then followed by a review of the electric observations and electric conditions to reach this new state, and are given as it is most commonly known and accepted. The chemical yield of the electrochemical system is also a remarkable example of how the process can exhibit new results, both quantitatively and qualitatively. Indeed, as far as it concerns its chemical performances, an appreciable deviation from the Faraday's law of electrolysis is observed, and therefore will be given special attention from this point of view. With regards to the optical and spectral properties of the discharges, an overview of some spectrochemical results which are most relevant to this work is presented.

2.1. History

The history and progress made on the study of the electrochemical discharges start with the work of the two French physicists Fizeau and Foucault back in 1844. They were the first to report in "Recherches sur l'intensité de la lumière émise par le charbon dans l'expérience de Davy" *Comptes Rendus des Séances de l'Académie des Sciences* **1844**, *18*, 746–754 (*10*) and 860–862 (*12*), that they had observed light emission from an electrode immersed into an electro-conductive media. Indeed, their papers were initially about investigating the spectrum of the light emitted by an electrode of carbon in the experiment of Sir Davy, where they reported at the end of the publication an interesting finding. They observed light emission emanating from the cathode during an electrolysis by means of two electrodes of platinum under a constant potential difference. Fizeau and Foucault had actually discovered the electrochemical discharge phenomenon as they pointed out some analogies with the electric discharges in gaseous media. Many physicists have since been inspired by their discovery as a potential source of light spectra and heat generating electrochemical system.

Ten years later, Hoho (*13*, *14*) with the collaboration of Lagrange, reviewed the experiment more deeply and explained the intermittence of the discharge activity and light emission, as well as the unstable region[*] in the electrical characteristic of the process. They reported an interesting application of the high calorific source property of collective discharges as well as the catalyzed electrochemical reactions at the vicinity of the electrode. The experiment consisted of cathodically polarizing a stack of alloy steel which was subject to the heating process depending upon the gradually increased terminal voltage of the cell. By analogy to the hardening process of metals, they observed changes in the structure of the electrode surface,

---

[*] The unstable region is recognized by a short voltage window in which the electrochemical system may return to the conventional electrolysis process or proceeds to the discharges regime.

but only at the surface and not within the volume of the material (*14*). The cross section of the part of the electrode in question showed two completely different structures: a hard outside layer of fine grains covering an inside fibrous and stiff volume. The conventional hardening, in the other hand, elevates the temperature of a bulk material both at the surface and in the volume and consequently its hardening in contact with cold liquid will affect the whole of its structure. Many applications followed the publication of the work of Hoho, especially in the metallurgy domain.

One noticeable technological invention in the field of applied physics is the current interrupter device invented in 1899 by Wehnelt (*15*). The German physicist brought the first generation of electrolytic interrupters by exploring the intermittent discharges frequencies. Wehnelt's experiment consisted of a large plate of lead placed in an aqueous solution of sulfuric acid as the cathode and a platinum wire fitted into a glass or porcelain tube as the anode. When this arrangement was inserted in the circuit of primary coil, a rapid intermittency in the primary current was recorded. The frequency of Wehnelt's interrupter break can be simply adjusted by regulating the extent of the platinum electrode through the glass or porcelain tube. In his experiments, Wehnelt thought the current was periodically interrupted and he subsequently came up with the innovative idea to replace the mechanical interrupters, widely used at that time to control the induction coils. More detailed surveys on Wehnelt's electrolytic current interrupter can be found in Wüthrich and Mandin (*3*) and in Wüthrich (*2*).

In the middle of the 20th century, the chemistry community engaged the research again on the phenomenon by using and applying it in non-faradic electrochemical reactions. In this way, by trying to reproduce the anode effect in molten salts for the case of electrolytic solutions, Kellogg (*16*), in 1950, pointed out the major effects of heat and temperature at the boundary conditions of the so-called *aqueous anode effect*. The non-negligible economical impact of the anode effect for the production of aluminum by Hérault's process was at the origin of his work. Soon after, the British authors Hickling and Newns (*17*) and Hickling and Ingram (*18*) introduced what they called *contact glow discharge electrolysis* (CGDE) of aqueous solutions. This phenomenon was observed when they were studying the electrolysis of liquid solutions of ammonia while gradually raising the applied voltage between a platinum wire and a counter electrode of much larger surface. A remarkable feature of CGDE is that its chemical effects are closely similar to the ones observed with α-radiolysis and high linear energy transfer radiative chemistry of water. Thus, the chemical performances of the phenomenon are several times the values of Faraday's law of electrolysis. The chemical products are novel for conventional electrolysis such as the release of large amounts of molecular hydrogen and hydrogen peroxide, as well as the $H^{\cdot}$ and $OH^{\cdot}$ radicals in the liquid phase, among other secondary reactions products (*17*–*23*).

The electrochemical principle has attracted even more interest from engineers for applications like micro-scale precision machining of non electro-conductive materials, especially for the bio-compatibles such as glass and composites. The process is known in literature as *spark assisted chemical engraving* (SACE) (*1*, *2*, *24*, *25*). SACE micro-machining combines at certain proportions the heat source property of the electrochemical discharges with the catalyzed chemical etching effects induced by the supporting electrolyte. Here, the calorific process joins the technological application previously introduced by the experiments of Hoho for metal heat treatment. Many promising applications are foreseen for glass machining in the field of micro-electromechanical systems for example, such as micro-reactors, micro-mixers, micro-pumps, lab-on-chip or drug delivery devices.

Another fundamental application of the electrochemical discharges is in the field of synthetic chemistry which has been reported by Harada et al. (*26*–*28*) in the last quarter of the 20th century. Harada et al. (*26*) discovered, by adding organic compounds to the reactants of the electrochemical cell, a new route for the synthesis of amino acids and urea. The experimental setup is comprised of a carbon rod as the cathodic polarized electrode in an aqueous solution of NH_3 and under an electric current of a few milliampers during short time periods. The amino acid analysis plot (*27*) shows the detection of glycine in the first place with other amino acids such as aspartic acid, threonine, serine, glutamic acid, alanine as well as urea. In another report, Harada and Suzuki (*28*) conducted series of experiments with solutions of aliphatic amines and formic acids and they showed as well the formation of some of the essential amino acids such as glycine, alanine, aspartic acid, glutamic acid, etc.

The most recent application of the electrochemical discharges is for the synthesis of nano-sized materials. Lal et al. (*9*) successfully produced Cu, Pt and Au nanoparticles by applying around 20 V terminal voltage in low concentrated aqueous solutions of metal salts. The counter electrode had a significantly larger surface than the working one. Lal et al., in addition to the quasi non-convective situation of the nanoparticles synthesis route, added Corriolis forces to the process by using a rotating disc electrode going up to 5000 rpm. They generated low strength potential vortices around the cathodic polarized electrode such that the fabricated particles were ejected from its vicinity. Following to a series of characterizations of the resulted solutions, the authors have shown the successful manufacturing of 150 nm down to 10 nm particles. They concluded with the promising potential that the electrochemical discharges have as a novel technique in nanoscience.

Similar to the work of Lal et al., Toriyabe et al. (*6*) reported the controlled formation of metallic nano-sized spheres of several transition metals i.e Ni, Ti, Ag and Au by generating discharge plasma in electrolytic medium. Low concentrated aqueous solution of potassium bicarbonate was used as the electrolyte. The sacrificed electrodes, also cathodically polarized, were thin wires of the several targeted metals. The anode was in all cases a platinum mesh of much larger surface than the cathode in order to displace the current breakdown to the cathodic side of the electrochemical cell. The electrical conditions were several times higher than the ones in previous cited work of Lal et al. (*9*) due to the low electric conductivity of the K_2CO_3 solution, as well as the ratio between the electro-active surfaces of the cathode and the anode. According to the electron micrographs of the cathodes' surfaces, relatively monodisperse nano-spheres of Ni, Ti, Ag and Au can be observed which witnesses the versatility of this route for nanoparticles fabrication. By varying the applied terminal voltage, they reported that the nanoparticles' average size is inversely proportional to the potential difference and this was valid for the different metals they used. As an example the average Ni particle diameter is around 300 nm for an applied voltage of 100 V where it goes down to around 100 nm for 160 V cell voltage. The shape of the products is correlated to the applied voltage as well, and has been explained by the authors as being due to the electrothermal instabilities caused by the discharging activity.

In another register of the studied phenomenon, Kawamura et al. (*7*) and Oishi et al. (*8*) successfully synthesized fine metallic particles by generating quasi-stable cathodic discharges in fused salts under atmospheric pressure of argon. Experimentally, the group used a sub-kV DC power supply and a two-electrode configuration cell under atmospheric argon flow. The sacrificial anode, fully immersed into the eutectic melt, was made of the metal of the targeted nanoparticles. The molten salt was composed of 58.5 mol % of LiCl and 41.5 mol % of KCl heated up to a few hundreds degrees Celsius. Additional low concentrated metal salt was added to the melt, i.e. AgCl in the case of silver nano-materials synthesis or K_2TiF_6 in the case of titanium. The electrical discharges were produced by carefully approaching the tungsten cathode tip to the molten salt surface and removing it a few millimeters back. The discharges were stationary for a certain time duration, so that the same procedure had to be repeated again once the electronic activity at the cathode tip ceased. Fine clusters with sizes ranging from a few hundreds of nanometers down to 10 nm were obtained by this technique. The group has suggested some correlations controlling the particles sizes and shapes such as the time of the discharging, the distance between the cathode tip and the bath surface as well as the chemical composition of the salt.

While reviewing the continuous work and contributions of scientists in the field of the electrochemical discharges, one can retain the conclusion that the history of this phenomenon is full of richness and progress. Because it is a complex physicochemical system, the electrochemical discharge phenomenon has attracted various disciplines of research and technological applications throughout the last two centuries of modern science. Indeed, interest in high current densities electrolysis lies not only in its importance for fundamental investigations about its physics but also in its wide range of applications in industry and technology, from the macroscopic down to the nanoscopic scales. Sections 2.2, 2.3 and 2.4 discuss some of the most important features of the phenomenon from the electrical, chemical and spectrochemical viewpoints respectively, which are believed to be essential to the comprehension of the rest of this work.

2.2. I-U Characteristics

Prior to the analysis of the current-voltage characteristics of the electrochemical discharges, let us briefly recall some basic definitions during the electrode reactions. Consider the two-electrode cell arrangement as schematized in Figure 2.1(a). The current is carried thought the electrolytic solution by means of the charged particles, i.e. the ions. The electrode which dips into the solution and is connected to the negative side of the power supply will be negatively charged, and so the reaction occurring at that electrode is the reduction. Indeed, the energy of the electrons is

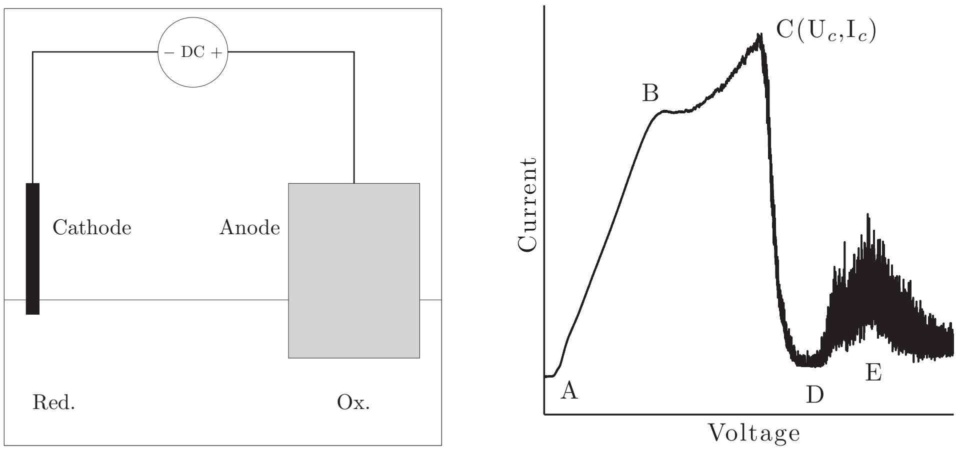

(a) Two-electrode setup used in electrochemical discharge phenomenon.

(b) Typical quasi steady state current-voltage characteristics of the electrochemical discharges (*21*).

Figure 2.1.: Two-electrode cell (2.1(a)) and typical stationary I-U characteristics (2.1(b)) of the electrochemical discharge phenomenon.

high enough so that they can transfer from the cathode into the vacant electronic states of the electrolytic ions. Conversely, the reaction of oxidation occurs at the positively polarized electrode where the electrons transfer from the electrolyte to more favorable energy level at the anode, to close the electric circuit. The plot of the current as a function of the applied voltage in electrochemical experiments generally carries informative details about several parameters of the cell, such as the solution, the nature of the electrodes, as well as the reactions at the electrodes/solution interfaces.

With a linear voltage scan, several sections can be identified from the evolution of the current collected at the cathodic side[†] of the cell shown in Figure 2.1(a). A typical steady state plot is shown in Figure 2.1(b). The region prior to point *A* corresponds to the characteristic potential related to the contribution of the electrochemical reactions in the solution. In the case of aqueous solutions, the potential at point *A*

[†] Note that the cathode has a much smaller active surface than the anode, which is explicitly designed to displace the current breakdown to that electrode and to ignite the electrochemical discharges at lower voltage.

is known as the water decomposition potential which is equal to the sum of the thermodynamic nerstian electromotive force of the cell, U_0, and the sum of the overpotentials of activation and diffusion at both electrodes:

$$U_A = U_0 + \sum |\eta| \tag{2.1}$$

The kinetic term $\sum |\eta|$ represents the difference between the actually measured potential in the electrochemical cell and the thermodynamically predicted one. The variations of $\sum |\eta|$ at high current density values like it is in the case of the electrochemical discharge phenomenon can be neglected from now on. This can be explained from the dimensionless Wagner number, which characterizes the kind of current distribution in an electrochemical cell and the influence of the overpotential (*29*):

$$W = \frac{R_f}{R_s} \tag{2.2}$$

where R_f being the resistance to the secondary current distribution due to the charge transfer faradic reaction at the electrode surface, and R_s is the ohmic resistance of the solution due to primary current distribution. The faradic resistance is related to the variation of overpotential with the applied current density and is very low when compared to R_s. This justifies the assumption in which $\sum |\eta|$ are neglected at high current densities characteristic of the electrochemical discharge phenomenon.

The quasi-linear initial region *A*-*B* in the current-potential curve corresponds to the conventional electrolysis where Ohm's law is satisfied and Joule heating effect due to the ohmic electric power loss in the electrochemical cell is noticed. Macroscopic bubbles formation by the accumulation of the dissolved H_2 in the vicinity of the cathode is characteristic of this step in the current-voltage plot, as illustrated in Figures 2.2(b) and 2.2(c). During this evolution, small bubbles of O_2 are also observed leaving the anode surface. In the vicinity of point *B*, and with

(a) (b) (c) (d) (e) (f) (g) (h) (i)

Figure 2.2.: From conventional electrolysis (2.2(a)-2.2(d)) to the electrochemical discharges (2.2(e)-2.2(i)) with ⌀0.5 mm Ni cathode in 6 M KOH – 0 to 45 V linear scan, with acknowledgments to Zahra Ghorbani.

gradually increasing the applied voltage, a vapor sheath starts to form around the working electrode by gas bubbles coalescence. The coalescence becomes more and more important at higher current densities. At this point, the temperature of the

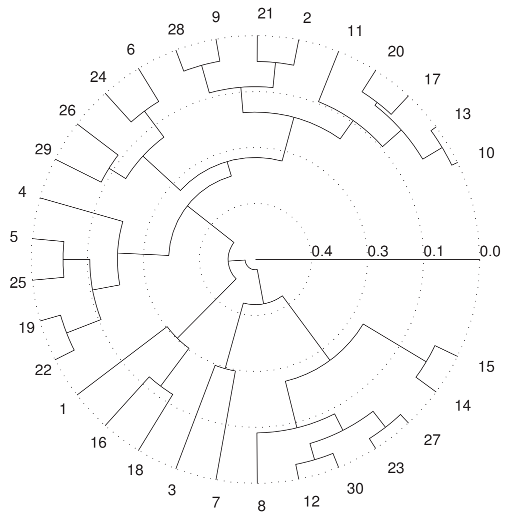

Figure 2.3.: Polar dendrogram representing the binary coalescence of 30 gas bubbles.

solution around the working electrode almost reaches the boiling temperature of the solution.

The plateau in region *B-C* is explained by the bubbles saturation at the active electrode surface and therefore it is also known as the limiting current region. This saturation is mainly function of the electrolytic solution concentration, the chemical composition of the present entities as well as the active electrode surface quality (*30*). Due to the instabilities near this region, the external environment can also play not negligible roles in the gas film behavior. Figure 2.3 illustrates a polar dendrogram of 30 bubbles of the same size randomly distributed at a flat surface. Their coalescence is done hierarchically, pair by pair, depending on the minimum euclidean distance separating them. At the percolation threshold p_c of value 0.5 calculated for the Bethe lattice with three branches (*31*, *32*), the gas film is presumably assumed to be totally formed around the cathodically polarized electrode.

The electrical conductivity of the gas film covering the active electrode is much lower than the electrical conductivity of the electrolytic media. Thus, the equivalent resistance of the gas-solution interface increases sharply leading to high negative values of the electric current gradient (*33*, *34*). This phenomenon is observed in the region *C*-*D* of the current-voltage characteristics, also called the unstable region (see Figure 2.2(d)). Indeed, from the thermodynamic point of view, the system becomes more and more macroscopically complex and is no longer able to remain in that state so that it becomes inevitably unstable. The point *C* is characterized by the coordinates critical voltage, U_C, and critical current, I_C. Note that these two crucial values, necessary for the electrochemical discharges ignition, are controlled by various parameters such as the geometry of the electrochemical cell, the applied voltage, the working electrode surface state and the chemical composition of the electrolyte and its conductivity. From the current-voltage characteristics, note that the current at point *D* tends to zero confirming that the gas film is electrically isolating the electrode. Additionally, one can see a rise rather than a depression of the electrolyte level in contact with the electrode during the discharge regime, witnessing of the non-wettability of the electrode.

Due to the difference of electrical conductivity between the gas film and the liquid phase around it, the breakdown occurs primarily within the vapor sheath, inducing a strong electric field within the separated bubbles covering the electrode (see Figure 2.2(e)). The temperature of the working electrode rises considerably due to the very low heat conductivity of the gas. If now the applied voltage is sufficiently higher, electrons emitted from the cathode are accelerated and therefore the electric field within the bubbles will cause the multiple and cascade ionization of the gas. Starting from point *D*, an electronic avalanche process leads to the electric breakdown of the gas and the initiation of the so-called electrochemical discharges within the gas film, where at this point the working electrode surface begins to emit visible light (see Figure 2.2(f)).

The current timeseries signal collected from a stainless steel 316 L working electrode in NaOH 30 wt.% aqueous solution is plotted in Figure 2.4. The prolonged

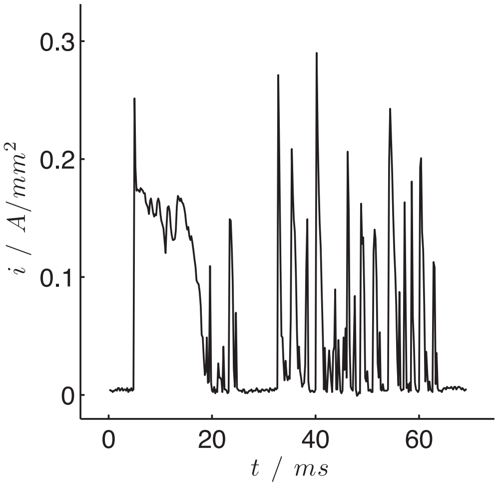

Figure 2.4.: Current signal of electrochemical discharges in NaOH 30% wt. aqueous solution at 30 V; cathode made of stainless steel 316 L and anode made of carbon steel.

inverted U-shape represents the signal related to the gas film formation and the following high frequency signal represents the current response of the discharges. While raising the potential difference from point *D* to point *E*, the current-voltage characteristics curve shows also an approximately steady increase of the discharges intensity as well as their frequency of appearance (see Figures 2.2(g)-2.2(i)). A bit beyond the mid-point *D*, one can observe the electrode covered by a stable glow discharge partially or entirely covering its surface, as illustrated by Figure 1.1. However, starting from *E* the system is forced to decrease its average discharge magnitude where unstable sparks start to be emitted across the gas film. In this region, the melting of the electrode is inevitable due to the high electric power imposed on the electrode.

2.3. Chemical Yields

In addition to the electric observations during the electrochemical discharges, the chemical yields of the phenomenon are worth review. In conventional electrolysis, Faraday's law states that the amount of production of a chemical species at the surface of the electrode is proportional to the charge passed through the closed electrolytic circuit. Mathematically, this is expressed by Faraday's second law of electrolysis, which relates the mass, m, of a chemical species deposited at or liberated from an electrode, proportionally to the total quantity of charge Q and to the molar mass M of the chemical product, and inversely proportional to the valence number z of the ionic state and Faraday constant F, such that:

$$m = \frac{QM}{zF} \tag{2.3}$$

Equation 2.3 can be expressed in terms of a differential equation for the volume production rate of an ideal gas such that:

$$\frac{1}{A}\frac{dV}{dt} = \frac{iRT}{(z/\nu)FP} \tag{2.4}$$

with A the electro-active surface of the electrode, i the current density per unit surface, R the universal gas constant, T the gas temperature, ν the stoichiometric number of the reaction and P the gas pressure. As it concerns the chemical yield of water electrolysis, the reactions happening at the electrodes in acidic medium are:

$$4\,\mathrm{H}^+ + 4\,\mathrm{e}^- \longrightarrow 2\,\mathrm{H}_2 \quad : \quad \text{Cathode} \tag{2.5}$$

$$2\,\mathrm{H}_2\mathrm{O} \longrightarrow \mathrm{O}_2 + 4\,\mathrm{H}^+ + 4\,\mathrm{e}^- \quad : \quad \text{Anode} \tag{2.6}$$

which writes the overall electrochemical reaction which takes place in region A-C of Figure 2.1(b):

$$2\,\mathrm{H}_2\mathrm{O} \longrightarrow 2\,\mathrm{H}_2 + \mathrm{O}_2 \tag{2.7}$$

However, the chemical performances are quite different if the terminal voltage is raised beyond the conventional electrolysis limit. Several studies have been conducted to analyze and evaluate the chemical yields of the electrochemical discharges. In summary, the features of this phenomenon from the chemical point of view are the following:

1. a remarkable deviation of the amounts of chemical species from the expected formation rates according to Faraday's law of electrolysis, and
2. the production of species novel for conventional electrolysis.

To be brief, some of the existing ideas and experiments are selected and reviewed (*4*, *17–20*), which are considered to be the most important and relevant to the scope of this work. For the *glow discharge electrolysis* (GDE) of aqueous solutions, where one of the electrodes is positioned just above the electrolytic surface, Hickling and Ingram (*35*), proposed a mechanism based on similarities with results from α-particles radiolysis of water, also known as high linear energy transfer. For the case of the anodic glow discharges, the electrolyte acts as the cathode and the discharges take place in the gaseous phase near the surface of the electrolyte. To understand the mechanism proposed by Hickling and Ingram, let us consider the overall water radiolysis reaction, depicted by Allen (*36–39*), such that:

$$\mathrm{H_2O} \rightsquigarrow \mathrm{e^-_{aq}}, \mathrm{H}\cdot, \mathrm{OH}\cdot, \mathrm{H_2}, \mathrm{H_2O_2} + \mathrm{H_2O}\cdot + \mathrm{H_3O^+} \tag{2.8}$$

where e^-_{aq} represents the hydrated electron. From the interaction of high energy particles with molecules, the ejection of the single secondary electron reaches rapidly its thermal equilibrium with the surrounding liquid and becomes trapped as the so-called hydrated electron, e^-_{aq}, for the case of water, and solvated electron, e^-_s, for the case of non-aqueous solutions. The thermal equilibrium can be reached in time periods less than the picosecond. A complete survey of radiation chemistry of water and aqueous solutions can be found in the review articles of Fricke and Thomas (*40*) and Dewhurst et al. (*41*).

The first conclusion that can be drawn from Hickling and Ingram's work is the qualitative analogy between the anodic and cathodic GDE, in terms of their chemical products. The effects are much more important for the former due to the high potential fall at the electrolytic surface during an anodic GDE. Secondly, the authors proved that the chemical reactions are initiated, in the first place, in a narrow zone in the liquid phase and not in the gaseous phase. This was concluded from the unsuccessful trials to reproduce the GDE phenomenon by simultaneously placing both electrodes just above the electrolytic surface. In addition, the chemical yield is mainly dependent on the electric energy supplied to the electrochemical system.

In connection with these observations, and due to the high local temperature of the plasma state at the anodic polarized electrode, the charges are assumed to be transported by positive gaseous ions present in the ionized water vapor, probably the $H_2O^+_{gas}$. The gaseous $H_2O^+_{gas}$ ions, accelerated under cathodic potential fall, penetrate the electrolyte with high energies. From Hickling and Ingram, and with comparison with radiation chemistry measurements (*36*, *41*), the average energy load that the $H_2O^+_{gas}$ ions could have is about 100 eV, knowing that their experimental setup operates at some hundreds of volts. With this energy, the mean penetration of the superoxide radicals into the electrolytic medium is expected to be in the range of 10 Å, which defines the *primary reaction zone* of Hickling and Ingram denoted by *RZ 1* in Figure 2.5. This conclusion comes from the comparison of the yield of ionized molecules with high and low kinetic energies (*35*, *42*, *43*).

Within this short range primary reaction zone, water molecules are subject to different decomposition processes of the collision and charge transfer types. Water molecule ionization gives both $OH^{\cdot}$ and $H^{\cdot}$ radicals and is formulated as follows:

$$H_2O \longrightarrow H_2O^+ + e^-_{aq} \xrightarrow{+H_2O} OH\cdot + H_3O^+ \tag{2.9}$$

$$\xrightarrow{+H_2O} OH\cdot + H\cdot \tag{2.10}$$

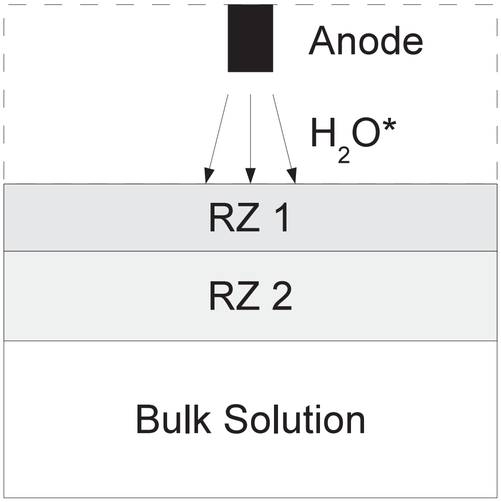

Figure 2.5.: Glow discharge electrolysis model with the primary (RZ 1) and secondary (RZ 2) reaction zones, adapted from Hickling and Ingram (*18*).

The water activation process obeys the reaction:

$$H_2O^* \longrightarrow OH\cdot\ + H\cdot \tag{2.11}$$

Charge transfer mechanism states that one water molecule per superoxide ion will be broken to form one hydroxyl radical and one hydronium cation, such that:

$$H_2O^+ + H_2O \longrightarrow OH\cdot\ + H_3O^+ \tag{2.12}$$

In addition to Reactions 2.9-2.12, Hickling and Ingram suggested the formation of molecular hydrogen peroxide and hydrogen following the Reactions:

$$H_2O^+ + H_2O^+ \longrightarrow H_2O_2 + 2\,H^+ \tag{2.13}$$

$$H_2O^* + H_2O^* \longrightarrow H_2O_2 + H_2 \tag{2.14}$$

Table 2.1.: Chemical reactions in glow discharge electrolysis of water, adapted from Fricke and Thomas (*40*).

Chemical reaction	**Reaction rate constant k†**
$H\cdot + H\cdot \longrightarrow H_2$	1.0
$H\cdot + OH\cdot \longrightarrow H_2O$	1.9
$OH\cdot + OH\cdot \longrightarrow H_2O_2$	0.44
$H\cdot + H_2O_2 \longrightarrow H_2O + OH\cdot$	$1.1 \cdot 10^{-2}$
$OH\cdot + H_2O_2 \longrightarrow H_2O + HO_2^{\cdot}$	$0.9 \cdot 10^{-3}$
$H\cdot + HO_2^{\cdot} \longrightarrow H_2O_2$	2.0
$OH\cdot + HO_2^{\cdot} \longrightarrow H_2O + O_2$	0.9
$H\cdot + O_2 \longrightarrow HO_2^{\cdot}$	2.0
$HO_2^{\cdot} + HO_2^{\cdot} \longrightarrow H_2O_2 + O_2$	$2 \cdot 10^{-4}$

† k × ∽ 10^{10} $M^{-1}.s^{-1}$ (zero-order reactions).

Furthermore, and by the diffusion of these energetic chemical species, i.e. OH·, H·, H_2O_2 and H_2, out of the primary reaction region, Table 2.1 gives a summary of the chemical reactions expected to occur at the *secondary reaction zone*, *RZ 2*, with their reaction rate constants. Indeed, in the absence of any foreign solute in water, Allen (*36*) stated that the reaction of the free radicals OH· and H· should cause the disappearance of these radicals where H· and H· react to form the molecular H_2, H· and OH· react to reform the water molecule, and OH· and OH· react to form the hydrogen peroxide H_2O_2 (see Table 2.1). In addition to this, comparison between experimental investigations when water was irradiated with α-rays and X-rays shows that the steady-state concentrations of H_2O_2 and H_2 were much more important for the former type of radiation. The products concentrations are therefore proportional to the used intensity of radiation.

One of the main products obtained in glow discharge electrolysis of inert aqueous solutions, and not in conventional electrolysis, is the hydrogen peroxide H_2O_2. In the primary reaction zone, Reactions 2.13 and 2.14 involving the H_2O^+ and the H_2O^+ are expected to ensure its production, whereas in the secondary reaction zone, reactions in Table 2.1 yield to the production of H_2O_2. In the case of oxidation and reduction of solutes present in aqueous solutions, the back reaction involving the hydrogen peroxide and the molecular hydrogen is in continuous competition with the reactions of solutes with the free radicals $OH\cdot$ and $H\cdot$.

2.4. Spectrochemical Analysis

What is visibly remarkable about the electrochemical discharges, as previously mentioned, is the emission of visible light. Indeed, from the results obtained by fast video imaging, discharge dimensions during cathodic electrochemical discharges were evaluated by Guilpin and Garbarz-Olivier (*44*) to be around some tens of micrometers. Recent work, about single and collective behavior of discharges from electrodes made of industrial grade H30T Al alloy in alkaline solutions, published by Yerokhin et al. (*45*), confirms these results. The discharge cross-sectional areas were found to lie in a range of 0.01 to 1.35 mm^2, depending on the applied voltage and surface characteristics.

The spectrochemical analysis of light emitted during the electrochemical discharges provides valuable information on the phenomenon such as the electronic temperature, the degree of ionization, the electronic density, etc (*46*). The origin of light emission is due to the de-excitation process of the chemical species present around the electrode and chemical species constituting the electrode material. Most of these excited species originate from the pulverization of the aqueous solution or of elements present at the working electrode surface (*33*, *44*, *45*, *47–49*). The excellent reviews by Maximov and Khlustova (*48*, *49*) give a general summary of the characteristics of optical emissions form glow discharges of the most commonly used solutions and metals. For example, in the case of an electrolytic solution containing an alkali metal, such as sodium and potassium, or an alkaline earth metal, such as magnesium and calcium, the color of the discharges is characteristic of the emission resonance lines of these metallic elements. The authors qualified the process by *nonequilibrium system* with important and wide range of rotational, vibrational and electron temperatures. Therefore, they suggested both electron collisions and ion bombardment mechanisms for the formation of the energetic emitting species. Some examples of spectra recorded during the cathodic electrochemical discharges in their corresponding experimental conditions conducted by Guilpin and Garbarz-Olivier (*44*) are given in Table 2.2. The spectra are originated either from the elements constituting the cathode, the electrolyte or an association of both which is the case of species denoted by $MH^{\cdot}$ in Table 2.2.

The light spectra for both cathode and anode effects are reported by several other groups and in general it is more rich and diverse for the cathodic polarization arrangement. From the experimental investigations reported by Kobayashi et al. (*47*) in 0.5 M NH_4NO_3 solution, the emission spectrum at a platinum anode shows weak lines of hydrogen and oxygen. However, platinum cathode emission measurements in the visible from 350 to 800 nm show several emission lines originating from the atomic state of hydrogen, oxygen as well as platinum. The obtained transmission spectra clearly show the 656.3 and 486.1 nm lines corresponding to the transitions

Table 2.2.: Recorded spectra during the cathodic electrochemical discharges, adapted from Guilpin and Garbarz-Olivier (*44*).

Experimental conditions	**Observed spectra**
Pt in H_2SO_4 1 M, 110 V	Pt(I), Pt(II), H, OH
M with M={Au, Cu, Ag, Zn, Al} in H_2SO_4 1 M, 110 V	M(I), M(II), H, OH, $MH^{\cdot}$
Pt in KOH 1 M, 110 V	Pt(I), Pt(II), K(I), K(II) H, OH
Pt in KBr 1 M, 140 V	Pt(I), Pt(II), K(I), K(II) H, OH, O(II)

$n = 3$ to $n = 2$ and $n = 4$ to $n = 2$ Balmer series of hydrogen atom (*47*). The corresponding colors for these two wavelengths are the red and the blue-green color, respectively. The full widths at half maximum of the H emission at 656.3 and 486.1 nm increase with the applied voltage. The electron density is estimated by Kobayashi et al. to be in the order of 10^{16} cm^{-3} for a few hundreds of applied volts at the cathodic polarized electrode. H_2 emission at 529.1 nm and the O transition from $3p\ {}^5P \rightarrow 3s\ {}^5S^0$ at the 777.1 nm wavelength are also recognized from the spectra. In addition to that, strong emission lines of platinum are recorded at the wavelengths 392.3, 367.4, 367.2, 363.9, 362.8, 348.6, 340.9, and 330.1 nm. Despite the consequent concentration of NH_4^+ and NO_3^- ions from the dissociation of the 0.5 M NH_4NO_3 aqueous solution, emissions from both N and NO were not recorded in the spectra.

Comparison between the emission spectra in a 0.5 M of different solutions: HNO_3, NH_4NO_3, $LiNO_3$ and KNO_3 reveals that a broad OH emission is observed just for the low pH nitric acid solution and also that the potassium cations K^+ are responsible for the vanishing of H_2 and Pt emissions. By analyzing the spectra from the three acids HNO_3, H_2SO_4 and HCl, Kobayashi et al. showed a common behavior of the solutions where OH emission is observed in addition to the emissions of H, H_2, O and Pt. The solutions contain respectively the NO_3^-, SO_4^{2-} and Cl^- ions but no emissions from N, S and Cl are observed. An additional experiment has been conducted by the authors in the attempt to relate the emission of OH. Indeed, by comparing strongly alkaline solutions of KOH and NaOH, one can observe the emission of potassium at 769.9 nm but difficultly distinguish the very closed together spectral lines of sodium at 589.0 and 589.6 nm. From the above measurements, the OH emission is quenched or canceled only in neutral solutions containing nitrate ions.

The excitation temperature can be estimated from the spectral lines of chemical species in the case of local thermal equilibrium hypothesis. If we denote by I_{ji}^{α} the intensity of the emission line of a species at the degree of ionization α and transiting from level j to i, λ_{ji}^{α} the wavelength of emission, g_i^{α} the degeneracy factor or the statistical weight of level i, f_{ji}^{α} the transition probability and E_j^{α} the energy at level j, it is known that (*44*, *50*):

$$\log \frac{I_{ji}^{\alpha}(\lambda_{ji}^{\alpha})^3}{g_i^{\alpha} f_{ji}^{\alpha}} = \mathrm{C} - \frac{5040\, E_j^{\alpha}}{T} \tag{2.15}$$

where C is an experimental constant. The temperature T can be obtained from Boltzmann plot. The straight lines of $\log I_{ji}^{\alpha}(\lambda_{ji}^{\alpha})^3/g_i^{\alpha} f_{ji}^{\alpha}$ versus the energy of Fe emission lines of in NH_4NO_3 and $Fe(NO_3)_3$ solution at 600 and 800 V give an approximated plasma temperatures of 13000 and 15000 K respectively (*47*). From Guilpin and Garbarz-Olivier (*44*), T was estimated at 4000 K from the measurement of Mg spectral emission lines in 1 M $MgCl_2$ under 420 V during the anode effect of Pt wire. A temperature of 3900 K was obtained from the radiation of Ca in $CaCl_2$ and under the same experimental conditions.

From the above reviewed works encompassing the electric, chemical/electrochemical and spectrochemical aspects of the electrochemical discharges, it is clear that the phenomenon is a multidisciplinary problem that has been tackled from different directions since its discovery back in 1844 (*10*). With applications of great use in modern science and with aim to have a better control and eventually scale it up to industrial production, there is, however, still a lack in the description of the phenomenon with thermodynamic state variables. In fact, it does not exist at all. Some statistical integrations or empiric-experimental relations about the gas film and its formation parameters are reported (*2*, *32*, *51*–*55*) but there is not a single work on the issues of its stability. Although the attempts to link the hydrodynamic instabilities of type Kelvin-Helmholtz to the electrode effect has been proposed by Mazza et al. (*52*) and Sengupta et al. (*56*), there are some limitations worth noting: *i)* the critical volume flux density of vapor in gas evolving electrodes is much smaller and represents roughly some 5% of its analogous in boiling, *ii)* no analogy is possible between superheating in boiling and the applied potential at the elecotrode, and most importantly *iii)* there is no discharge regime which can be reached in film boiling (*57*). Compact thermodynamic analysis of the electrochemical discharges and the stability considerations of the phenomenon are of fundamental importance and are presented and discussed in Chapter 3.

Chapter 3

Macroscopic Analysis

> *If for the entire universe we conceive the same magnitude to be determined, consistently and with due regard to all circumstances, which for a single body I have called entropy, and if at the same time we introduce the other and simpler conception of energy, we may express in the following manner the fundamental laws of the universe which correspond to the two fundamental theorems of the mechanical theory of heat: (a) The energy of the universe is constant, (b) The entropy of the universe tends to a maximum.*
>
> *(Rudolf Clausius)*

The gas film stability plays a fundamental role in the electrochemical discharge phenomenon. Its formation/breaking during the process is one of the key parameters to understand its numerous applications. The system is an open-system, i.e. exchanges both matter and energy with its environment, and is driven far from its equilibrium state. Indeed, the conventional electrolysis observed at lower voltages is considered as an ancestral state of the system once the voltage exceeds a critical value. This needs a continuous supply of power to the electrochemical cell in order that the nonequilibrium system keeps its new state of electrochemical discharges.

In the attempt to explain its macroscopic behavior, the nonequilibrium thermodynamic analysis is used. It is the starting point of the gas film stability study which is to be analyzed at the end of this Chapter. In order to determine the entropy production in the gas film, the local expressions of conservation laws and the first law of thermodynamics are applied to the system. The entropy production is considered to be the most general approach to study systems far from their equilibrium situations (*11*, *58*).

In a second step, the second law as well as the differential form of Gibbs equation are used to write compact expressions for the stability discussion on the electrochemical discharges or more explicitly the gas film. In summary, from the nonequilibrium thermodynamics analysis of the electrochemical discharges system, the combination of thermal and electrochemical effects are found to be at the origin of the entropy production in the gas film. Considering the Lyapunov's sense of stability of dissipative systems, the gas film behavior is discussed in Section 3.3 based on Glansdorff and Prigogine criterion and the *excess entropy production* written in the form of general conjugated thermodynamical flows and forces (*11*, *58–61*).

3.1. Definition of the System

The system under investigation for the stability analysis of the electrochemical discharge phenomenon is the fully formed gas film around the cathode, as illustrated in Figure 3.1(a). The gas film has a volume V and is limited by a surface A, and will be denoted by Σ in the following analysis. System Σ is a macroscopic element of fluid and consists of n chemical components amongst which r chemical reactions are possible (*11*). Some examples of the chemical species and their possible reactions

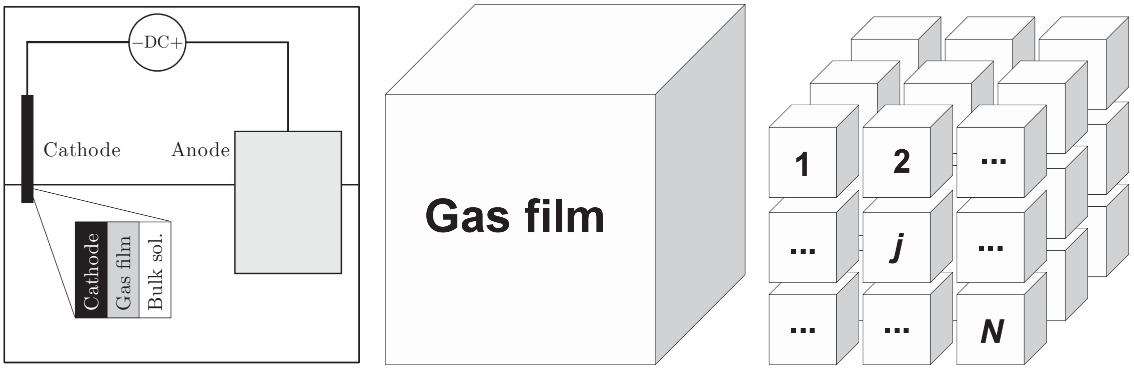

(a) Two-electrode setup. (b) System Σ. (c) N subsystems of Σ.

Figure 3.1.: Scheme of the Electrode | Gas film | Bulk solution model for stability discussion.

were presented in Table 2.1. Nonequilibrium thermodynamics approach is based on local expressions of conservation laws which calls the assumption of local thermodynamic equilibrium. Figure 3.1(c) shows a schematic representation of this assumption in our case where Σ, in Figure 3.1(b), is divided into N subsystems. It is assumed that each subsystem is large enough so that it is contains a large number of particles. With this assumption, each of the thermodynamic state variables ρ_k for the mass density of component k, z_k for its density of charge, $\mathbf{v}_k$ for its velocity, $\mathbf{F}_k$ for its density of external force, ψ_k for its potential energy and $\mathbf{J}_k$ for the diffusion flow of component k remains constant in each subsystem $j = 1, 2, ..., N$ of Σ. The flow of analysis in this Chapter can be summarized in the scheme represented by Figure 3.2. Section 3.2 reviews the foundations of nonequilibrium thermodynamics analysis and the specific application to our system is done in Section 3.3.

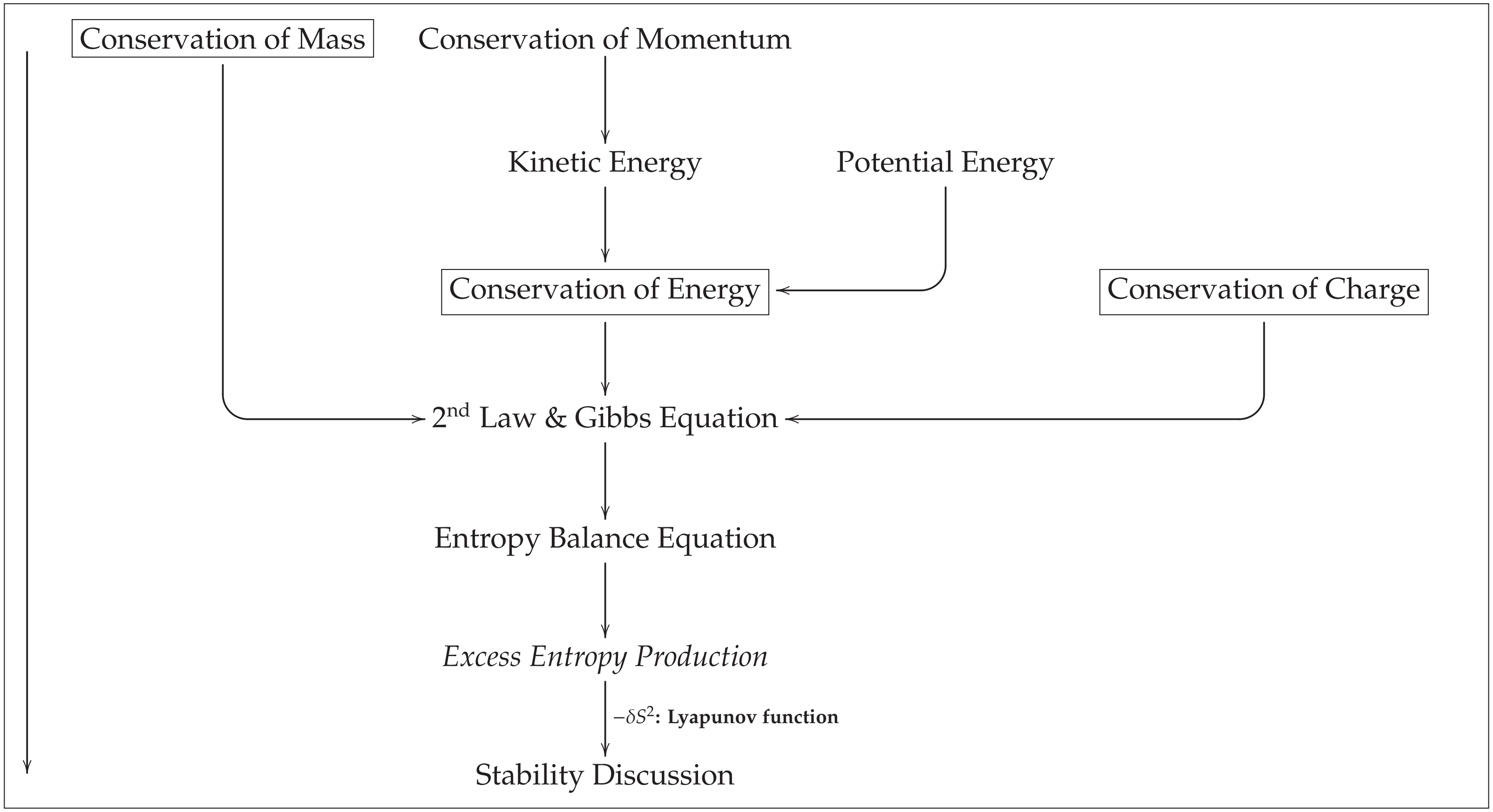

Figure 3.2.: Scheme of nonequilibrium thermodynamics approach for the stability analysis of the gas film during the electrochemical discharges.

3.2. Review of Nonequilibrium Thermodynamics

In this section, the nonequilibrium thermodynamics formulation is applied to the electrochemical discharges. In the interest of clarity, the well-known derivation of local expressions of the first and second laws of thermodynamics are reproduced here. The reader familiar with the foundations of nonequilibrium thermodynamics can go directly to the final result expressed by Equation 3.45. Two cases are treated alternatively for the expression of the first law: the first one is for the case of conservative force fields and the second one is more appropriate to the study of general electrochemical systems and for the electrochemical discharge phenomenon in particular. In the later case study, the considered force is the electromagnetic force of Lorentz, with which the electrical parameters of the system can be described. The entropy balance equation is then expressed by plugging the conservation laws into the differential form of Gibbs equation.

3.2.1. Local Formulation of Entropy Production

3.2.1.1. Conservation of Mass

The rate of change in time of m_k, the mass of a component k among the n ones in system Σ, is expressed by:

$$\frac{dm_k}{dt} = \frac{d}{dt}\int_V \rho_k \, dV = \int_V \frac{\partial \rho_k}{\partial t} \, dV \tag{3.1}$$

where ρ_k is the mass density of the component k. Relation 3.1 can be expressed as the sum of a surface and a volume term (*11*, *62*), such that:

$$\int_V \frac{\partial \rho_k}{\partial t} \, dV = -\int_A \rho_k \mathbf{v}_k \, d\mathbf{A} + \sum_{j=1}^{r} \int_V \nu_{kj} J_j \, dV \tag{3.2}$$

where $\mathbf{v}_k$ is the vector velocity of k thought the surface element $d\mathbf{A}$ and the coefficient ν_{kj}[*] is proportional to the stoichiometric number of k in the chemical reaction j. The scalar J_j is nothing but the chemical reaction rate of reaction j. The mass balance equation of k can be rearranged in a differential form using Green-Ostrogradsky theorem, such that:

$$\frac{\partial \rho_k}{\partial t} = -\nabla \cdot \rho_k \mathbf{v}_k + \sum_{j=1}^{r} \nu_{kj} J_j \tag{3.3}$$

and by summing up over all components k in the system Σ, the law of conservation of mass is written in its common form as:

$$\frac{\partial \rho}{\partial t} + \nabla \cdot (\rho \mathbf{v}) = 0 \tag{3.4}$$

where ρ is the total density of the system and $\mathbf{v}$ its velocity. Note that $\sum_{k=1}^{n} \nu_{kj}$ is null for each chemical reaction j. The mass equations for components k can be rewritten then as (*63*):

$$\frac{d\rho_k}{dt} = \frac{\partial \rho_k}{\partial t} + (\mathbf{v} \cdot \nabla)\, \rho_k \tag{3.5}$$

Plugging Equation 3.3 into Equation 3.5 and using the diffusion flow of component k defined by Glansdorff and Prigogine (*11*) as:

$$\mathbf{J}_k = \rho_k \left(\mathbf{v}_k - \mathbf{v}\right) \tag{3.6}$$

the other form of mass balance equations, which gives the rate of change of the mass fraction c_k of component k ($c_k = m_k/m$), can be formulated as (*62*, *64*):

$$\rho \frac{dc_k}{dt} = -\nabla \cdot \mathbf{J}_k + \sum_{j=1}^{r} \nu_{kj} J_j \tag{3.7}$$

---

[*] ν_{kj} is positive if k is a product and negative if its is a reactant in the reaction j.

3.2.1.2. Conservation of Momentum

To write the explicit local expression for the first law, we need first to formulate the kinetic energy of Σ from the conservation of momentum (see Figure 3.2). Newton's second law writes (*62*, *64*):

$$\rho \frac{d\mathbf{v}}{dt} = -\nabla P + \sum_k \rho_k \mathbf{F}_k \tag{3.8}$$

where P is the pressure and $\mathbf{F}_k$ is the external force per unit mass acting on the component k. One can also express Equation 3.8 in the form of a time derivative of the momentum density as follows (*62*, *64*):

$$\frac{\partial \rho \mathbf{v}}{\partial t} = -\nabla \left(\mathbf{v} \rho \mathbf{v} + P \right) + \sum_k \rho_k \mathbf{F}_k \tag{3.9}$$

First, it is considered that the forces $\mathbf{F}_k$ are conservative and can therefore be derived from a potential ψ_k, so that one can write:

$$\mathbf{F}_k = -\nabla \psi_k \quad \text{and} \quad \frac{\partial \psi_k}{\partial t} = 0 \tag{3.10}$$

Second, the nonconservative electromagnetic Lorentz force is used which more appropriate to the study of the electrochemical discharges. Lorentz force acting on a component k per unit mass is expressed as:

$$\mathbf{F}_k = z_k \left(\mathbf{E} + \frac{1}{c} \mathbf{v}_k \times \mathbf{B} \right) \tag{3.11}$$

where z_k is the electric charge per unit mass of component k, $\mathbf{E}$ the electric field, $\mathbf{B}$ the magnetic field, and c the speed of light . In this case, Equation 3.8 can be written as follows:

$$\rho \frac{d\mathbf{v}}{dt} = -\nabla P + \sum_k \rho_k z_k \left(\mathbf{E} + \frac{1}{c} \mathbf{v}_k \times \mathbf{B} \right) \tag{3.12}$$

By expressing the total electric density **I** as the sum of a two contributions of convective and conductive nature (*62*):

$$\mathbf{I} = \sum_{k=1}^{n} \rho_k z_k \mathbf{v}_k = \rho z \mathbf{v} + \sum_{k=1}^{n} z_k \mathbf{J}_k = \rho z \mathbf{v} + \mathbf{i} \tag{3.13}$$

the momentum balance in the electrochemical system can be formulated as:

$$\rho \frac{d\mathbf{v}}{dt} = -\nabla P + \rho z \left(\mathbf{E} + \frac{1}{c} \mathbf{v} \times \mathbf{B} \right) + \frac{1}{c}\, i \times \mathbf{B} \tag{3.14}$$

3.2.1.3. Conservation of Energy

The conservation of energy or the first principle of thermodynamics states that the total energy within any volume element of the system can only change if energy flows through the boundaries of the volume element. Energy can not be created or lost (*11*, *62*, *64*–*66*). System Σ freely exchanges energy with its surroundings. Mathematically, the time derivative of the total energy E is written as follows (*62*, *64*):

$$\frac{dE}{dt} = \frac{d}{dt} \int_V \rho e \, dV = \int_V \frac{\partial \rho e}{\partial t} \, dV = -\int_A \mathbf{J}_e \, d\mathbf{A} \tag{3.15}$$

where e is the total energy per unit mass and $\mathbf{J}_e$ is the energy flux per unit surface and unit time. In its differential form, Equation 3.15 can be written:

$$\frac{\partial \rho e}{\partial t} = -\nabla \cdot \mathbf{J}_e \tag{3.16}$$

The total specific energy e can be expressed as the sum of three kinds of energies: the specific kinetic energy, the specific potential energy and the specific internal energy of the system, such that:

$$e = \frac{1}{2}\mathbf{v}^2 + \psi + u \tag{3.17}$$

Similarly, from Kondepudi and Prigogine (*64*) and de Groot and Mazur (*62*), its flux $\mathbf{J}_e$ is equal to the sum of the convection flux of the total energy, $\rho e\mathbf{v}$, the mechanical energy flux $P\mathbf{v}$, the potential energy flux, $\sum_k \psi_k \mathbf{J}_k$, due to the diffusion of k and finally the heat flow $\mathbf{J}_q$:

$$\mathbf{J}_e = \rho\mathbf{v}\left(\frac{1}{2}\mathbf{v}^2 + \psi + u\right) + P\mathbf{v} + \sum_k \psi_k \mathbf{J}_k + \mathbf{J}_q \tag{3.18}$$

For the case of electromagnetic forces, the total specific energy is defined as (*62*):

$$e = \frac{1}{2}\mathbf{v}^2 + \frac{1}{\rho}\left(\mathbf{E}^2 + \mathbf{B}^2\right) + u \tag{3.19}$$

with the correspondent total energy flux (*62*):

$$\mathbf{J}_e = \rho\mathbf{v}\left(\frac{1}{2}\mathbf{v}^2 + u\right) + P\mathbf{v} + c\,\mathbf{E}\times\mathbf{B} + \mathbf{J}_q \tag{3.20}$$

For the derivation of the conservation of energy equation, the balance equations for the kinetic and potential energies are needed (see Figure 3.2). From Equation 3.8, it is possible to derive a balance equation form for the kinetic energy as follows (*62*):

$$\begin{aligned} \rho\frac{d}{dt}\left(\frac{1}{2}\mathbf{v}^2\right) &= \rho\mathbf{v}\frac{d\mathbf{v}}{dt} \\ &= -\mathbf{v}\nabla P + \sum_k \rho_k \mathbf{F}_k \mathbf{v} \\ &= -\nabla\cdot(P\mathbf{v}) + P\nabla\cdot\mathbf{v} + \sum_k \rho_k \mathbf{F}_k \mathbf{v} \end{aligned} \tag{3.21}$$

which can be derived also from Equation 3.9 to have the form:

$$\frac{\partial}{\partial t}\left(\frac{1}{2}\rho\mathbf{v}^2\right) = -\nabla\cdot\left(\frac{1}{2}\mathbf{v}\rho\mathbf{v}^2 + P\mathbf{v}\right) + P\nabla\cdot\mathbf{v} + \sum_k \rho_k \mathbf{F}_k \mathbf{v} \tag{3.22}$$

Considering Equation 3.14, the balance equation for the kinetic energy is written as:

$$\frac{\partial}{\partial t}\left(\frac{1}{2}\rho\mathbf{v}^2\right) = -\nabla\cdot\left(\frac{1}{2}\mathbf{v}\rho\mathbf{v}^2 + P\mathbf{v}\right) + \rho z\mathbf{v}\cdot\mathbf{E} - \frac{1}{c}\mathbf{i}\cdot(\mathbf{v}\times\mathbf{B}) \tag{3.23}$$

As for the rate of change of the potential energy, defined by $\rho\psi = \sum_k \rho_k\psi_k$, one can derive from Equation 3.3 the following expression (*62*):

$$\begin{aligned}\frac{\partial\rho\psi}{\partial t} &= \frac{\partial}{\partial t}\sum_k \rho_k\psi_k \\ &= -\nabla\cdot\left[\rho\psi\mathbf{v} + \sum_{k=1}^{n}\rho_k\psi_k(\mathbf{v}_k-\mathbf{v})\right] + \sum_{k=1}^{n}\rho_k\nabla\psi_k\cdot\mathbf{v} \\ &\quad + \sum_{k=1}^{n}\rho_k\nabla\psi_k\cdot(\mathbf{v}_k-\mathbf{v}) + \sum_{k=1}^{n}\sum_{j=1}^{r}\nu_{kj}J_j\psi_k\end{aligned} \tag{3.24}$$

Recalling the diffusion flow $\mathbf{J}_k$ of component k defined by Equation 3.6, the conservative forces properties expressed by Equation 3.10 and considering that the potential energy is conserved in each chemical reaction j, Equation 3.24 is reduced to:

$$\frac{\partial\rho\psi}{\partial t} = -\nabla\cdot\left[\rho\psi\mathbf{v} + \sum_{k=1}^{n}\psi_k\mathbf{J}_k\right] - \sum_{k=1}^{n}\rho_k\mathbf{F}_k\cdot\mathbf{v} - \sum_{k=1}^{n}\mathbf{J}_k\cdot\mathbf{F}_k \tag{3.25}$$

Subtracting the sum of Equations 3.22 and 3.25 from Equation 3.16, and using the relation for the specific energy flux (Equation 3.18), one obtains the balance equation for the specific internal energy u as:

$$\frac{\partial\rho u}{\partial t} = -\nabla\cdot\left(\rho\mathbf{v}u + \mathbf{J}_q\right) - P\nabla\cdot\mathbf{v} + \sum_k \mathbf{J}_k\cdot\mathbf{F}_k \tag{3.26}$$

On the other hand, if the electromagnetic energy density is taken into account, knowing that the Poynting equation (*62*, *67*) writes:

$$\frac{\partial}{\partial t}\left[\frac{1}{2}\left(\mathbf{E}^2+\mathbf{B}^2\right)\right] = -\nabla\cdot[c\,(\mathbf{E}\times\mathbf{B})] - \mathbf{I}\cdot\mathbf{E} \tag{3.27}$$

one gets the following expression:

$$\frac{\partial}{\partial t}\left[\frac{1}{2}\left(\rho\mathbf{v}^2+\mathbf{E}^2+\mathbf{B}^2\right)\right]=P\nabla\mathbf{v}-\mathbf{i}\cdot\left(\mathbf{E}+\frac{1}{c}\mathbf{v}\times\mathbf{B}\right)-\nabla\cdot\left(\frac{1}{2}\mathbf{v}\rho\mathbf{v}^2+P\mathbf{v}+c\;\mathbf{E}\times\mathbf{B}\right) \quad (3.28)$$

Similarly to the case of conservative forces, by substituting Equation 3.28 from Equation 3.16 and using Equation 3.20 one obtains the balance equation of the specific internal energy u as (*62*):

$$\frac{\partial\rho u}{\partial t}=-\nabla\cdot\left(\rho\mathbf{v}u+\mathbf{J}_q\right)-P\nabla\cdot\mathbf{v}+\mathbf{i}\cdot\left(\mathbf{E}+\frac{1}{c}\mathbf{v}\times\mathbf{B}\right) \quad (3.29)$$

or alternatively, it can be written as:

$$\rho\frac{du}{dt}=-\nabla\cdot\mathbf{J}_q-P\nabla\cdot\mathbf{v}+\mathbf{i}\cdot\left(\mathbf{E}+\frac{1}{c}\mathbf{v}\times\mathbf{B}\right) \quad (3.30)$$

For the specific case of the electrochemical discharges system, it is not erroneous to neglect the magnetic field term in Lorentz force in Equation 3.30. The first law of thermodynamics is therefore written in the simplified form, to be considered from now on, as:

$$\rho\frac{du}{dt}=-\nabla\cdot\mathbf{J}_q-P\nabla\cdot\mathbf{v}+\mathbf{i}\cdot\mathbf{E} \quad (3.31)$$

3.2.1.4. Entropy Balance

The second principle of thermodynamics states that for any macroscopic system, the variation of the entropy dS is equal to the sum of two terms as follows:

$$dS=d_eS+d_iS \quad (3.32)$$

where d_eS is the variation of entropy of the system supplied by its environment and d_iS is the entropy production inside the system (*11*, *62*, *64*–*66*). The entropy flow d_eS may have any sign depending on the interaction of the system with the surrounding environment while d_iS is positive for irreversible transformations and zero for reversible ones:

$$d_iS \geqslant 0 \tag{3.33}$$

Because it is an irreversible process, a more suitable expression for the study of the electrochemical discharge phenomenon can be expressed by the local density of entropy balance of the system as:

$$\frac{\partial \rho s}{\partial t} = -\nabla \mathbf{J}_{s,tot} + \sigma \tag{3.34}$$

which relates the time change of entropy per unit mass to a flow term, $\mathbf{J}_{s,tot}$, and a source term, σ. An alternative expression of Equation 3.34 can be written as follows:

$$\rho \frac{ds}{dt} = -\nabla \mathbf{J}_s + \sigma \tag{3.35}$$

where $\mathbf{J}_s$ is defined by the difference between the total entropy flux, $\mathbf{J}_{s,tot}$, and a convective term, $\rho s \mathbf{v}$:

$$\mathbf{J}_s = \mathbf{J}_{s,tot} - \rho s \mathbf{v} \tag{3.36}$$

The rate of change of the entropy based on the combination of the conservation laws and Gibbs equation shall lead to a remarkable expression of product sum of conjugated thermodynamical flux and forces (*11*, *61*, *62*, *64*, *68*). As discussed in Section 3.2, conservative and nonconservative forces are treated separately for the derivation of the equations, but again it is the Lorentz force which will lead to a comprehensive view of stability of the gas film. The validity of the use of Gibbs formula at the local level for the entropy balance equation has been compared by means of the kinetic theory of dilute gases (*62*). This comparison is based on the integro-differential equation of Boltzmann and shows that the microscopic and macroscopic perspectives are identical to the first order of Chapman-Enskog series decomposition (*69*). The differential form of Gibbs function defined in terms of the system's specific properties writes:

$$Tds = du + Pdv - \sum_{k=1}^{n} \mu_k dc_k \tag{3.37}$$

where μ_k is the chemical or thermodynamic potential of component k. With Gibbs formula and the Equations of conservation laws rewritten below:

$$\rho \frac{dc_k}{dt} = -\nabla \cdot \mathbf{J}_k \tag{3.38}$$

$$\rho \frac{du}{dt} = -\nabla \cdot \mathbf{J}_q - P\nabla \cdot \mathbf{v} + \mathbf{i} \cdot \mathbf{E} \tag{3.39}$$

$$\rho \frac{dz}{dt} = -\nabla \cdot \mathbf{i} \tag{3.40}$$

one can write the expression of the entropy balance as:

$$\rho \frac{ds}{dt} = -\nabla \cdot \left(\frac{\mathbf{J}_q - \sum_{k=1}^{n} \mu_k \mathbf{J}_k}{T} \right) - \frac{\nabla T}{T^2} \cdot \mathbf{J}_q - \frac{1}{T} \sum_{k=1}^{n} \mathbf{J}_k \cdot \left[T\nabla \left(\frac{\mu_k}{T} \right) - z_k \mathbf{E} \right] - \frac{1}{T} P\nabla \cdot \mathbf{v} \tag{3.41}$$

from which one can identify an entropy flow as:

$$\mathbf{J}_s = \frac{1}{T} \left(\mathbf{J}_q - \sum_{k=1}^{n} \mu_k \mathbf{J}_k \right) \tag{3.42}$$

and an entropy source as:

$$\begin{aligned} \sigma &= \mathbf{J}_q \cdot \nabla \left(\frac{1}{T} \right) - \frac{1}{T} \sum_{k=1}^{n} \mathbf{J}_k \cdot \left[T\nabla \left(\frac{\mu_k}{T} \right) - z_k \mathbf{E} \right] - \frac{1}{T} P\nabla \cdot \mathbf{v} \\ &= \mathbf{J}_q \cdot \nabla \left(\frac{1}{T} \right) - \frac{1}{T} \sum_{k=1}^{n} \mathbf{J}_k \cdot \left[T\nabla \left(\frac{\mu_k}{T} \right) \right] - \frac{1}{T} \mathbf{i} \cdot \nabla U - \frac{1}{T} P\nabla \cdot \mathbf{v} \end{aligned} \tag{3.43}$$

Note that Relation 3.10 has been used for the electric field **E** which is derived from the time independent electric potential U. The expression of the entropy production in Equation 3.43 can be rearranged as (*62*, *64*, *70*):

$$\sigma = \mathbf{J}'_q \cdot \nabla\left(\frac{1}{T}\right) - \frac{1}{T}\sum_{k=1}^{n} \mathbf{J}_k \cdot \nabla\mu_{k,T} - \frac{1}{T}\mathbf{i} \cdot \nabla U - \frac{1}{T}P\nabla \cdot \mathbf{v} \tag{3.44}$$

By analyzing the entropy flow $\mathbf{J}_s$ in Equation 3.42, one can identify a first term related to the heat flow, $\mathbf{J}_q$, and a second one related to the diffusion flow $\mathbf{J}_k$ of components k. In the other hand, and by examining Equation 3.44 for the entropy production, one can identify four terms. The first contribution is due to the heat conduction within the gas film system, the second one is correlated to the diffusion of chemical and molecular species k, the third is due to the applied electric conditions to the system and the fourth and last one is connected to viscous flow (*62*). The nonequilibrium thermodynamics theory permits to derive condensed expression of the entropy balance equation in terms of conjugated thermodynamic fluxes and forces (*11*, *58–61*, *64*):

$$\sigma = \sum_i \mathbf{J}_i\, X_i \tag{3.45}$$

The study of the electrochemical discharge system is now restricted to a few variables which are summarized in Table 3.1. It shows that there are four phenomena of thermal, diffusional, electrical and convective effects which are at the origin of the entropy production in this physicochemical phenomenon. The contribution of the magnetic field to the entropy production is neglected. Stability analysis based on Glansdorff and Prigogine criterion (*11*) with the excess entropy production follows in Section 3.2.2.

Table 3.1.: Conjugated thermodynamical flows and forces in the entropy production of the electrochemical discharge phenomenon.

Thermodynamic flow	**Thermodynamic force**
$\mathbf{J}'_q$	$-\frac{\nabla T}{T^2}$
$\mathbf{J}_k$	$-\frac{\nabla \mu_k}{T}$
$\mathbf{i}$	$-\frac{\nabla U}{T}$
P	$-\frac{\nabla \cdot \mathbf{v}}{T}$

3.2.2. Stability Analysis

Stability study of dynamic time-dependent systems is a powerful mathematical tool for the analysis of their behavior and trends. The gas film formed around the active electrode during the electrochemical discharges is a system subject to disturbances, and stability characterizes the comportment of such a system. Moreover, its is driven far from the linear region to the nonlinear one where the thermodynamic flows are no longer linear functions of their corresponding thermodynamic forces (*71*, *72*).

3.2.2.1. Lyapunov Stability

The stability analysis of physical points under equilibrium and nonequilibrium situations is usually expressed in the Lyapunov sense of stability. The mathematician showed that certain kinds of functions other than the mechanical energy function could be used to determine stability of an equilibrium point (*73*). Mathematically, Lyapunov's stability can be formulated from Khalil (*74*) as follows:

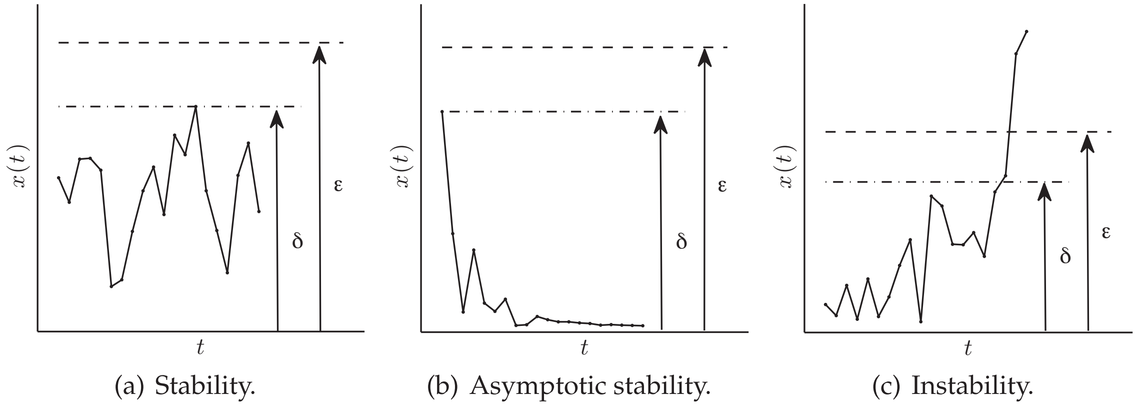

(a) Stability. (b) Asymptotic stability. (c) Instability.

Figure 3.3.: Stability (3.3(a)), asymptotic stability (3.3(b)) and instability (3.3(c)) in one-dimensional/variable space.

Definition 3.1. Let $x = 0^{\dagger}$ be an equilibrium point for the dynamical system defined by $\dot{x} = f(x,t)$, a Lipschitz map‡ from $D \subset \mathbb{R}^n$ into $\mathbb{R}^n$. The equilibrium point $x = 0$ is:

- stable if, for each $\epsilon > 0$, there is a $\delta = \delta(t_0, \epsilon) > 0$ such that:

$$\|x(t_0)\| < \delta \Rightarrow \|x(t)\| < \epsilon, \forall t \geqslant t_0 \tag{3.46}$$

- unstable if not stable.

- asymptotically stable if it is stable and δ can be chosen such that:

$$\|x(t_0)\| < \delta \Rightarrow \lim_{t \to +\infty} x(t) = 0 \tag{3.47}$$

Figure 3.3 shows an example of one-variable stability, asymptotical stability and instability situation with the concept of limiting functions δ and ϵ. It is more interesting to analyze the direct method of Lyapunov which gives information

---

[†] An equilibrium at the origin could be a translation of another equilibrium point or, more generally, a translation of another solution of the system by simply making a change of variables (*74*). Therefore, without any loss of generality, it is correct to always normalize the study and assume that the function $f(x)$ satisfies $f(0) = 0$, and to study the stability of the origin point $x = 0$ instead of another point.

[‡] Standard condition for the existence and uniqueness of solutions.

about the stability of a system without having to solve its governing time and space-dependent equations. The idea is based on the rate of change in a certain *measure of energy of the system* (*74*):

Theorem 3.2. *Let $V(x,t)$ be a locally positive definite function*[§] *with $\dot{V}(x,t)$ its total derivative along the trajectories of the system*[¶]. *The equilibrium point $x = 0$ is stable if $\dot{V}(x,t) \leqslant 0,\ \forall t \geqslant t_0$.*

The above stated Lyapunov stability theorem gives sufficient conditions for the stability of the origin of a system, however, it does not guarantee the necessity of these conditions (*73*–*75*). It does not either give directions to find proper Lyapunov functions $V(x,t)$. However, it is worth noting that the converse theorem of Lyapunov's establishes that if an equilibrium point is stable then there exists a certain function $V(x,t)$ that satisfies the condition of Lyapunov stability theorem (*75*).

3.2.2.2. -δS^2 Lyapunov Function

In the attempt to analyze the stability of the electrochemical discharges, we shall first find a Lyapunov function which satisfies the conditions of Theorem 3.2. To do so, Glansdorff and Prigogine (*11*) proceeded as follows to prove that $-\delta S^2$ is a Lyapunov function suitable for the stability analysis of far from equilibrium dissipative systems based on the excess entropy production.

Consider the power series expansion of the entropy S about an equilibrium point of the system Σ, such that (*11*, *60*, *63*, *64*):

$$
\begin{aligned}
S &= S_e + \left(\frac{\partial S}{\partial x_i}\right) dx_i + \frac{1}{2}\left(\frac{\partial^2 S}{\partial x_i^2}\right) dx_i^2 + \ldots && (3.48)\\
&= S_e + (\delta S)_e + \frac{1}{2}\left(\delta^2 S\right)_e + \ldots && (3.49)
\end{aligned}
$$

[§] A positive definite function is globally similar to an energy function.

[¶] $\dot{V}(x,t) = \frac{\partial V}{\partial t} + \frac{\partial V}{\partial x} f$

where x_i represent the set of variables on which the entropy S of the system depends, such as temperature T, volume V, mole number N_k of elements k, etc. Higher order can be neglected (*11*, *60*, *64*). In this Taylor series expansion, the term $(\delta S)_e$ represents the first order terms of the entropy about an equilibrium state containing the fluctuation terms δT, δV, δN_k, etc., while $(\delta S)_e^2$ contains the second order fluctuation terms $(\delta T)^2$, $(\delta V)^2$, $(\delta N_k)^2$ etc. The time derivative of S to the second order is:

$$\frac{\partial S}{\partial t} = \frac{\partial}{\partial t}(\delta S)_e + \frac{1}{2}\frac{\partial}{\partial t}\left(\delta^2 S\right)_e \tag{3.50}$$

First and second order terms in Equation 3.50 can be obtained for systems at thermodynamic equilibrium as follows (*11*):

$$\begin{aligned} \frac{\partial}{\partial t}(\delta S)_e &= -(\mathbf{J}_S)_e && (3.51) \\ \frac{1}{2}\frac{\partial}{\partial t}(\delta^2 S)_e &= -\nabla \mathbf{J}_S + \Phi && (3.52) \end{aligned}$$

with $\Phi = \int \sigma dV$. For systems of constant boundary conditions, the entropy balance reduces to:

$$\frac{1}{2}\frac{\partial}{\partial t}(\delta^2 S)_e = \Phi \geqslant 0 \tag{3.53}$$

where the first term in the r.h.s. of Equation 3.52 vanishes since the system reaches its maximum entropy at its equilibrium state. In other words, at the equilibrium situation of the system, the change in entropy due to fluctuations is in the second order and higher, i.e. $\delta^2 S(dx_i^2) + \delta^3 S(dx_i^3) + \ldots$, but as mentioned previously (*11*, *60*, *64*) this analysis is restricted to the second order only.

Equation 3.53 is the starting point for the study of equilibrium from the entropy balance equation (*11*, *59–61*), which is nothing but the second law of thermodynamics. Inequality 3.53 expresses an evolution criterion near equilibrium situations where both sides vanish for equilibrium states and are positive for all perturbated states.

The stability condition is therefore expressed by the fact that the system will be stable when no evolution from the unperturbed state can satisfy the requirements of the second law, which can be written as (*11*):

$$\frac{1}{2}(\delta^2 S)_e = \frac{1}{2}\int \left[\delta^2(\rho s)\right]_e \, dV = \int_{t_0}^{t_e} \Phi \, dt < 0 \tag{3.54}$$

In its local form, this can be written as:

$$\delta^2 s < 0 \text{ or } \delta^2(\rho s) < 0 \tag{3.55}$$

With the assumption of validity of local thermodynamics in equilibrium and nonequilibrium problems verified by Glansdorff and Prigogine (*11*), it is clear from the negative definitiveness of $\delta^2 s$ and $\delta^2(\rho s)$ that the approach to the stability problem of stationary nonequilibrium situations can be studied using their opposites as Lyapunov functions. In this way the stability conditions are obtained by verifying that:

$$\frac{\partial}{\partial t}(\delta^2 s) \geqslant 0\,; \quad \frac{\partial}{\partial t}\left[\delta^2(\rho s)\right] \geqslant 0, \quad \forall t \geqslant t_0 \tag{3.56}$$

The global stability of the system Σ of volume V is defined simply by:

$$\frac{\partial}{\partial t}(\delta^2 S) \geqslant 0 \quad \forall t \geqslant t_0 \tag{3.57}$$

together with the local equilibrium assumption:

$$\delta^2 S < 0 \tag{3.58}$$

3.2.2.3. Excess Entropy Production

The explicit form of the stability conditions of the gas film should take into consideration the expression of $\delta^2 S$, which in terms of specific variables can be obtained directly from Gibbs formula as:

$$\delta^2 s = \delta u \, \delta\left(\frac{1}{T}\right) + \delta v \, \delta\left(\frac{p}{T}\right) - \sum_{k=1}^{n} \delta c_k \, \delta\left(\frac{\mu_k}{T}\right) \tag{3.59}$$

and its time derivative is then expressed by:

$$\frac{1}{2}\frac{\partial}{\partial t}\left(\delta^2 s\right) = \frac{\partial}{\partial t}(\delta u) \, \delta\left(\frac{1}{T}\right) + \frac{\partial}{\partial t}(\delta v) \, \delta\left(\frac{p}{T}\right) - \sum_{k=1}^{n} \frac{\partial}{\partial t}(\delta c_k) \, \delta\left(\frac{\mu_k}{T}\right) \geqslant 0 \tag{3.60}$$

More suitable for the derivation of the stability conditions, one can write:

$$\frac{1}{2}\frac{\partial}{\partial t}\left[\delta^2(\rho s)\right] = \frac{\partial}{\partial t}\left[\delta\left(\rho u\right)\right] \delta\left(\frac{1}{T}\right) - \sum_{k=1}^{n} \frac{\partial}{\partial t}\left[\delta\left(\rho c_k\right)\right] \delta\left(\frac{\mu_k}{T}\right) \geqslant 0 \tag{3.61}$$

Let us rewrite the expressions for the terms under the time derivative in the r.h.s. of the stability condition defined by Inequality 3.61:

$$\frac{\partial \rho u}{\partial t} = -\nabla \cdot \left(\rho \mathbf{v} u + \mathbf{J}_q\right) - P\nabla \cdot \mathbf{v} + \sum_k \mathbf{J}_k \cdot \mathbf{F}_k \tag{3.62}$$

$$\frac{\partial \rho c_k}{\partial t} = -\rho_k \nabla \cdot \mathbf{v} - \nabla \cdot \mathbf{J}_k + \sum_{j=1}^{r} \nu_{kj} J_j \tag{3.63}$$

Assuming that the external forces are constant ($\delta \mathbf{F}_k = 0$), the correspondent *excess balance equations* (*11*, *59–61*) of Equations 3.62 and 3.63 are respectively written as follows:

$$\frac{\partial}{\partial t}\left[\delta\left(\rho u\right)\right] = -\nabla \cdot \left[\delta\left(\rho \mathbf{v} u + \mathbf{J}_q\right)\right] - \delta\left(P\nabla \cdot \mathbf{v}\right) + \sum_k \delta\left(\mathbf{J}_k\right) \cdot \mathbf{F}_k \tag{3.64}$$

$$\frac{\partial}{\partial t}\left[\delta\left(\rho c_k\right)\right] = -\delta\left(\rho_k \nabla \cdot \mathbf{v}\right) - \nabla \cdot \delta\left(\mathbf{J}_k\right) + \sum_{j=1}^{r} \nu_{kj} \, \delta\left(J_j\right) \tag{3.65}$$

By introducing Equations 3.64 and 3.65 into Equation 3.61, one obtains the entropy balance equation for small perturbations (*11*, *59–61*):

$$\frac{1}{2}\frac{\partial}{\partial t}\left[\delta^2(\rho s)\right] = \sigma(\delta S) - \left[\nabla\cdot\left(\delta\mathbf{J}_q\right)\,\delta\left(\frac{1}{T}\right) - \sum_{k=1}^{n}\nabla\cdot\left(\delta\mathbf{J}_k\right)\,\delta\left(\frac{\mu_k}{T}\right)\right] \tag{3.66}$$

with

$$\sigma(\delta S) = \sum_i \delta\mathbf{J}_i\,\delta X_i \tag{3.67}$$

where $\mathbf{J}_i$ and X_i are given in Table 3.1. For any boundary conditions, as $-\delta^2 S$ is as a Lyapunov function, a given nonequilibrium stationary state is stable if (*11*, *64*):

$$\begin{cases} \frac{1}{2}\frac{\partial}{\partial t}(\delta^2 S)_e = \Phi = \int \sum_i \delta\mathbf{J}_i\,\delta X_i\,dV \geqslant 0, \quad \forall t \geqslant t_0 \\ -\int\left[\nabla\cdot\left(\delta\mathbf{J}_q\right)\,\delta\left(\frac{1}{T}\right) - \sum_{k=1}^{n}\nabla\cdot\left(\delta\mathbf{J}_k\right)\,\delta\left(\frac{\mu_k}{T}\right)\right] dA \geqslant 0, \quad \forall t \geqslant t_0 \end{cases} \tag{3.68}$$

However, if Inequalities 3.68 are not satisfied, it is a necessary but not sufficient condition for the instability of the system.

3.3. Stability of Electrochemical Discharges

The application of stability conditions to the electrochemical discharge phenomenon is automatically obtained by considering the Lorentz force as the external force in the conservation of energy equation. Moreover, and for the sake of simplicity, the boundaries of the system consisting on the sequential domains: electrode, gas film and bulk solution are considered to be fixed (Figure 3.1(a)). With this assumption that the l.h.s of Relation 3.68 vanishes, the explicit stability condition writes that the nonequilibrium steady state is stable if the excess entropy production of the system is positive for any time t greater than t_0, the time at which a perturbation occurred

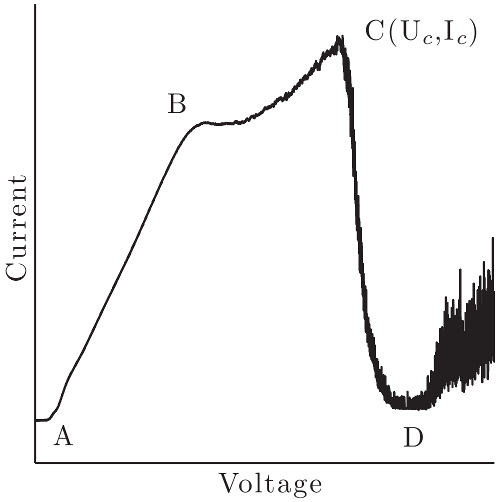

Figure 3.4.: Quasi steady state current-voltage characteristics of the electrochemical discharge phenomenon.

(*11*, *58*, *60*):

$$\Phi = \int \sum_i \delta \mathbf{J}_i \, \delta X_i \, dV \geqslant 0, \quad \forall t \geqslant t_0 \tag{3.69}$$

where Φ is expressed by (see Equation 3.44 and Table 3.1):

$$\Phi = \int \left\{ \delta \mathbf{J}'_q \cdot \delta \left[\nabla \left(\frac{1}{T} \right) \right] - \sum_{k=1}^{n} \delta \mathbf{J}_k \cdot \delta \left[\frac{1}{T} \nabla \left(\mu_{k,T} \right) \right] - \delta \mathbf{i} \cdot \delta \left(\frac{\nabla U}{T} \right) - \delta P \cdot \left(\frac{\nabla \cdot \mathbf{v}}{T} \right) \right\} dV \tag{3.70}$$

For simplicity, the last term in the r.h.s. of Equation 3.70, due to the mechanical work, will be neglected so that the excess entropy production is expressed by (*68*, *76*, *77*):

$$\Phi = \int \left\{ \delta \mathbf{J}'_q \cdot \delta \left[\nabla \left(\frac{1}{T} \right) \right] - \sum_{k=1}^{n} \delta \mathbf{J}_k \cdot \delta \left[\frac{1}{T} \nabla \left(\mu_{k,T} \right) \right] - \delta \mathbf{i} \cdot \delta \left(\frac{\nabla U}{T} \right) \right\} dV \tag{3.71}$$

The stability discussion of the gas film is based on Figure 3.4, which illustrates a typical stationary *i*-*U* characteristics for cathodic discharges (*68*, *77*). In the initial region *A*-*C* of the current-voltage behavior, which corresponds to the conventional water electrolysis, the electric current increases accordingly with the applied potential difference. From the surface of the electrode to the electrolyte, the temperature gradient rises as well, due to the increase of the current density because of the growing number of gas bubbles nucleated at the surface (*16*). From Glansdorff and Prigogine stability criterion expressed by the the second order variation of $\dot{S}$ in Equation 3.71, motion along this steady state region is stable with respect to small deviations from a fixed point belonging to this trajectory.

In the following region *C-D*, no sufficient condition of stability can be obtained from the excess entropy production criterion. Experimental evidence shows, however, that this region is an unstable situation where any fixed voltage within this zone does not guarantee a well-defined stationary current value. On the contrary, the system exhibits bi-stable behavior (*78*) in region *C-D* where there are two stable and one unstable trajectories. In other words, the critical point *C* is a bifurcation point where the system choses to follow a new way of order. The stable region *A-C* of conventional electrolysis loses its stability and is succeeded by two stable branches (*68*, *76*, *77*). The system follows a behavior similar to the one illustrated in Figure 3.5 which represents the bifurcation diagram for the supercritical pitchfork bifurcation. The branch between the two stable ones is unstable for $\lambda > 0$, the critical point[‖]. Actually, a relay, also known as the passive or positive-kind of hysteresis[**], is identified by monitoring the current at forward and reverse scan of the cell voltage (*68*, *76*, *77*).

Once the region *C-D* is passed, and with further increase of the terminal voltage, another state of order is observed. The following discussion on the stability of the electrochemical discharge phenomenon is organized on the contributions of each of the terms in Equation 3.71.

[‖] A similar example is to consider a metal rod with a weight attached on it that can translate along its length. When the rod is set vertical, and depending on the height of the weight, it can either stand straight or bend to the left or to the right. In both situations, any perturbation will cause the oscillation of the rod around its actual equilibrium situation.

[**] The existence of multiple stable branches allows hysteresis and jumps from one branch to another.

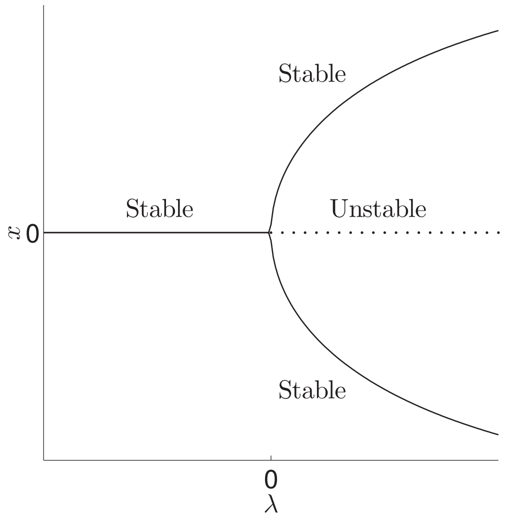

Figure 3.5.: Supercritical pitchfork bifurcation diagram.

First, let us rewrite the heat transfer term of Equation 3.44 over the x-axis pointing to the right:

$$\Phi_{q,x} = \int_0^d J'_q \frac{\partial}{\partial x}\left(\frac{1}{T}\right) dx \tag{3.72}$$

where d being the gas film thickness. If we denote the heat capacity at constant volume of the the gas film by C_v and its equivalent heat conductivity constant by k, the heat diffusion equation in the gas film is written as:

$$\rho C_v \frac{\partial T}{\partial t} = \frac{\partial}{\partial x}\left(k \frac{\partial T}{\partial x}\right), \quad 0 < x < d, \forall t \geqslant 0 \tag{3.73}$$

The time derivative of $\Phi_{q,x}$ is expressed by combining both Equations 3.72 and 3.73 to obtain:

$$\frac{d\Phi_{q,x}}{dt} = \delta^2 S = -2\int_0^d \frac{\rho c_v}{T^2}\left(\frac{\partial T}{\partial t}\right)^2 dx = -\frac{2\rho C_v d}{T^2}(\delta T)^2 < 0 \tag{3.74}$$

which is valid in both equilibrium and nonequilibrium situations (*11*, *59*). The entropy production of the stationary state is function of $(\delta T)^2$ tends to zero in the course of time. Now the excess entropy production due to the heat transfer term

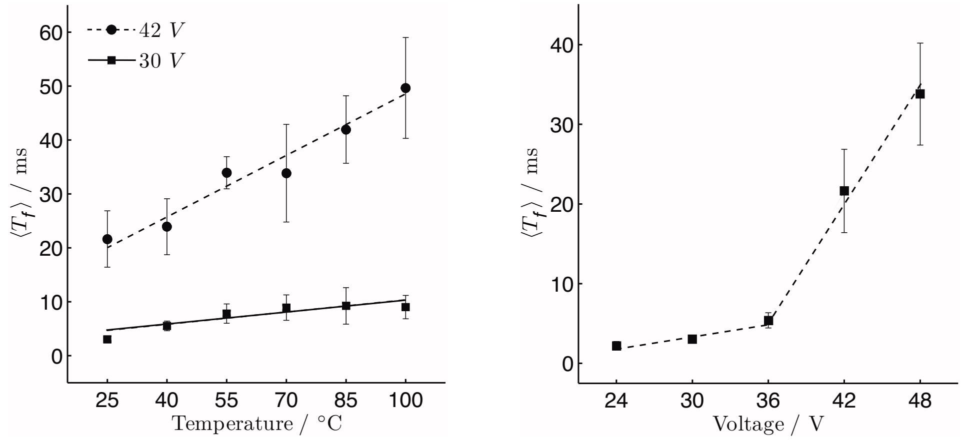

(a) Variation of $\langle T_f \rangle$ with the temperature at the terminal voltages 30 and 42 V.

(b) Variation of $\langle T_f \rangle$ with the voltage at 25°C bulk temperature.

Figure 3.6.: Variation of gas film life-time function of the temperature for 30 and 42 V (3.6(a)) and of the voltage at 25°C bulk temperature (3.6(b)) in NaOH 30% wt. aqueous solution.

can be expressed as:

$$\frac{1}{2}\frac{\partial}{\partial t}(\delta^2 S) = \int_0^d \delta J'_q \, \delta\left[\frac{\partial}{\partial x}\left(\frac{1}{T}\right)\right] dx = \int_0^d \frac{k}{T^2}\left[\frac{\partial}{\partial x}(\delta T)\right]^2 dx \geqslant 0, \quad \forall t \geqslant t_0 \tag{3.75}$$

The excess heat conduction contribution is always positive for any change in the gas film temperature and contributes positively to the overall excess of entropy production of the system so that it converges to its stable branch. Additionally, there is a tendency of the system to be more stable at higher bulk temperatures. Figure 3.6(a) shows the increase of the mean value of the gas film life-time, $\langle T_f \rangle$, with the increase of the bulk solution temperature in a NaOH 30% wt., for two fixed terminal voltages, 30 and 42 V. The description of the experimental methods to determine the random variable $\langle T_f \rangle$ are detailed in Chapter 4. Two results are drawn from the plots of Figure 3.6(a):

1. the random variable $\langle T_f \rangle$ is always greater at higher bulk temperature for a fixed voltage, and
2. $\langle T_f \rangle$ is always greater at 42 V than at 30 V for the same fixed bulk temperature, which is further confirmed by Figure 3.6(b) where the mean gas film life-time is computed at different voltages from 24 to 48 V at a bulk temperature of 25°C.

The second term in Equation 3.71 refers to the change in mass fluxes through the gas film boundaries. The time continuous mass transfers are needed to maintain the electrochemical discharge phenomenon, as it is far from thermodynamic equilibrium observable. The Glansdorff and Prigogine criterion of stability ensures that if the change in mass gradients of the sum of components k is growing, then the steady state of the electrochemical system is stable. The possible convective movements in the gas film which may enhance the mass transports and contribute more effectively to the stability of the phenomenon are not taken into account in Equation 3.71. The estimation of the mass transfer term is not unambiguous as it requires precise identification of the chemical species, their flowing directions, velocities, as well as their chemical affinities (*68*, *76*, *77*).

The last term, $\int \left\{ -\delta \mathbf{i} \cdot \delta \left(\frac{\nabla U}{T} \right) \right\} dV$, in the excess entropy production also contributes positively to the function and to the stability of the system. In this term, it is the current vector which is the variable of interest. On one side, there is the current due to electrochemical charge transfer on the free electrode sites. On the other side, in the portion covered by the gas film, electric discharges contribute to the total current. This second contribution will give a positive entropy production as here the current is increasing with the terminal voltage and consequently the gas film life-time $\langle T_f \rangle$. The first type of current can be expressed by a mean field model based on the mass balance of the gas evolving electrode (*2*, *32*). This model computes the time evolution of the bubble coverage fraction θ. From Wüthrich (*2*), the stationary solution is given by the solution of the following equation:

$$\frac{d\theta}{dt} = \frac{p_c}{1-p_c}\mathcal{U}(1-\theta) - \left[\sum_{s=0}^{s_{max}} sn_s(\theta) + \tau P(\theta)\right] = 0 \tag{3.76}$$

with $\sum_{s=0}^{s_{max}} sn_s(\theta)$ the sum product of cluster size s by the normalized cluster number n_s over the cluster sizes 0 to ${s_{max}}^{\dagger\dagger}$, τ the ratio between the mean gas detachment period from the electrode surface and the mean gas film life-time, p_c is the percolation threshold and $\mathcal{U}$ the normalized voltage defined by:

$$\mathcal{U} = \frac{U - U_A}{U_C - U_A} \tag{3.77}$$

with U_A the water decomposition potential. The term $\sum_{s=0}^{s_{max}} sn_s(\theta)$ can be evaluated using the percolation theory. For example, for the Bethe lattice with three branches with the assumption $s^{max} \to \infty$, one can write:

$$\sum_{s=0}^{s_{max}} sn_s(\theta) + \tau P(\theta) = \begin{cases} \theta, & \mathcal{U} < 1 \\ \\ \frac{(1-\theta)^3}{\theta^2} + \tau\left[\theta - \frac{(1-\theta)^3}{\theta^2}\right], & \mathcal{U} \geqslant 1 \end{cases}$$

The normalized mean stationary *i-U* behavior according to this model can then be computed as follows:

$$i_1 = \frac{1-\theta}{1-p_c}\mathcal{U} \tag{3.78}$$

The second model to be considered is the cold field electron emission (CFE), which from Fowler and Nordheim's tunneling theory (*79–81*), its empirical expression in *i-U* form obeys:

$$i_2 = \mathrm{C}\mathrm{U}^{\kappa} \exp\left(-B/\mathrm{U}\right) \tag{3.79}$$

[††] s_{max} is a critical value of the cluster size beyond which the bubbles in a gas evolving electrode system are fully adherent to the electrode surface and are not able to detach anymore.

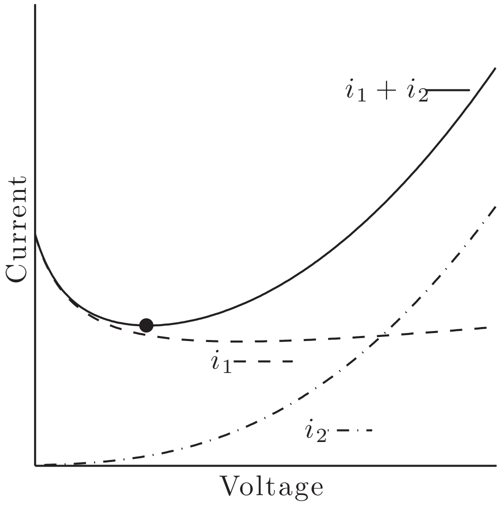

Figure 3.7.: Current-voltage evolution during the discharge regime ($i_1 + i_2$) according to the integral electrochemical model (i_1) and to the cold field electron emission from metals (i_2).

where B, C and κ are experimental constants. Considering the sum of both electrochemical and CFE models, the mean-field *i-U* characteristics is represented qualitatively in Figure 3.7, where the $i_1 + i_2$ curve shows two regions delimited by a global minimum. Before this minimum, the electric term in Equation 3.71 contributes with a negative part to the excess entropy production. If this contribution is higher, in absolute value, than the other two terms in Equation 3.71, the system may potentially be destabilized. After this minimum, the electric term will contribute positively and therefore stabilizes the system. In summary, high temperature gradients and the electrical discharges enhance the stability of the electrochemical discharge phenomenon. Together, the sum of these two contributions to the excess entropy production can overcome the negative one due to the negative resistance of the system once the gas film starts to be formed (*68*, *76*, *77*).

3.4. Conclusion

By writing the entropy balance equation in terms of conjugated thermodynamic fluxes and forces, the study of the electrochemical discharges is now condensed to a few global variables. Focusing on the heat, mass and charge transfers should suffice to study and describe the behavior of the electrochemical discharges. From the stability discussion of the system based on the excess entropy production, with $-\delta S^2$ as a Lyapunov function, it is concluded that small perturbations in both electrochemical and thermal phenomena contribute to the stability of the far from thermodynamic equilibrium stationary state.

The thermodynamic analysis presented in this Chapter succeeds in describing the electrochemical discharges from a macroscopic time-independent viewpoint. From the steady state trajectory followed by the system, its stability analysis is essential so that the process can be used in more effective and controllable manners for its numerous applications. To complete the description, knowing that in real situations the current timeseries signal is far from being steady, there is a need to look at the short time scale behavior of the phenomenon. The gas film dynamic analysis of Chapter 4 is therefore the logical complementary study of the steady-state thermodynamic description of the electrochemical discharges.

Chapter 4

Gas Film Dynamics

> *What then is time? If no one asks me, I know what it is. If I wish to explain it to him who asks, I do not know.*
>
> *(Saint Augustine)*

Describing the gas film dynamics during the electrochemical discharge phenomenon, or more explicitly its time-dependent variables, has potential applications to deepen the understanding of the contact glow discharge electrolysis, micro-machining by spark-assisted chemical engraving (SACE) technique as well as nanoparticle synthesis. For example, it is known from Wüthrich and Hof (*82*) that geometric discontinuities and the non-regularity of the resulting shapes by SACE machining are related to the gas film stability and also to the current intensity. Indeed, while the gas film is at the onset of the discharge regime and is necessary for the machining by thermo-chemical effects, its intermittent presence affects the geometric quality of the produced structures in the work piece. Thus, studying the distribution of the gas film life-time and its formation time in the current signal of the discharge regime gives valuable information on the process and its alternating stable-instable states. The approach is experimental with wavelet signal processing tools complemented with statistically-based analysis of pre-defined random variables. It is understood that the study and experimental investigations of the gas film dynamics of this Chapter are the time-dependent validation of the results obtained in Chapter 3 about the thermodynamic description and the gas film stability conditions.

4.1. Current Signal

Figure 4.1 illustrates a sample of current timeseries response during the electrochemical discharges. The signal is collected by an Agilent current probe model N2774A–50MHz recorded wit a Newport XPS hardware/software system (Universal High-Performance Motion Controller–Driver) at a sample rate of 10 kS per second. The electrochemical cell is composed of a ⌀0.5 mm stainless steel 316 L grade cathode concentric with a ⌀7 cm stainless steel 304 grade ring immersed in a 100 ml of 30 wt.% NaOH aqueous solution. The cathode immersion depth in the solution is of 2 mm and the applied constant terminal voltage is set to 32 V.

While acquiring the current signal, one can identify the formation of a gas film prior to each series of discharges. The large time period shape of 2.3 ms characterizes the gas film formation-time in the current timeseries signal, while the high frequency pulses characterize the electrochemical discharges activity. The signal is stochastic where both gas film formations and discharges have non-constant magnitudes, formation times and frequencies of appearance in the signal. The intensities of the discharges may surpass those of the gas film formations.

Quantitative studies about the gas film dynamics, in particular through the estimation of the mean gas film life-time are the purpose of this Chapter. Reliable signal processing algorithms which allow the proper identification of the various gas film formation peaks in the current signal are needed. Due to the stochastic nature of the current response, it is essential to ensure that the signal's time- and frequency-based views are not altered by the applied algorithmic logics. The precise

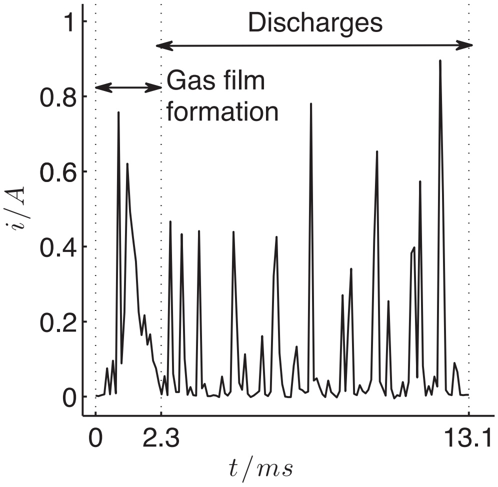

Figure 4.1.: Current signal during the electrochemical discharge phenomenon.

identification of the gas film formation has to be preceded by filtering out the discharge pulses to *de-noise* the signal. The second constraint is to keep the low frequency part of the signal, which corresponds to the gas film formations, without loss of information about the time- and frequency-based views.

Descriptive statistics of the gas film formation-time and life-time can provide valuable information about its stability and instability, so it should constitute a part of the presented algorithm. To do so, let us define the following random variables necessary for the analysis of the current signal:

- T_f: random variable defining the time interval between two successive gas film formations, also called the gas film life-time.
- T_g: random variable defining the formation-time or the building-time of a gas film .
- ΔT: random variable defining the time interval between two successive gas film formations maxima.

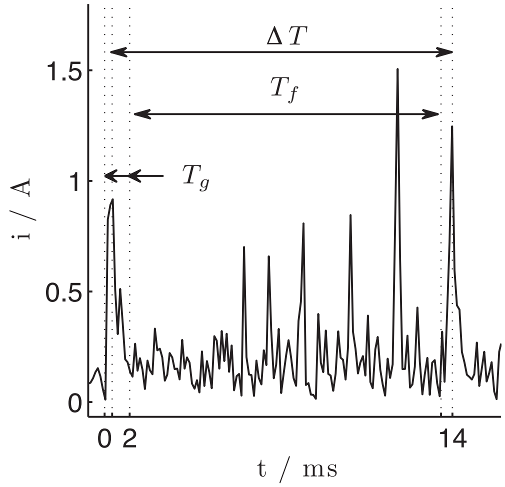

Figure 4.2.: Definition of the random variables T_f for the gas film life-time, T_g for the gas film building-time and ΔT for the time between the maxima of two successive gas film formations.

These random variables are illustrated on a real current signal shown in Figure 4.2. The time window shows two gas film formations, the local maxima of which are separated by the time ΔT. The first gas film formation presents a small perturbation in its current signal. Several discharges can be identified in the signal, especially the one with higher magnitude that the gas film formations.

4.2. Wavelet Analysis Algorithm

Approximation using superposition of functions has existed since the early 18th century, when Joseph Fourier discovered that functions can be represented using the superposition of sines and cosines. Fourier laid the foundations of signal processing with his theory of frequency analysis, which is very important and influential in various scientific fields. However, the bases of Fourier analysis, namely the trigonometric functions sines and cosines, are non-local functions and therefore are not very accurate in sharp discontinuities approximation which are the main features of the current signal during the discharge regime, as illustrated in both Figures 4.1 and 4.2.

The focus of mathematicians like Alfred Haar, Jean Morlet, Yves Meyer, Stephane Mallat, Ingrid Daubechies and Ronald Coifman, to cite a few, gradually turned from the frequency-based analysis to scale-based analysis. Indeed, an approach measuring average fluctuations at multi-scale or multi-resolution analysis is less sensitive to noise when compared to frequency analysis. With the wavelet analysis which uses local mother wavelets i.e. contained in finite domain, one can look at the signal from large and small windows according to different scales or resolutions.

Wavelet algorithms for temporal analysis are performed with a high frequency version of the base function, while frequency analysis is performed with a low frequency version. This property is the main point that favors the use the wavelet analysis in the proposed algorithm instead of Fourier analysis, knowing that the gas film formations will represent the low frequency part of the signal while the discharges will represent its high frequency part. Other issues are that the gas film formations are subject to large fluctuations and consequently applying a simple low-pass filtering method will deform the original signal. The discharges have various amplitudes, as illustrated in Figure 4.2, which excludes the option of using a global threshold for the signal.

Wavelet-based signal processing algorithms are firstly applied to simulated signals of known statistics. After validation of the algorithm, series of experimental data analysis are conducted. As it concerns the gas film stability, the results support previous contributions (*16*, *18*, *82*–*84*) and especially the dual combination of thermal and electrochemical effects developed and discussed in Section 3.3. The proposed algorithm can be extended to discuss the electrochemical discharge activity by considering the high frequency feature of the timeseries current signal, but it is not the purpose here. Other techniques have been applied to the study of the discharges and can be found in Wüthrich (*83*) and in Wüthrich et al. (*55*).

4.2.1. Definition

Definition 4.1. Consider the family of functions for wavelet analysis $g_{p,a}(t) = \frac{1}{a}\bar{g}\left(\frac{t-p}{a}\right)$ where $p \in \mathbb{R}$ represents a position or a translation, $a \in \mathbb{R}_+$ with $a \neq 0$ is a scaling number and $\int g = 0$. The wavelet transform of a function s with finite energy such that $s \in L^i(\mathbb{R})$, $i \in [1; +\infty[$, with the condition $\|s\| < \infty$ is defined by the scalar product $\langle g_{p,a}|s\rangle$ over $\mathbb{R}$ such that (*85*, *86*):

$$\mathbb{W}_g s\,(p,a) = \langle g_{p,a}|s\rangle = \int_{-\infty}^{+\infty} dt\; \frac{1}{a}\bar{g}\left(\frac{t-p}{a}\right)s(t) \tag{4.1}$$

The numbers $\mathbb{W}_g s\,(p,a)$ are called the wavelet coefficients of s with respect to the mother wavelet function g.

Suppose V_j to be a multi-resolution or multi-scale analysis over $\mathbb{R}$ with its associated wavelet spaces W_j of the signal s. The orthogonal projections of V_j and W_j will be called P_{v_j} and P_{w_j} respectively. Suppose $s \in V_0$ a function over $\mathbb{R}$. One may then decompose s without loss of information into sequence of functions according to (*86*):

$$s_{LF}^{(j+1)} = P_{v_{-(j+1)}} s_{LF}^{(j)} \quad \text{and} \quad s_{HF}^{(j+1)} = P_{w_{-(j+1)}} s_{LF}^{(j)} \tag{4.2}$$

with $s_{LF}^{(0)} = s$. This is to say that at each step one splits the low frequency part or approximation $s_{LF}^{(j)}$ into a part with still lower frequencies $s_{LF}^{(j+1)}$ and a part with high frequencies $s_{HF}^{(j+1)}$ that have been removed by passing from level j to level $j+1$. This is an orthogonal decomposition scheme of a one-dimensional function or signal.

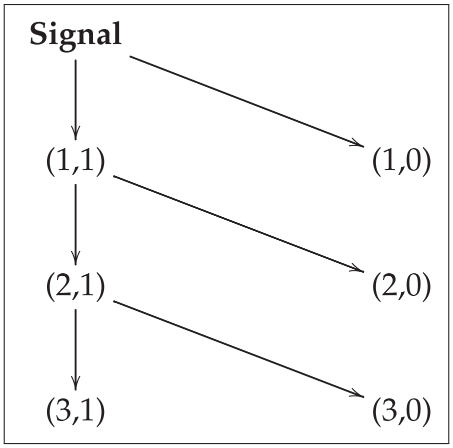

Figure 4.3.: Scheme of a three-level orthogonal tree decomposition of a signal.

A three-level orthogonal decomposition follows a scheme as illustrated in Figure 4.3. The original signal is localized at the upper node. The first coordinate of the nodes is the level of decomposition of the original function while the second one is to say whether the output signal belongs to the *details* or to the *approximation* group. The first level of decomposition yields two different signals of the same length as the original one; the detail signal is located at node (1,0) and the approximation is at (1,1). The signal (1,1) is then split onto two other signals, approximation and details, until the required level of decomposition is reached. The reconstruction of the original signal from the different approximations and details is obtained by simple additions. For example, to reconstruct the original signal in the tree represented by Figure 4.3, one has to simply make the addition of the signals in nodes (3,1), (3,0), (2,0) and (1,0). It is understood that for the study of the gas film dynamics it is the last signal of the approximation group which is analyzed. On the contrary, if one is interested by discharge dynamics, signals from the details group are more appropriate.

4.2.2. Algorithm

The algorithm for the study of the gas film dynamics is composed of two parts:

1. denoising the signal from the discharges by wavelet transformation based on decomposition and reconstruction algorithms,
2. detection of the well-chosen local peaks in the denoised signal to describe the gas film dynamics.

The choice for the base function for the wavelet transformation is for the discrete approximation of Meyer wavelet, defined in the frequency domain by the wavelet function $\hat{\psi}$ and the scaling function $\hat{\phi}$ as follows (*85*):

$$\hat{\psi}(f) = \begin{cases} \frac{e^{(if/2)}}{\sqrt{2\pi}} \sin\left[\frac{\pi}{2}\nu(a)\left(\frac{3}{2\pi}|f|-1\right)\right], & \frac{2\pi}{3} \leqslant |f| \leqslant \frac{4\pi}{3} \\ \frac{e^{(if/2)}}{\sqrt{2\pi}} \cos\left[\frac{\pi}{2}\nu(a)\left(\frac{3}{4\pi}|f|-1\right)\right], & \frac{4\pi}{3} \leqslant |f| \leqslant \frac{8\pi}{3} \\ 0, & \text{otherwise} \end{cases} \tag{4.3}$$

$$\hat{\phi}(f) = \begin{cases} \frac{1}{\sqrt{2\pi}}, & |f| \leqslant \frac{2\pi}{3} \\ \frac{1}{\sqrt{2\pi}} \cos\left[\frac{\pi}{2}\nu(a)\left(\frac{3}{2\pi}|f|-1\right)\right], & \frac{2\pi}{3} \leqslant |f| \leqslant \frac{4\pi}{3} \\ 0, & |f| > \frac{4\pi}{3} \end{cases} \tag{4.4}$$

with $\nu(a) = a^4\left(35 - 84a + 70a^2 - 20a^3\right)$ and $a \in [0,1]$. Figure 4.4 illustrates the Meyer wavelet function (Figure 4.4(a)) and the Meyer scaling function (Figure 4.4(b)) in the interval $[-3\pi; +3\pi]$. Mayer wavelet is a fast convergent function which allows

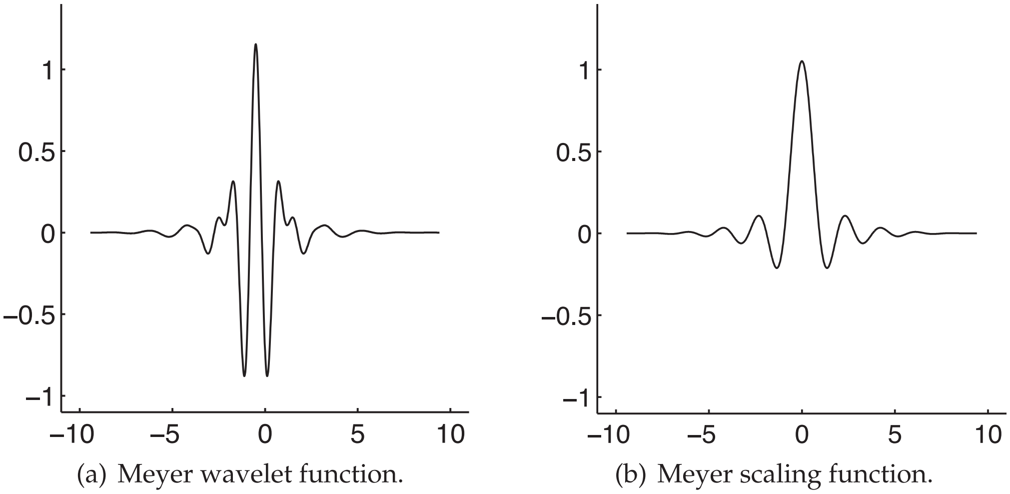

(a) Meyer wavelet function.

(b) Meyer scaling function.

Figure 4.4.: Meyer wavelet (4.4(a)) and scaling (4.4(b)) functions in $[-3\pi; +3\pi]$.

better quantification of both time and frequency localizations. It also constitutes an orthogonal basis and has the regularity advantage which is very suitable to obtain smoother features in the processed signal. To avoid non necessary large size data resulting from the continuous wavelet transform, the discrete version of Meyer wavelet for the decomposition step is chosen. Inverse transform using dyadic scales and positions are used for the reconstruction step (*87*).

The approximated signal obtained from the first part of the algorithm is scanned to find all the local extrema using the center-clipping technique. Proper decision logic is applied to distinguish between peaks and valleys. However, with this procedure, local discontinuities during the gas film formation are detected as well and may be identified wrongly as electrochemical discharges. To properly attribute the identified extrema to the gas film formation or to an electrochemical discharge, the following criteria are used. It is considered that successive extrema having an amplitude change below 50% do still be part of the gas film formation signal. If, on the contrary, two successive extrema will drop by more than 50%, the end of the gas film formation is reached. The value of 50% is chosen based on a theoretical

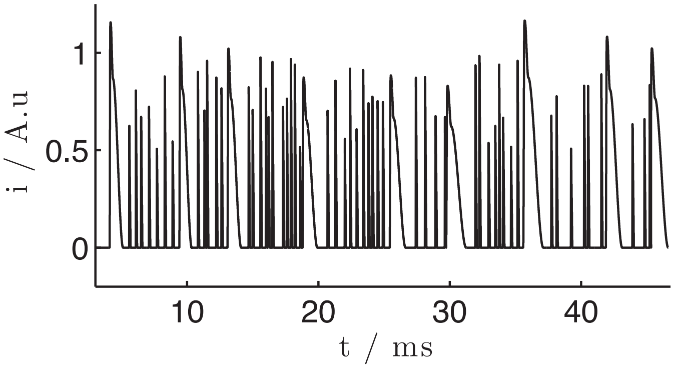

(a) Original signal.

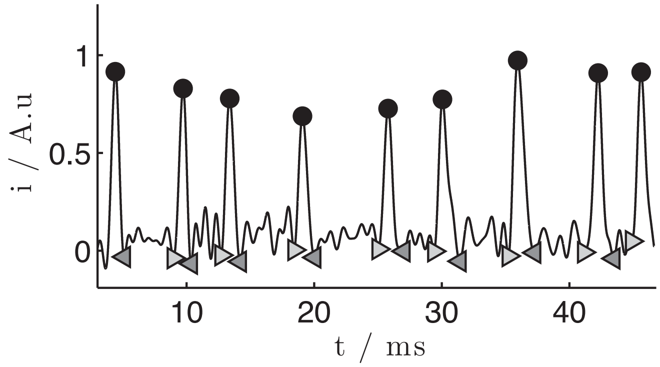

(b) Approximated signal.

Figure 4.5.: Generated signal (4.5(a)) decomposed to and reconstructed from the 12th level by the discrete Meyer wavelet transform, and detection of well-chosen extrema (4.5(b)), adapted from Allagui and Wüthrich (*88*).

model for the description of the gas film formation (*83*). The computation of the three random variables of interest is detailed in Appendix A (*88*).

Figure 4.5(a) shows a simulated signal where the low frequencies represent the gas film formations and the high frequencies represent the discharges. The gas film formation shape has been approximated by a B-spline function inspired from experimental observations (see Figure 4.1 or 4.2). The simulation is performed using realistic values of the durations and frequencies of gas films and discharges observed from experimental data. The plot in Figure 4.5(b) shows the output of the two steps of the algorithm:

1. decomposition–reconstruction by the discrete Mayer wavelet.
2. detection of the needed points in the signal to estimate the three random variables ΔT, T_f and T_g.

4.3. Characterization and Validation

The characterization procedure for the robustness of the proposed algorithm is performed by means of applying the algorithmic steps to five different simulated timeseries signals. The gas film formation shapes have been approximated by five different functions: rectangular, Barlett, Bohmann, sum of cosine functions of different frequencies (see Figure 4.6), and a B-spline function built according to experimental observations of gas film shapes (see Figure 4.5).

The results show that the proposed decomposition–reconstruction algorithm, using the discrete wavelet transform analysis with the Meyer wavelet as mother function, is unbiased and very accurate for the analysis of the gas film life-time and formation-time distributions in real signals. Figure 4.7 illustrates the descriptive statistics of a simulated signal similar to the one in Figure 4.5, as well as its processed version by wavelet transform.

The time interval between the maxima of two successive gas film formations was chosen Gaussian distributed with mean μ and variance σ^2. To reproduce realistic signals, typical values of μ around 5 ms and σ^2 around 1 ms were selected. In the time intervals between each two successive gas film formations the electrochemical discharges has been inserted. These later have been assimilated to a pulse train where the frequency of appearance follows a Poisson distribution of parameter $\lambda = 2$ discharges per millisecond.

The amplitudes of the gas film formation, of the discharges and the gas film building-time were not taken constant. After normalization of the signal according

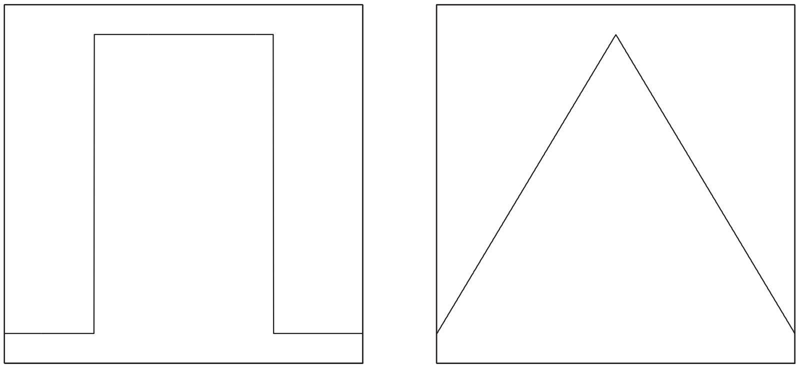

(a) Rectangle (b) Bartlett

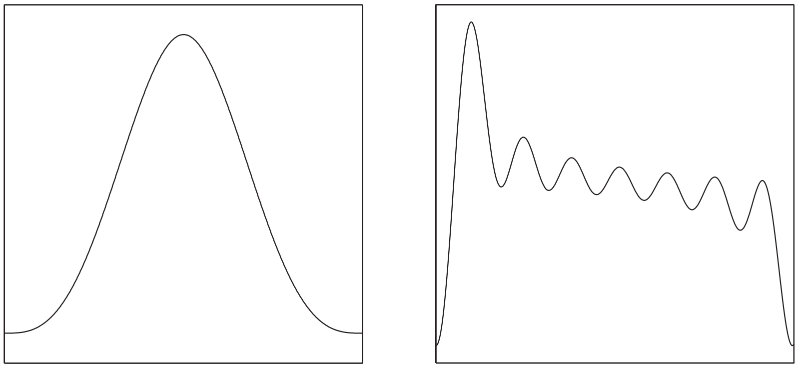

(c) Bohman (d) $\Sigma_i \sin(ix)$

Figure 4.6.: Tested gas film formation shapes for the characterization and validation of the algorithm.

to a fixed arbitrary unit, the gas film formation height and the amplitude of the discharges have been varied according to a uniform distribution between 67% and 133% ($\pm\sigma$) of their normalized height. The same procedure has been performed with the gas film formation time which is taken uniformly distributed between 80% and 120% of 2 ms.

While generating the signal, the normally distributed random variable ΔT was recorded. This original signal is the input of the algorithm presented above. Figure 4.7(a) shows a typical example of the ΔT distribution with a signal containing 200 gas film formations. The same distribution for the processed signal is shown in Figure 4.7(b). Note the excellent agreement of both distributions. The scatter plot in

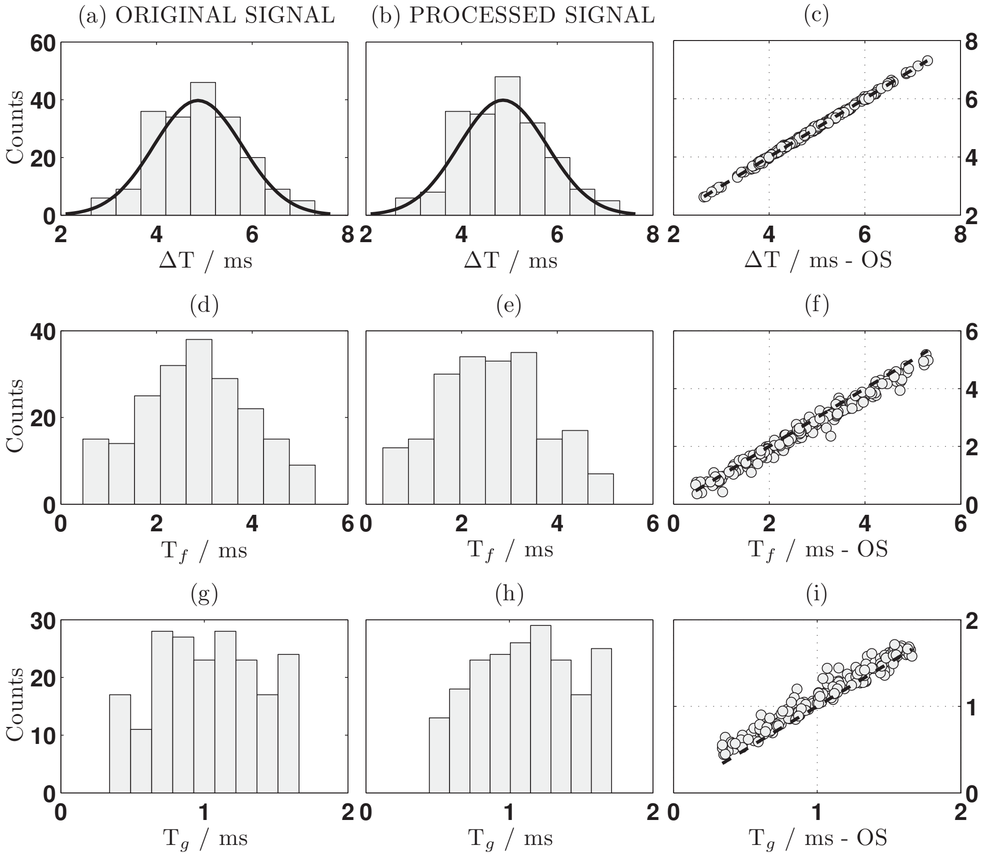

Figure 4.7.: Histograms of the random variables ΔT (a-b), T_f (d-e) and T_g (g-h) determined from the original and processed signals. The linearity of the scatter plots (c-f-i) demonstrates the correspondence of the different events, adapted from Allagui and Wüthrich (*88*).

Figure 4.7(c) shows that the random variable ΔT calculated from both original and processed data follow the same Gaussian distribution.

The probability distributions of the random variable gas film life-time T_f, calculated from the original and processed signals are shown in Figure 4.7(d) and Figure 4.7(e) respectively. The points cloud in Figure 4.7(c) is within a narrow bandwidth around the main diagonal represented by the dashed line. The same conclusion holds for the random variable T_g which represents the gas film formation-time distribution. The output of the algorithm shows in Figure 4.7(h) that the distribution of T_g collected from the processed signal is following a uniform distribution which

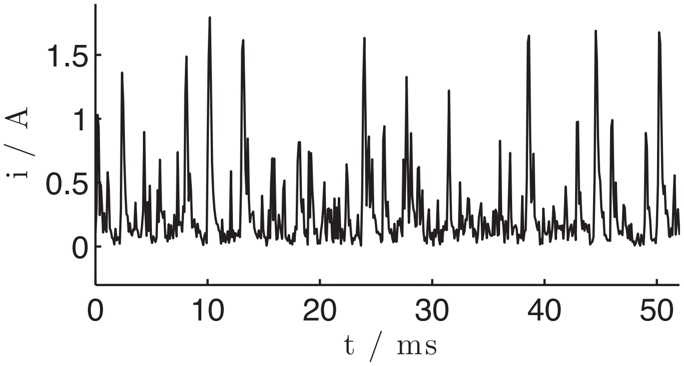

(a) Original signal.

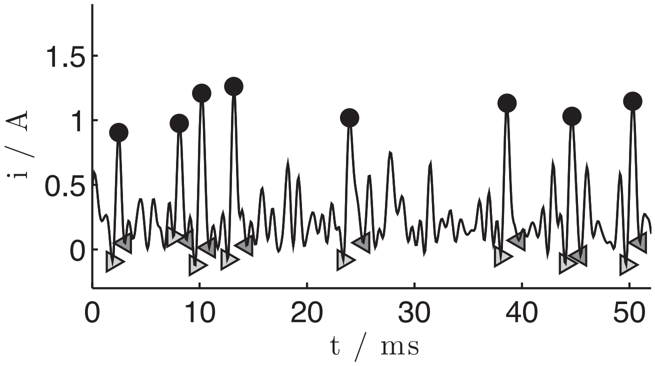

(b) Reconstructed signal.

Figure 4.8.: Real signal (4.8(a)) decomposed to and reconstructed from the 2nd level by the discrete Meyer wavelet transform, and detection of well-chosen extrema (4.8(b)) for the gas film dynamics study, adapted from Allagui and Wüthrich (*88*).

corresponds to the one in Figure 4.7(g) from the original signal. The last scatter plot also confirms the data correspondence between the two signals.

4.4. Application to Actual Timeseries Signals

The experimental conditions to collect the current signals during the electrochemical discharges are the same as detailed previously is Section 4.1. Figure 4.8 illustrates a typical example of the result of the acquired signal and its analysis, zoomed on a short time portion. The signal acquisition for this sample is at a fixed terminal

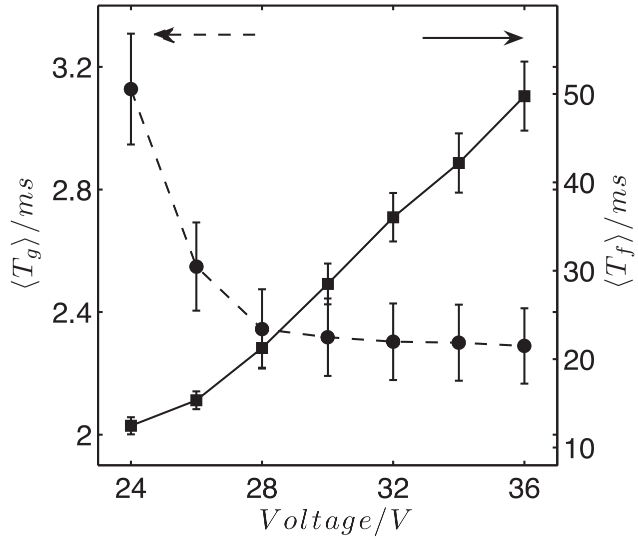

Figure 4.9.: Gas film life-time and gas film formation-time in NaOH 30% wt. aqueous solution, adapted from Allagui and Wüthrich (*88*).

voltage of 24 V. By applying the decomposition–reconstruction step of the algorithm and identifying the local peaks and the well-chosen local minima, one ends up with the processed version of the original signal shown in Figure 4.8(b). The mother wavelet is the discrete Mayer wavelet and the signal is decomposed to the second level. Note the excellent correspondence between the two time series plots, especially for the required local extrema needed for the calculation of three random variables ΔT, T_f and T_g.

The evolution versus terminal voltage of the means of the two random variables T_g and T_f, calculated from one set of experiments, composed of signals of 400 s length for each voltage, is plotted in Figure 4.9. The error bars included in the plots represent the standard deviation of the experimentally measured probability distributions around the mean values. The order of magnitude of T_g is grater than the order of magnitude of T_f by at least one-fold. The mean gas film life-time is gradually increasing with the voltage while the mean gas film formation-time follows the opposite trend.

The evolution of mean value of T_g shows that the gas film life-time is more stable at high voltages than at low voltages. This observation is in close agreement with the qualitative observations done by Kellogg (*16*). This author noted, on one hand that the electrode temperature increases with the terminal voltage, and on the other hand that at high electrode temperatures, the gas film is quite uniform and seems to be more stable than at lower temperatures. This also confirms the nonequilibrium thermodynamic results based on the excess entropy production criterion os stability in Chapter 3.

Additionally, the electronic transfer from the surface of the working electrode to the electrolyte is related to the mobility of ions in the gas film. The kinetic energies of these charges are not high enough to carry large current densities. As a result, the discharges tend to be an avalanche process of multiplication to occupy larger volumes around the electrode by establishing multiple electronic pathways. Indeed, when the applied voltage is increased, it is observed visually that the volume occupied by the discharge emissions from the system as a whole increases. Wüthrich (*83*) proposed a Poisson process model for the electrochemical discharges appearance in the current signal where the Poisson parameter λ, increases with the voltage. Each discharge released by the electrode contributes to the stability of the gas film by further heating up the electrode and creating favorable electric conditions to the continuity of the discharges process. Therefore, the series of discharges tend to maintain the stability of the gas film during this phenomenon. The last term, $\int \left\{-\delta \mathbf{i} \cdot \delta\left(\frac{\nabla U}{T}\right)\right\} dV$, in the excess entropy production expressed by Equation 3.71 and modeled by both the integral electrochemical model and the cold thermal emission theory is in agreement with this explanation.

The decrease of the gas film formation-time with the terminal voltage can be explained as follows. Coalescence of the electrochemically generated bubbles at the working electrode surface and evaporation of the electrolyte by local Joule heating are believed to be responsible for the gas film formation (*89*). Both contributions build the gas film faster with increasing the terminal voltage. A mathematical attempt to explain this trend is proposed by Allagui and Wüthrich (*88*). This result can be beneficiary for the various applications of the electrochemical discharge phenomenon such as nanoparticle synthesis, micro-machining by SACE technology and contact glow discharge electrolysis.

4.5. Conclusion

From the results of both nonequilibrium thermodynamics analysis presented in Chapter 3 and statistical estimation of stability indices of the gas film of this Chapter, the dynamics of the electrochemical discharge phenomenon are much clearer at this stage. One can adapt these results for its various technological applications such as SACE micro-machining of non-conductive materials, for example. The main conclusions to be retained from this part are the following:

1. The gas film formation-time is in the order of the millisecond and decreases with high voltages and temperatures, because of the enhanced mass transfer and bubble evolution at the electrode.
2. The gas film life-time, which is an index of stability of the phenomenon, is at least one order of magnitude higher than the gas film formation-time.
3. The gas film life-time increases with the applied terminal voltage and the bulk temperature.

On the other hand, the destabilization of the process or the breaking of the gas film is not observed macroscopically as it occurs in the range of each 10 to 50 ms. This suggests that fast and local perturbations, probably related to the emission and dissipation of electrical discharges from the electrode, might be behind the alternating behavior of the electrochemical process. This is to say that there is probably a critical value related to the gas film system itself, for example a certain degree of ionization, which makes the gaseous envelope not conductive enough and therefore the process ceases until the next turn.

So far, the last known application of the cathodic discharge phenomenon is the manufacture of nano-sized materials and the only reported work is by Lal et al. (*9*). This application is not well-understood and the main questions the second part of this thesis will focus on are:

1. Under which conditions are the nanoparticles synthesized?
2. What are the parameters to monitor during the synthesis procedure?
3. What are the parameters which control the obtained nano-sized materials? and
4. What is(are) the mechanism(s) behind the manufacturing process?

Prior to tackling these questions, an introduction to the importance of the nanoscopic engineering field that has seen so much development and research activity is the subject of Chapter 5. Some properties of nanoparticles and their applications are reviewed along with some of the most relevant synthesis techniques related or comparable to this work, i.e from the fields of electrochemistry and discharge physics.

Part II.

Synthesis of Nanoparticles

Chapter 5

Properties, Applications and Synthesis Methods

> *Nature uses only the longest threads to weave her patterns, so that each small piece of her fabric reveals the organization of the entire tapestry.*
>
> *(Richard Feynman)*

In 1959, the Nobel prize Laureate in Physics Richard Feynman gave his famous talk on top-down nanoscience and nanotechnology entitled: *There is plenty of room at the bottom* (*90*). In his lecture, Feynman talked about miniaturizing the technology we use by, in his words, *writing* and *reading small*, manufacturing *microcomputers*, *molecular machines* and *molecular doctors*. Nowadays, both academic and industrial interests for fundamental and applied nanoscale science and their applications are rapidly growing because of the nanoparticles size-dependent optical, mechanical, catalytic, magnetic and electronic properties. In the nanometer size scale, matter exhibits specific properties that can significantly differ from those of the bulk counterpart. Numerous technological applications are possible by extracting and combining these properties into functional systems. Therefore, nanoscience and nanotechnology are considered to be the pioneers of modern physics of the 21^{st}

century. Some of the commonly known properties of nano-materials and their applications, as well as some selected fabrication techniques, are reviewed in this Chapter.

5.1. Properties and Applications

The properties of particles in the nanometer size range are different from those of the correspondent bulk versions. Generally, nanoparticles properties depend on the size, the shape, the chemical composition, the medium in which they are dispersed, the dispersion state as well as their surface characteristics. Selected works on some of the most impressive properties of nano-materials are reviewed and discussed in what follows. A list of applications used in academia and industry are also outlined.

5.1.1. Properties

One of the reasons why nanoparticles cannot be treated as tiny elements of the bulk material is, from the electronic viewpoint, that the structure is changed from the continuous electronic bands to discrete or quantized electronic levels (*91*–*93*). This is explained by the presence of the conduction band in a bulk metal which is absent if we go down to the nano-scale material, and instead there are discrete states at the band edge. Downsizing from bulk material to small clusters is analogous to replacing a continuous density of state by a set of discrete energy levels. Starting from a certain critical size, the distance separating two small clusters will be in the order of magnitude of the wavelengths of the electrons leading to the quantum size effect (*92*).

An example is to analyze the quantum heat capacity of small clusters as was given by Kubo et al. (*92*) and based on Fermi liquid theory. Assume the average spacing between two successive levels of energy to be:

$$\delta_E \approx \frac{E_F}{N} \tag{5.1}$$

where E_F is the Fermi energy and N the number of valence electrons in a particle of finite size. If the particle is constituted of say 10^4 atoms, then δ_E will be of the order of 10^{-4} eV. The usual Fermi energy is of the order of a few electronvolts, which suggests from this simple example that δ_E of a few 10^{-4} eV corresponds to thermal energy of a few degrees Kelvin. At this temperature, one should expect alteration in some of the thermodynamic properties of the particle. For example, the quantum heat capacity of small particles at low thermal energy i.e. $k_BT \ll \delta_E$ can be expressed as (*92*):

$$C_p \approx k_B \left(\frac{k_BT}{\delta_E}\right)^{n+1} \tag{5.2}$$

while the specific heat of bulk material can be evaluated by (*92*):

$$C_b \approx k_B \left(\frac{k_BT}{\delta_E}\right) \tag{5.3}$$

with n an element from the set $\{0, 1, 2, 4\}$ (*91–93*). From Equations 5.2 and 5.3, it is clear that the heat capacity of small particles is $(k_BT/\delta_E)^n$ times less that the bulk material. Experimental measurements of the heat capacity of 10 to 26 Å average size of Pt particles co-sputtered with SiO_2 matrix at temperatures ranging from 1 to 12 K have been reported by Stewart (*94*). The author showed the size effect of Pt particles on their measured heat capacity which is in good agreement with the theory proposed by Kubo et al. (*92*).

Another example concerns the catalytic properties of nano-sized materials. Catalytic reactions, which are generally surface chemical reactions, are logically correlated to the high surface energy of nanoparticles. Indeed, when the size of

Table 5.1.: Variation of the proportion of surface atoms with the size of cluster.

# of cubes	Edge / cm	Surface / cm^2	% atoms on surface
1	1	6	10^{-5}
10^3	0.1	60	10^{-4}
10^{18}	10^{-6}	6×10^6	11
6.4×10^{19}	2.5×10^{-7}	2.4×10^7	44
10^{21}	10^{-7}	6×10^7	88

particles is reduced to the nanometer scale, the number of atoms at the surface or grain boundaries of the crystalline regions is comparable to the number of atoms that constitutes the crystalline lattice itself. For example, a nanoparticle of 10 nm diameter has approximately 10% of atoms on the surface, compared to very close to 100% when the diameter goes down to 1 nm. A simple calculation, originally shown by Ostwald, is illustrated in Table 5.1 starting from a cube of 1 cm^3 volume which has been successively divided into tiny cubes (*95*). For the case of 1000 cubes of 1 mm edge each, they will have a total surface of 60 cm^2, with just 6×10^{-5} cm^2 at the outside surface of the cube. However, 10^{18} cubes of 10 nm edge each will have the same volume as the later, but with some 0.66×10^6 cm^2 at the outside surface, which is 110 million times larger.

It is clear that nano-sized materials are much more suitable for catalytic purposes that the bulk material. One of the most impressive changes in properties induced by a decrease in particle size is the catalytic characteristic of gold nanoparticles. While the gold at bulk state is considered as a weak chemisorber, and consequently as a weak catalyst, Haruta et al. (*96*, *97*) have shown that the adsorption properties and reactivities of gold can be changed through the control of its size. Gold catalytic performances depend also on the degree of dispersion, shape and supported metal oxides. Gold supported on titanium oxide with optimum particle size of 2 to 3 nm has shown its most remarkable catalytic property, for example, in the combustion of carbon monoxide, the oxidation of amines and partial oxidation of hydrocarbons (*96*, *97*).

From the viewpoint of general thermodynamics, the melting temperature of nanoparticles, as an example, also strongly depends on the particle size. Buffat and Borel (*98*) studied the size effect on the melting point of gold particles having diameters down to 2 nm. They showed that T_m of 2 nm clusters of gold goes down to 600 K whereas 1100 K was measured for gold at 5 nm size, knowing that the bulk gold melting temperature is 1600 K. However, it has been found recently that tin clusters composed of tens of atoms stay solid above the melting point of the bulk material. In their wok, Shvartsburg and Jarrold (*99*) explained this phenomeon with what they called the hypothesis of *the heavy reconstruction geometry* of nanoclusters. In brief, the authors suggested that the geometric structure of tiny particles is totally different from the one which forms a bulk material.

Another well-known property of nano-sized materials is that, from the optical point of view, the presence of small metal particles in stained glass generates some very beautiful colors known from the times of the Egyptians and the Romans. When a particle is much smaller than the wavelength of light, coherent oscillation of the conduction band of electrons is induced by interaction with an external electromagnetic field. This resonance is called surface plasmon resonance. Mulvaney (*100*) have shown the *spectacular* size-dependence color of gold from the atomic to the mesoscopic scale. The changes gold–blue–purple–red of gold nanoparticles can be explained with Mie theory of light-scattering by a sphere. Ung et al. (*101*) have studied the optical properties of Au at SiO_2 particle films function of the silicon oxide shell thickness. From their result, the authors stated that it is possible to obtain heterogeneous nanoparticles with optical properties between those of the metallic gold and of the glass.

5.1.2. Applications

The various properties of nano-materials have multiple applications in academia and increasingly in industry. With the *Project on Emerging Nanotechnologies*[*], in the Washington press release of May 15, 2007 (*102*), it is claimed that the number of consumer products is almost 500 in the most advanced countries in the field. The Center has made available a list of 475 products related to nanotechnology from 20 countries from all around the world including clothing, cosmetics, cleaning products, jewelry, toys and games, food and beverages, electronics and computers, batteries, etc. Two year later, on August 25, 2009, the *Project* counted over 1000 nano-based consumer products (*103*) from 24 countries.

The histogram illustrated in Figure 5.1 has been last updated on February 09, 2010, and shows the number of products related to nanotechnology according to their country of origin. It can be seen that at the top of the list is the United States with 540 available products in the market, which constitutes over 50% of the global market. It is then followed by Asian countries which all together manufacture and commercialize some 271 products, while the European countries generate a bit more than 150 products. Canada, however, is noticeably behind with only 16 consumer products mainly related to clothing and cosmetics.

In the other hand, in the *Roadmap Report on Nanoparticles* published by the European Commission in 2005, Pérez et al. (*105*) said: "*Existing and potential applications*

---

[*] The Project on Emerging Nanotechnologies is an initiative launched by the Woodrow Wilson International Center for Scholars and The Pew Charitable Trusts in 2005.

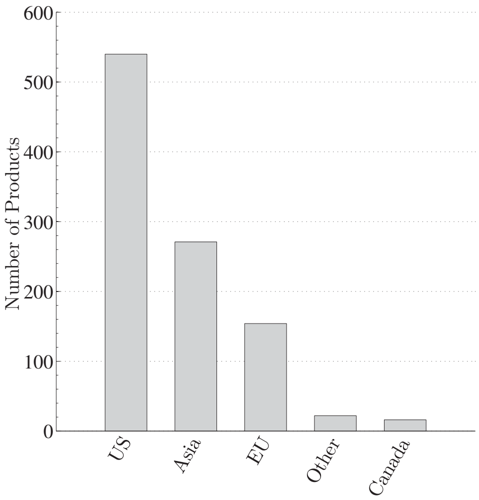

Figure 5.1.: Nanotechnology-related products by country of origin as of February 09, 2010 (*104*).

involving nanoparticles are almost endless". Some selected applications of nanoparticles are summarized in Table 5.2 (*105*, *106*) which are sorted by categories and sub-categories in the fields of energy & power, biomedical, material & engineering and electronics. Some other applications in healthcare, consumer goods, environmental and food industry are also included. Therefore, there are multiple synthesis techniques of nano-materials under intensive elaboration and some of them are analyzed and discussed in the next Section.

Table 5.2.: Some selected nanoparticles applications, adapted from Pérez et al. (*105*) and Nagarajan (*106*).

Category	**Application**	**Method**
Energy	Dye-sensitized solar cells	Increase of cells efficiency via the optical properties of TiO_2, ZnO and Au nanoparticles
	Hydrogen storage	Enhancement of hydrogen storage process by heterogenous metallic nanoparticles
	Fuel cell	Improvement of electrical and barrier properties of electrodes by carbon nanotubes and metal nanoparticles
Biomedical	Bone growth	Enhancement of bioactivity by hydroxyapatite ceramics
	Sunscreens	Enhancement of speed and effectiveness of skin protection by ZnO and TiO_2 nanoparticles
	Antibacterial wound dressings	Enhancement of bio-protection by Ag nanoparticles

	Bio-labeling and bio-detection	Increase the sensitivity and selectivity by Ag and Au nanoparticles
	Pharmaceutical	Enhancement of the efficiency of cancer diagnostics and drug delivery by magnetic nanoparticles
Material	Polymers	Reinforcement and lowering the loadings by organoclays and oxides of metal nanoparticles
	Pigments	Increase the protective properties and chemical stability of water-borne primers and coatings by Ag, Mg, Zn and Pb nanoparticles
Electronics	Data storage	Increase of data storage density by CoPt and FePt nanoparticles
	Electronic circuits	Thinner layers and more reliable electric path due to the point-to-point contacts of Ag, Cu and Al nanoparticles
	Ferro-fluids	Increase the efficiency of magnetic storage by the superparamagnetic property of Fe, FeCo and Fe_3O_4 nano-dispersions

5.2. Nanoparticle Synthesis Techniques

From an adequate survey of the recent extensive literature in nanoscience and nanotechnology, many of the various methods reported for the preparation of metal nanoparticles are applicable to a number of metals across the periodic table of elements. Different chemical, electrochemical and physical methods have been developed and used in order to obtain uniformly distributed ultra-fine particles. These strategies can be generally categorized in two main categories: the so-called *top-down* methods where the bulk material is dispersed into tiny clusters and the *bottom-up* techniques where nano-materials are prepared from the atomic or molecular precursors. Some other synthesis methods may belong to both categories in the same time. An emphasis on the low-current electrochemical methods by mean of two or three-electrode configurations are reviewed. The application of radiative chemistry and electric discharges to nanoscience are also presented as they both involve high energies, similar to the case of the electrochemical discharge phenomenon. Other techniques are presented but in less detailed focus.

5.2.1. Electrochemical Methods

Reetz and Helbig (*107*) proposed a simple electrochemical method to obtain fine colloidal particles of certain transition metals i.e. Pd and Ni nanoclusters in acqueous solutions. For example, Pd particles of 4.8 nm average diameter were synthesized in a two-electrode cell constituted of a 2×5 cm^2 palladium foil as the anode and a platinum foil of the same dimensions as the cathode. The Pd sheet is anodically dissolved with the application of electric current which forms intermediate metal cations. These ions will be reduced at the Pt cathode with the formation of adatoms giving colloidal Pd clusters stabilized by the additional tetraalkylammonium salts to the solution. The experiments are conducted in two-electrode configuration without any potentiostatic control or reference electrode. Reetz and Helbig (*107*) showed that the particle size can be controlled via the applied current density in the electrolysis cell. For example, Pd clusters of mean size diameter of 4.8 nm were synthesized with 0.1 mA/cm^2, whereas particles as small as 1.4 nm were obtained by applying 5 mA/cm^2 to the electrolytic cell.

By using two sacrificial anodes and one inert Pt cathode, and following the same electrolysis procedure described above, Reetz et al. (*108*) were able to synthesize bimetallic clusters such as Ni/Pd, Fe/Co and Fe/Ni with 3 nm average diameter. With precise control of the current density delivered by the dual power supply to the electrolysis cell, the composition of the hybrid nanoclusters can be controlled. For example, for the couple Ni/Pd, when applying a current density $|i_{Ni/Pt}|$=5 mA/cm^2 between the Ni anode and the Pt cathode and $|i_{Pd/Pt}|$=30 mA/cm^2 between the Pd anode and the Pt cathode, a ratio of 20:80 was obtained for Ni-Pd bimetallic clusters. In another configuration where both current densities are equal, $|i_{Ni/Pt}| = |i_{Pd/Pt}|$= 20 mA/cm^2, the measured ratio by elemental analysis was found to be 24:76. These compositions might be attributed to the difference of the reduction potentials of the metals Ni and Pd according to the authors (*108*).

The review of Reetz et al. (*109*) added additional valuable results about this two-electrode electrochemical method where it is shown that the solvent polarity plays an important effect in the size control of the particles. By varying the polarity of the medium via the ratio of acetonitrile (AN) over tetrahydrofuran (THF), the particle size of Pd is increased (*109*). For example, for a ratio AN:THF=0, it is found that the average Pd particle diameter is equal to 1.4 nm, while for a ratio AN:THF=0.5, the average diameter is 4.8 nm. Additionally, and with fixed medium polarity, the measured average size of the particles increases with the increase of the electrolysis duration which suggests that the growth process is a main parameter to be considered in the size-selectivity of this method (*109*). Also, it is remarked that there are two different behaviors of the system at low and high current densities. For example, by applying 2.16 mA/cm^2, the mean size of the obtained Pd nanoparticles linearly increases and were of less than 3 nm at 0.1 A.h, 3.5 nm at 1 A.h and a bit over 4 nm at 2.1 A.h. On the other hand, at a current density of 5.41 mA/cm^2, the average sizes of Pd nanoparticles did not change much and were found 2.82, 2.93, 2.93 and 2.72 nm at the charge flows of 0.1, 0.5, 1.7 and 2.1 A.h respectively.

Another experiment has been conducted by the group, wherein they were interested in evaluating the influence of the distance d between the Pd anode and the Pt cathode. For small values of d, their results suggest that there is no real monodispersity of the fabricated palladium nanoparticles. On the contrary, when separating the two electrodes by larger distance, almost monodisperse colloidal Pd clusters were obtained. Finally, the temperature is also an important variable to be considered as has been shown by Reetz et al. (*109*) via two tests for the particle size determination using TEM and SAXS. In short, at higher temperatures, the obtained colloidal particles are larger, which can be explained by various factors such as higher transport rates as well as lower overpotential η of the Pt cathode (*109*). Reetz et al. concluded their review by showing that the above mentioned parameters for size-selective $R_4N^+X^-$-stabilized[†] colloids are applicable to other transition metals such as Ni, for example.

Many others have been inspired by this electrochemical method, where Yu et al. (*110*) and Mohamed et al. (*111*) have reported the possible synthesis of gold nanorods. The experimental setup is similar to the one of Reetz et al. but the electrolytic solution has been modified to contain a cationic surfactant such as the hexadecyltrimethylammonium bromide (C_{16}TAB) and a rod-inducing cosurfactant such as the tetraoctylammonium bromide (TC_8AB). The two groups have reported that the addition of acetone is necessary to facilitate the cylindrical growth mech-

---

[†] $R = (n\text{-}C_4H_9), (n\text{-}C_8H_{17}), (n\text{-}C_{18}H_{37}), \ldots$ and $X^- = Br^-, Cl^-, \ldots$

anism for the obtention of the Au-surfactant-cosurfactant system. Furthermore, from Mohamed et al. (*111*), the average aspect ratio of the gold nanorods can be controlled by simple heating process where the length of the rods is observed to be decreasing by increasing the bulk temperature in which are fabricated the colloidal nanostructures.

The technique has been used and investigated with additional improvements (*112*, *113*). Yin et al. (*112*) proposed the addition of appropriate amounts of poly(N-vinylpyrrolidone) (PVP) which demonstrated two favorable effects for the synthesis of Ag nanoparticles. The polymer enhances the nucleation and formation process of the particles in the same time as reducing the electro-deposition of silver ions on the cathode surface. From Ma et al. (*113*), one can retain the conclusion that in addition to choice of appropriate surfactants and stabilizers, convective effects by using a rotating Pt cathode plays an important role in the monodispersity of the obtained nanoparticles. Indeed, the later generates centrifuge forces which will eject the manufactured particles to the bulk solution.

In a three-electrode cell, however, Tian et al. (*114*) also reported the successful electrodeposition of polycrystalline Pt nanoparticles of 750 nm average size on the surface of glassy carbon electrodes. This technique is fundamentally different from Reetz et al. method where here the cationic species are adsorbed and nucleate to form nanoparticles on the cathode surface. The solution is an aqueous mixture of 2 mM of K_2PtCl_6 and 0.5 M of H_2SO_4. The reported work of the group was aiming to manufacture single-crystal tetrahexahedral particles of high Miller's indices for catalytic purposes. The electrodeposited platinum particles of polyhedral shapes enclosed naturally by {111} and {100} facets were subject to electrochemical treatment by low frequency squared signals which generated smaller Pt particles enclosed by 24 facets such as the {730}, {210} and/or {520} surfaces (*114*). The electro-oxidation of formic acid and ethanol has been improved by almost four times in comparison with standard Pt polyhedral-shaped particles.

5.2.2. Radiolysis

In their communication to *Nature* in 1962 (*115*), Fujita et al. reported the homogeneous and instantaneous formation of colloidal gold nanoparticles in aqueous solution of chloroauric acid irradiated by a ^{60}Co γ-ray source. Experimentally, the authors have shown two interesting results when they irradiated two different 0.5 mM $HAuCl_4$ solutions with different radiation doses. Different aspects of the colloidal gold are obtained when the applied radiation dose rate is of 9.3×10^3 rad/min during 70 min or 9.8×10^3 rad/min during 10 min. This corresponds to total doses of 6.51×10^5 rad and 0.89×10^5 rad respectively. During the high radiation dose experiment, the Au particles were obtained with quasi-perfect circular shapes of 80 nm average diameter. However, from their SEM micrograph of the sample collected from the solution subject to lower radiation dose, micrometer-sized flat hexagons and quasi-triangular shapes were observed. Fujita et al. suggested that this difference in size and shape may be attributed to the difference in reaction rates of the products of radiolysis of water at different radiation doses, namely the H_2O_2 and $HO_2^{\cdot}$ or $H^{\cdot}$. Indeed, they concluded form a reference experiment, where the $HAuCl_4$ was reduced with the H_2O_2 without any radiative input giving even larger crystal shapes, that the hydrogen peroxide contributes mainly to the crystal growth rather than the nucleation. This is due to the competition between the two processes, more favorable to the former, because of the peroxide's slow reaction rate. On the other hand, even the bubbling of a 0.25 mM of $HAuCl_4$ with H_2 during 70 min did not produce a measurable quantity of gold nanoparticles, which suggests that it is actually the radicals $HO_2^{\cdot}$ or $H^{\cdot}$ which are the most active reducing agents to obtain nanoparticles by γ-radiolysis of aqueous solutions. Additional protective agents such as gelatin or polyvinyl alcohol contributed to the stability of the gold suspensions.

Marignier et al. extended the technique to synthesize non-noble metals such as Ni as well as two-metal alloys such as Cu−Pd (*116*). The group reported that despite the hydrated electron e^-_{aq} reducing strength which produce easily the zero-valent metal colloids, the difficulty with non-noble metals is that the reverse oxidations is much higher than with noble metals. Therefore, the successful use of radiolytic process for the synthesis of nanoculsters must include (*116*):

1. means of prevention of the back oxidation reactions,
2. means of inducing and favoring the aggregation process, as well as
3. chemical agents for the stabilization of the formed particles.

Following these recommendations Remita et al. (*117*) have successfully demonstrated the possibility to synthesize alloyed silver-palladium fine clusters with different proportions. The aqueous solutions contain metal salts mixture given the Ag^+ and Pd^{2+} ions in the mM range to which 2−propanol was added as a scavenger for the reactive radicals $OH^\cdot$ and $H^\cdot$. The alcohol presence is justified by selectively inducing the reactions with the $OH^\cdot$ and $H^\cdot$ radicals which will produce the strong reducing hydroxy-propyl as follows (*117*):

$$(CH_3)_2CHOH + OH^\cdot \longrightarrow (CH_3)_2^\cdot COH + H_2O \qquad (5.4)$$

$$(CH_3)_2CHOH + H^\cdot \longrightarrow (CH_3)_2^\cdot COH + H_2 \qquad (5.5)$$

The solution contains also 0.2 M of polyacrylic acid as a stabilizing surfactant. The pH of the solution was initially fixed to 2 but adjusted continuously during the γ-radiation experiments by adding sulphuric acid. As a result, the metal ions are being reduced by the hydrated electron e^-_{aq} and the hydroxy-propyl. From the unchanged optical absorption spectra of the colloidal solutions at the different doses ranging from 0 to 3.3 kGy[‡], Remita et al. concluded that the composition of the alloy Ag_x/Pd_{1-x} remains constant. In other words, no traces of core-shell configurations were detected. However, the control of the fraction *x* in the alloyed silver-palladium clusters is controllable via the initial conditions of the experimental solutions.

5.2.3. Electric Discharges

Successful manufacturing of monodispersed nanoparticles of a few nanometers is obtained with the use of electric discharges, which is a gas phase-based technique, versatile and quite economic. Sankaran et al. (*118*) synthesized blue luminescent Si nanoparticles of size ranging from 1 to 3 nm in diameter by applying micro-discharges in a SiH_4/Ar gas mixture. The experimental principle is based on a cathodically polarized tip facing an anode and generating micro-discharges within a plasma tube of high power densities per unit volume. The residence time of the discharges in the micro-reactor is as low as milli- to microseconds and they are operating in a plasma volume of the order of the microliter. To sustain the discharges between the electrodes, a potential difference of several hundreds of voltages is typically used with currents of some milliamperes. The power density of the electrical micro-dischargers is estimated to be a few kW/cm^3 which permits the facile decomposition of the used precursors to manufacture the required nanoparticles. Electron density in the plasma, temperature and quantity of injected metal precursor in the volume are the main parameters controlling the process.

The method based on electric discharges in liquids is also a promising technique. The setup is usually composed of a pulse generator able to function in spark and arc modes, a graphite electrode and another electrode made of the metal of interest. The two electrodes are separated by a fraction of a millimeter to maintain a stable

---

[‡] 1 Gy = 100 rad = 1 J/kg

activity of the discharges once they are initiated under some hundreds of volts (*118–120*). With different experimental conditions involving electrodes of Cu, W, and Zn, Burakov et al. (*119*) explained the mechanism of this technique as the dual pulverization/vaporization of the electrode material as well as the reduction by discharges of the metal precursors provides by their salts. The average fabrication efficiency of metal powder using the submerged pulsed discharges ranges from 1 to 40 mg/min (*119*), but this includes, of course, the whole range of sizes, from the micrometer down to the nanometer scale. The prepared nano-sized materials in suspension in the upper part of the solutions are found to be in the 3 to 7 nm interval for the tested materials.

5.2.4. Other Techniques

5.2.4.1. Sol-gel Approach

The sol-gel synthesis process of colloidal particles is based on hydrolysis followed by polymerization through condensation reactions (*121*, *122*). The polymerization chemistry via the cross-linking and branching of the inorganic polymeric chains leads to the formation of a three-dimensional blocks of nanoparticles. The typically used metal precursors are the alkoxides of the targeted material (*123*). From Kung and Ko (*122*), a simplified version of the hydrolysis and condensation reactions has been expressed as follows:

$$-\mathrm{M}-\mathrm{OR}+\mathrm{H_2O}\longrightarrow -\mathrm{M}-\mathrm{OH}+\mathrm{ROH}\quad:\quad\text{Hydrolysis}\qquad(5.6)$$

$$\left.\begin{array}{r}-\mathrm{M}-\mathrm{OH}+\mathrm{OR{-}M^-}\longrightarrow -\mathrm{M}-\mathrm{O}-\mathrm{M}-+\mathrm{ROH}\\ -\mathrm{M}-\mathrm{OH}+\mathrm{HO{-}M^-}\longrightarrow -\mathrm{M}-\mathrm{O}-\mathrm{M}-+\mathrm{H_2O}\end{array}\right\}\quad:\quad\text{Condensation}\qquad(5.7)$$

Chen and He (*124*) successfully synthesized $NiFe_2O_4$ nanoparticles by adding different proportions of polyacrylic acid (PAA) to a mixture of 0.4 M $Ni(NO_3)_2$ to

0.8 M $Fe(NO_3)_3$. After heat treatment of the obtained brown viscous gel, 30 nm down to 7 nm diameter of $NiFe_2O_4$ particles were characterized where the size decreased proportionally with the increase of the molar ratio of PAA. Bharathi et al. (*125*) presented a versatile approach applicable to synthesize nanodispersions of noble metals in silicate sol, gels and films. For the case of gold for example, a low concentrated HCl solution was added to a molar ratio of 100 to 1 of EDAS to $HAuCl_4$ to initiate the hydrolysis and condensation processes. The mixture is then reduced by a few droplets of sodium tetrahydridoborate giving an uniform size distribution with and average diameter of 5 to 6 nm. The procedure is the same for other metals whereas the used precursors for the cases of platinum, palladium and silver are their correspondent chloride or nitrate salts, the H_2PtCl_6, $Pd(NO_3)_2$ and $AgNO_3$ respectively.

5.2.4.2. Salt Reduction

An example of the method of chemical reduction of salts for the synthesis of colloidal nanoparticles is the well-known Turkevich et al. method (*126*, *127*) for the preparation of suspended gold nanoparticles. The technique is standardized and is based on the chemical reduction of chloroauric acid $HAuCl_4$ and trisodium citrate. The colloidal gold nanoparticles are obtained by firstly boiling a solution of 100 ml of $HAuCl_4$ containing 50 mg of gold. While stirring the solution, 5 ml of 1% sodium citrate was added which react by changing gradually the color from yellowish to faint grayish-pink or grayish-blue tone until stabilizing on a deep wine-red color.

Hirai et al. (*128*) successfully manufactured colloidal dispersions of several kinds of transition metals i.e. rhodium, palladium and platinum, among others, by the reduction principle of their corresponding chloride salts in alcohols and ether solutions. The synthesis is under the stabilization function of organic polymers such as poly(vinyl alcohol), polyvinylpyrrolidone and poly(methyl vinyl ether).

The obtained particles are monodispersed with sizes ranging from of a few tens of nanometers to the nanometer scale. The overall reaction involves the oxidation of the used alcohol and the reduction of metal ions in the solutions. For example with rhodium, one has (*95*):

$$RhCl_3 + 3/2R_1R_2CHOH \longrightarrow Rh^0 + 3/2R_1R_2CO + 3HCl \tag{5.8}$$

5.2.4.3. Microemulsions

First attempts using microemulsions to synthesize nano-materials has been reported by Boutonnet et al. (*129*) back in 1982 with the synthesis of monodisperse Pt, Pb, Rh and Ir particles in the 3 to 5 nm range. Stable Pt and Pb colloids have been obtained by the authors, but the synthesis of Rh and Ir nanoparticles has been reported that it requires high reduction kinetics which destabilize the equilibrium of the microemulsions. The reduction of metal ions provided by their corresponding salts was via either hydrazine or hydrogen gas in organic solvents. The principle of microemulsions to manufacture nano-sized materials is based on producing thermodynamically stable nano-sized droplets in which selected chemical reactions are initiated (*130*). Microemulsions are composed of two immiscible liquids such as water-in-oil or oil-in-water stabilized with surfactants. The most commonly used technique is to introduce two reactants A and B in two identical microemulsions and then, by mixing them, the colliding droplets will generate a product C (*131*). This technique allow the fabrication of single-metal nanoparticles (*132*, *133*) as well as alloys (*134*–*137*) of sizes ranging from 1 to 50 nm.

5.2.4.4. Sonochemistry

Ultrasound irradiation of liquids generates cycles of expansion and compression waves where during the negative pressure, sound can generate acoustic cavitations if the wave overcomes the tensile strength of the liquid (*138–140*). In other words, under high intensity ultrasound, the collapsing of bubble in liquids and therefore the high transport rates of kinetic energy of collisions generate locally high temperatures and pressures, emulsifications and some unusual chemical effects (*140*). The over 5000 K temperature generated by the *hot spots* was determined from sonoluminescence spectra in water by Flint and Suslick (*141*). Putterman (*142*) reported even higher temperatures and suggested that the lifetime of the hot spots is in the range of nano to picoseconds. From this, the heat transfer rates might exceed the 10^{12} $K.s^{-1}$ (*139*). The chemical consequences of this high-energy chemical phenomenon have been reviewed and reported by Suslick et al. (*143*) and Suslick and Price (*140*) where several kinds of nano-sized materials can be obtained such as amorphous and colloidal metals (*144–147*) as well as biomaterials (*148*). The sonochemical modification or degradation of polymeric materials and polymer surfaces is also possible (*138*, *140*).

In their letter to *Nature*, Suslick et al. (*144*) reported that the irradiation of iron pentacarbonyl ($Fe(CO)_5$) by high-intensity ultrasound, i.e. by using a ultrasonic generator delivering 20 kHz frequency and 100 W/cm^2 power intensity, produces over 96% purity amorphous iron powder. The experiment have been conducted without any additional surfactant or trapping agent. However, from the ultrasound irradiation of a solution of $Fe(CO)_5$ in octanol ($CH_3(CH_2)_7OH$) in the presence of PVP, colloidal iron nanoparticles were successfully manufactured (*145*). 3 to 8 nm diameter Fe particles are trapped in the polymer matrix and still exhibit some amorphous character, from the TEM nanographs. In the presence of oleic acid ($CH_3(CH_2)_7CH{=}CH(CH_2)_7COOH)$), Suslick et al. (*145*) reported that the stabilization is more uniform than the PVP yielding to monodisperse particles but with slightly larger diameter i.e. 8 nm in average. No hysteresis is observed in the magnetization-demagnetization loops of the PVP trapped iron nanoparticles, which in addition to the unchanged behavior the magnetization M versus the corrected ratio M/T suggests that the sonochemically manufactured Fe particles are superparamagnetic (*145*).

The synthesis of other kinds of metals has been reported (*146*, *147*). In Hyeon et al. (*146*), the authors have shown the successful manufacture of nanoparticles of molybdenum carbide (Mo_2C) from the high-intensity sonification of molybdenum hexacarbonyl ($Mo(CO)_6$) with hexadecane ($C_{16}H_{34}$). The obtained porous powder exhibits catalytic behavior comparable to platinum toward the dehydrogenation of cyclohexane. Okitsu et al. (*147*) compared the influences of different trapping and agglomeration-protecting agents such as sodium dodecyl sulfate (SDS), PVP, etc. While in water the Pd nanoparticles are generally unstable and tend to agglomerate quite quickly, with the presence of the polymer PVP, it has been shown that the stability in extended to a few days. However, SDS for example, maintains the colloidal state of the nanoparticles for several months (*147*). The authors have also shown some relation between the initial concentration of the metal precursor $PdCl_2$ as well as the nature of the protective agent on the average size of the obtained Pd nanoparticles. By using a calorimetric method to determine the rate of formation of Pd particles, Okitsu et al. concluded that the reduction of Pd^{2+} to zero-valent Pd in water is assured by the H atoms. However, with the presence of SDS or PVP, these agents act as powerful reducing agents, by producing intermediate radicals by pyrolysis, in addition to their stabilization functionality.

5.3. Conclusion

In summary, by giving access to the wide range of functionalities and performances of nanometric structures, nanoscience and nanotechnology are revolutionizing how we understand and use materials for our daily usages. The field of nanoscience is already having important scientific and commercial impacts on a global scale, due to the dynamic research activity that it generated. The synthesis and assembly of nanoparticles are the core research directions of this interdisciplinary field which make it the leading theme in the nanoscience family tree through the broad range of existing synthesis methods, as some have been enumerated above. The new technique based on the cathodic electrochemical discharges in aqueous solutions is investigated in Chapters 6 and 7 by presenting, respectively, a general experimental procedure for successful manufacturing of nano-materials as well as its governing mechanisms.

Chapter 6

Experimental Procedure and Characterizations

> *We must trust to nothing but facts. These are presented to us by Nature, and cannot deceive. We ought, in every instance, to submit our reasoning to the test of experiment, and never to search for truth but by the natural road of experiment and observation.*
>
> ---
>
> *(Antoine Laurent Lavoisier)*

The synthesis route of nanoparticles using the cathodic electrochemical discharges in aqueous solutions has not yet been investigated in detail. A few works have been reported (*6*, *9*) but an explicit experimental procedure about the technique and its mechanism are not available. A sequential and comprehensive methodological usage of the electrochemical discharges for the synthesis of nano-sized materials, including the influence of the working conditions are presented in this Chapter. Nickel and nickel oxide-based nanoparticles are known for their various applications such as in magnetic recording media (*149*), electro-catalysis (*150–152*), fuel cells (*153*) and gas sensing devices (*154*, *155*) and are the main subject of this investigation.

Additionally, NiO are known for their high performances for electrochemical energy storage applications (*156–160*), and will be investigated in this regard in Chapter 8. Morphological, structural and electrochemical characterizations of the obtained particles are presented with a summarized version of the microscopic mechanistic description which will be treated in more details in Chapter 7.

6.1. Materials and Setup

6.1.1. Materials

- H_2SO_4, H_3PO_4, HNO_3, HCl, KOH, NaOH, CH_3CH_2OH (Et) and $(CH_3)_2CO$ (Ac) were purchased from Fisher Scientific. All chemicals and reagents are used as received and no further purification was performed.
- Polyvinylpyrrolidone of molecular weight 40000 g/mol (PVP40) is bought from Sigma-Aldrich.
- Carbon black Vulcan XC72 was given courtesy of Cabot.
- 0.5 mm diameter at 99.98% purity Ni rods and 5×5 cm^2 at 99.5% purity Ni plates are purchased from Alfa Aesar.
- Ag/AgCl/KCl (saturated) reference electrode and 0.5 mm diameter at 99.99% purity Pt wire counter electrode with glass-fritted tube are purchased from Pine Research Instrumentation.
- Graphite electrodes of a cross-section of 0.27 cm^2 are purchased from SPI Supplies.
- Carbon-coated copper grids and silicon wafers are from Electron Microscopy Sciences.

- Grade 5.0 ultra high purity (99.999%) compressed nitrogen and argon gases are from Praxair.

6.1.2. Setup

- The used setup to manufacture the nano-sized materials is a two-electrode electrochemical cell as illustrated in Figure 2.1(a). Typically, the anodic polarized plate is of much larger geometrical surface (4×5 cm^2) than the cathodic one (approximately 10 mm^2). The immersion depths of both electrodes into the 100 ml solution is controlled by placing the whole experimental arrangement on top of a lab jack and attaching the cathode to a holder which can move vertically.

- The used remotely controlled DC power supply is the ZUP60-3.5 model from TDK Lambda which delivers 0-60 V and 0-3.5 A.

- In some instances, the current timeseries data during the discharge regime are monitored and collected through an Agilent current probe model N2774A-50 MHz connected to an Agilent DSO 3102A-100 MHz digital storage oscilloscope.

6.1.3. Characterizations Procedure

The general chart of the characterization procedure of the manufactured nanoparticles is illustrated in Figure 6.1, in which:

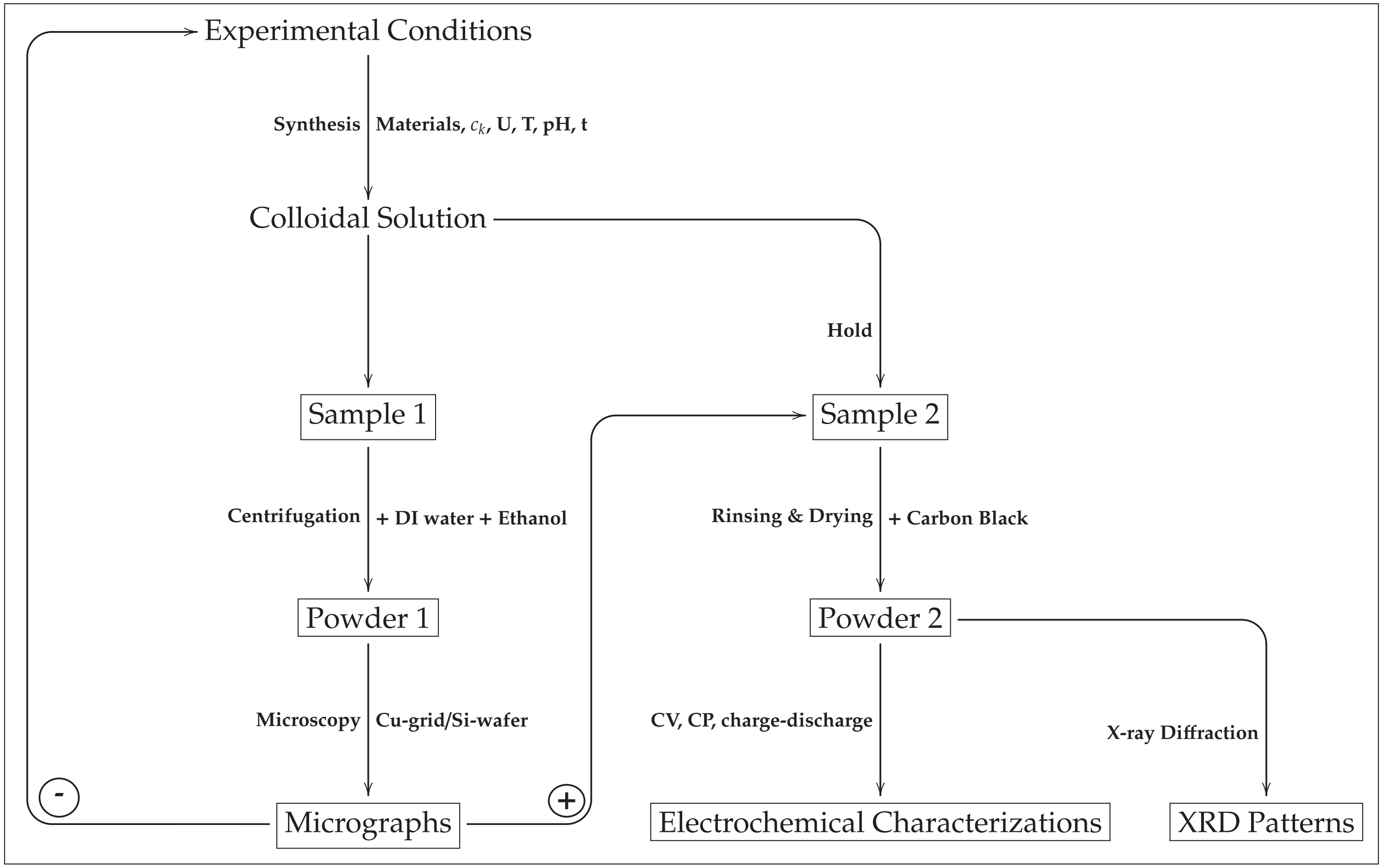

Figure 6.1.: Nanoparticles characterization chart.

- the ultra high resolution micrographs of nanoparticles are obtained with a JEOL JSM-7500F FESEM for scanning electron micrographs and a JEOL JEM-2100F FETEM for tunneling electron micrographs. Samples are prepared by depositing and drying the colloidal nanoparticles either onto a copper grid or a freshly cleaned silicon wafer.

- the powder X-ray diffraction patterns are measured in the θ-2θ geometry with a Philips X'Pert Pro Multipurpose X-ray diffractometer. Samples are prepared by *gluing* with Vaseline® a uniform flat layer of the tested powder on an approximatively 3 cm^2 portion of a glass slide for microscopes.

- the electrochemical measurements are recorded with an Amel Electrochemistry's potentiostat model 7050 versus the Ag/AgCl/KCl (saturated) reference electrode. The three-electrode setup is arranged in a standard multi-neck round-bottom flask under continuous bubbling of N_2 or Ar gases.

6.2. Preliminary Conditions

The electrochemical discharge phenomenon occurs when certain critical electric conditions are satisfied in a two-electrode setup. The starting point to describe and characterize this technique for the synthesis of nano-materials is to define the controllable variables to be monitored to reach an acceptable repeatability. As discussed in Section 3.2.2, the phenomenon is far from the thermodynamic equilibrium but naturally, not all possible combinations of external and internal constraints can be controlled and adjusted. Therefore, a few global and pertinent parameters are considered and studied in this work to manufacture nano-sized nickel materials, starting with the cell and its geometric design, the origin of the metal precursors and the stability of the products, and the minimum required electric conditions.

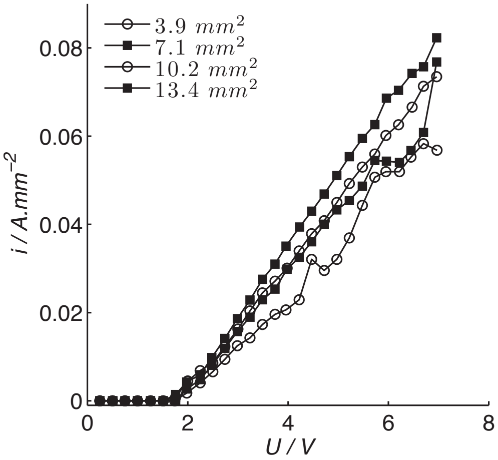

Figure 6.2.: Polarization curves of Ni cathode of four different surfaces immersed into NaOH 30% wt. aqueous solution.

6.2.1. Electrochemical Cell

The geometrical parameters of the electrochemical cell are investigated. The anode, a 5 × 5 cm^2 nickel plate, is partially immersed into an aqueous solution of NaOH 30% wt.* so that its surface with direct contact with the electrolyte is equal to 5 × 4 cm^2. A nickel rod of 0.5 mm diameter is screwed into the holder of a rotating disk electrode and placed at a distance of 3 cm from the anode. The whole arrangement is connected to a DC remotely controlled switching power supply ZUP60-3.5, and placed on top of a lab jack which allows the control of the immersion depth of the cathode into the electrolyte. The vertical reference is determined by switching on the power supply and slowly moving down the holder-cathode arrangement until some macroscopic bubbles at the surface of the electrolyte can be observed.

Four single 0 to 7 V scans acquired at 1 V/s scan rate corresponding to the four different immersion depths, 1, 2, 3 and 4 mm, of the cathode into the electrolyte are illustrated in Figure 6.2. The nickel rod surface in the legend of the plots does not take into consideration the surface tension effect. Starting from around 2 V,

---

*For better monitoring of the process a strong base is chosen in which the electrochemical discharges are easily visible.

corresponding to the water decomposition potential, Ohm's law is approximatively satisfied from the quasi-linearity of the curves. Figure 6.2 shows another particularity of the polarization curves where at very low values of the cathode surface, some deviations from the expected linear plot are recorded. This is clearly the case when the nickel rod is immersed just 1 mm into the electrolyte, which can be justified by the surface tension effect giving rise to approximately another 1 mm meniscus above the free surface of the solution. Above approximately 3 mm of immersion depth, the polarization curves of the nickel are perfectly linear. Thus, the the depth value of the electrode is an important geometric parameter to control during the electrochemical discharges.

6.2.2. Metal Precursors

The origin of metal precursors to be reduced during the discharge regime can be provided either by anodic dissolution or by dissolving salts of the targeted metal (*9*). For this work, the ionic entities present in the solution are provided by the dissolution of the metallic anode in contact with the aqueous solution which involves both electronic and ionic processes at the surfaces (*21–23*, *161*, *162*):

$$\mathrm{M^{z+}_{(aq)} + ze^- \longrightarrow M_{(s)}} \quad : \quad \text{Cathodic} \tag{6.1}$$

$$\mathrm{M_{(s)} \longrightarrow M^{z+}_{(aq)} + ze^-} \quad : \quad \text{Anodic} \tag{6.2}$$

The case of nickel dissolution in sulfuric acid solutions is discussed. Itagakia et al. (*163*) studied the dissolution mechanisms by mean of electrochemical quartz crystal microbalance. From the polarization curve of electrodeposited nickel, at low values of the anodic voltage, a first and second active dissolution regions were identified and producing mainly $\mathrm{Ni^{2+}}$ ions. At the transpassive dissolution region identified at higher anodic voltages, also $\mathrm{Ni^{2+}}$ ions were obtained but at lower rates.

Between the second active and the transpassive dissolution regions, a plateau in the current-voltage polarization curve characterizes the nickel passivity due to the formation of NiO (*164*, *165*) which ranges from 0.2 to around 1 V. Adapting Bockris et al.'s mechanism (*166*) for the dissolution of iron, the following mechanism has been proposed for the two active dissolution regions of nickel (*163*):

$$\mathrm{Ni} + \mathrm{OH}^- \leftrightharpoons \mathrm{NiOH}_{ads} + e^- \tag{6.3}$$

$$\mathrm{NiOH}_{ads} \longrightarrow \mathrm{NiOH}^+ + e^- \tag{6.4}$$

$$\mathrm{NiOH}^+ \longrightarrow \mathrm{Ni}^{2+} + \mathrm{OH}^- \tag{6.5}$$

At higher anodic voltages, passing the passivation region, the mechanism of nickel dissolution is similar and was proposed by Sato and Okamoto as (*167*, *168*):

$$\mathrm{Ni} + \mathrm{H_2O} \leftrightharpoons \mathrm{NiOH}_{ads} + \mathrm{H}^+ + e^- \tag{6.6}$$

$$\mathrm{NiOH}_{ads} \longrightarrow \mathrm{NiOH}^+ + e^- \tag{6.7}$$

For the synthesis of nanoparticles of nickel or its oxides/hydroxides by electrochemical discharges, the metal precursors should be stable for the continuous production of nano-materials by the process. In addition, the obtained particles are also expected to be stable in the solution.

6.2.3. Pourbaix Diagram

The Pourbaix diagram, also called the potential-pH diagram, provides a graphical illustration, for a given metal, of the domains of stability in aqueous solution of the metal ions, oxides and hydroxides etc. The Nernst equation allows to compute the lines in the Pourbaix diagram for the equilibrium reactions of the three following types:

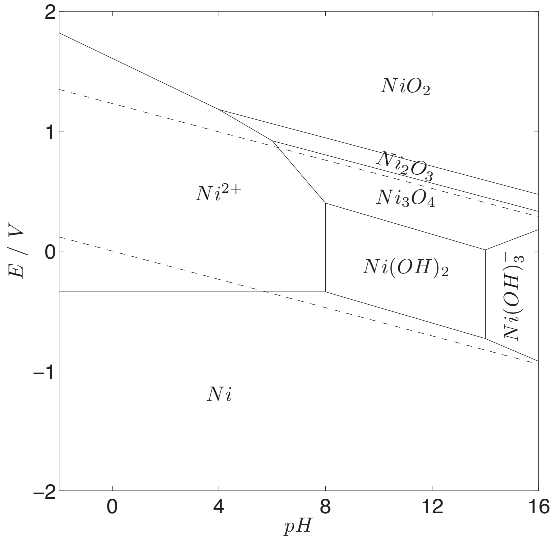

Figure 6.3.: Potential-pH diagram of 10^{-4} M of Ni at 25 °C.

- electrochemical reactions of pure charge transfer (horizontal lines),
- pure acid-base reactions (vertical lines),
- electrochemical reactions involving both charge and H^+ or OH^- transfers (other lines).

Figure 6.3 illustrates a simplified version of the Pourbaix diagram of 10^{-4} M of nickel at 25 °C where not all possible reactions are taken into account. Table 6.1 gives the values of the $E = a \times pH + b$ lines on the diagram (*169*, *170*). For example, for the first reaction in Table 6.1 of reduction of water in acidic solution written as:

$$H^+ + 2e^- \rightleftharpoons H_2 \tag{6.8}$$

Nernst equation writes:

$$\begin{aligned} E_{H^+/H_2} &= E^\circ_{H^+/H_2} + \frac{RT}{zF} \ln\left(\frac{c^2_{H^+}}{P_{H_2}}\right) \\ &= 0 + \frac{0.059}{2} \times 2 \times (-pH) = -0.059 \text{ pH} \end{aligned} \tag{6.9}$$

Table 6.1.: Reactions and equilibrium lines E = a × pH + b of the potential-pH diagram of 10^{-4} M of Ni at 25 °C represented in Figure 6.3.

pH	**a**	**b**	Reaction
-2 ··· 16	-0.059	0	$2\,H^+ + 2\,e^- \rightleftharpoons H_2$
-2 ··· 16	-0.059	1.23	$H_2O \rightleftharpoons 1/2\,O_2 + 2\,H^+ + 2\,e^-$
-2 ··· 8	0	-0.34	$Ni^{2+} + 2e^- \rightarrow Ni$
8	∞	-0.34··· 0.4	$Ni^{2+} + 2\,OH^- \rightleftharpoons Ni(OH)_2$
14	∞	-0.73··· 0.01	$Ni(OH)_2 + OH^- \rightleftharpoons Ni(OH)_3^-$
8 ··· 14	-0.065	0.18	$Ni + 2\,OH^- \rightleftharpoons Ni(OH)_2 + 2\,e^-$
8 ··· 14	-0.065	0.92	$3\,Ni(OH)_2 \rightleftharpoons Ni_3O_4 + 2\,H_2O + 2\,H^+ + 2\,e^-$
6 ··· 8	-0.26	2.48	$3\,Ni^{2+} + 4\,OH^- \rightleftharpoons Ni_3O_4 + 4\,H^+ + 2\,e^-$
4 ··· 6	-0.13	1.7	$2\,Ni^{2+} + 3\,H_2O \rightleftharpoons Ni_2O_3 + 6\,H^+ + 2\,e^-$
-2 ··· 4	-0.106	1.606	$Ni^{2+} + 2\,H_2O \rightleftharpoons NiO_2 + 4\,H^+ + 2\,e^-$
6 ··· 16	-0.059	1.274	$2\,Ni_3O_4 + OH^- \rightleftharpoons 3\,Ni_2O_3 + H^+ + 2\,e^-$
4 ··· 16	-0.059	1.416	$2\,NiO + OH^- \rightleftharpoons Ni_2O_3 + H^+ + 2\,e^-$
14 ··· 16	-0.095	0.6	$Ni + 3\,OH^- \rightleftharpoons Ni(OH)_3^- + 2\,e^-$
14 ··· 16	0.085	-1.18	$3\,Ni(OH)_3^- \rightleftharpoons Ni_3O_4 + OH^- + 4\,H_2O$

where $E°(H^+/H_2)$, c_{H^+} and P_{H_2} are the standard reduction potential of hydrogen, the concentration of H^+ and the partial pressure of gaseous H_2 respectively. In the same way, one can write from the second reaction in Table 6.1, corresponding to the oxidation of water:

$$\begin{aligned} E_{O_2/H_2O} &= E^{\circ}_{O_2/H_2O} + \frac{RT}{zF}\ln\left(\frac{\left(P_{O_2}\right)^{0.5} c^2_{H^+}}{c_{H_2O}}\right) \\ &= 1.23 + \frac{0.059}{2} \times 2 \times (-\mathrm{pH}) = 1.23 - 0.059\ \mathrm{pH} \end{aligned} \tag{6.10}$$

The same procedure follows for the rest of the equations. Reading the Pourbaix diagram shown in Figure 6.3 can be illustrated with the following example. The region between the two dashed lines represent the domain of water stability. Suppose the nickel metal dissolving in acidic solution of pH 0, the reaction Ni + 2 e^- → Ni^{2+} is more active than the evolution reaction $2H^+ + 2e^- \rightarrow H_2$ where the former reaction can drive the latter one. In other words, the Ni will displace the H_2 from the solution and the corrosion will take place via H^+ reduction. Pourbaix diagram allows, for a given metal, to predict at which region in the potential-pH space to operate the electrochemical discharges for the synthesis of nanoparticles.

6.2.4. Electric Conditions

To define the required electrical conditions for the fabrication of nickel nanoparticles, firstly, triangular voltage scans are performed in the solution. The steady state current-voltage characteristics, plotted in Figure 6.4, indicates the minimum cell terminal voltage to obtain the colloidal nanoparticles by electrochemical discharges[†]. The terminal voltage has to be larger than the critical voltage $U_C \approx 18$ V starting from which the gas film is getting formed, otherwise a continuous deposition of dendritic structures, as illustrated in Figure 6.5, are obtained. Practically, the voltage should be greater than $U_D \approx 25$ V because the system is in a metastable state just after the breakdown of region C-D due to the intense bubbles formation and instability of the

---

[†] The plot is performed in a solution composed of 2 M of H_2SO_4 + 1 M of ethanol + PVP40 in the range 0 to 50 V. More details about this composition will be given hereafter.

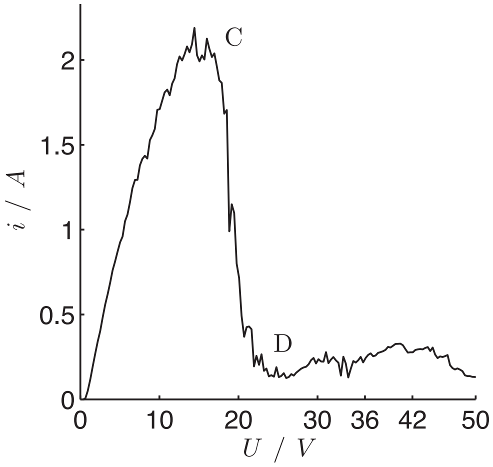

Figure 6.4.: Mean i-U characteristics during electrochemical discharges in 2 M H_2SO_4 + 0.5 M Et + 2.5 mg/ml of PVP40. Cathode and anode are both made of Ni and are of geometric surfaces 5 mm^2 and 20 cm^2 respectively.

Figure 6.5.: Dendritic structures: Ni working electrode covered by solid crystal deposition formed in aqueous solution of 2 M H_2SO_4 at 10 V.

gas film (*21*–*23*, *88*). However, large values of the terminal voltage are not suitable either, as it may cause the rapid melting of electrode due to the high thermal energy generated by the high current densities.

6.3. Synthesis and Characterization of Nanoparticles

6.3.1. Synthesis Conditions

- The primary solution for the synthesis of colloidal dispersion of nickel nanoparticles is an aqueous solution of 2 M of H_2SO_4 and 0.5 M of ethanol as $OH^{\cdot}$ radical scavenger (*171*). More details about the scavenging necessity of the hydroxide radical will be given in Chapter 7, but in short, ethanol is used to prevent the back oxidation reaction of reduced metal ions. The choice of the acidic environment for the manufacturing process is justified from the reading of potential-pH diagram of nickel where the Ni_2^+ ions generated by anodic dissolution will be the precursors for the reduction to nanomaterials. 250 mg of PVP40 as stabilizing agent are added *in situ* to each 100 ml of the solution. Alkaline solutions of KOH will be used at other instances to synthesize colloids by electrochemical discharges.
- Both cathode and anode are made of high purity nickel. The cathode is of 99.98 % purity and the anode is of 99.5 %.
- The experiment duration is usually set between 1 and 5 hours.
- The minimum and maximum applied terminal voltages are set to 30 and 60 V respectively.
- The bulk temperature at 3 cm from the cathode is approximatively 55 °C.
- The setup is operating at atmospheric pressure.

6.3.2. Characterizations

Morphological characterizations and size distribution analysis of the as-synthesized nickel nanoparticles by electrochemical discharges at cell terminal voltage of 36

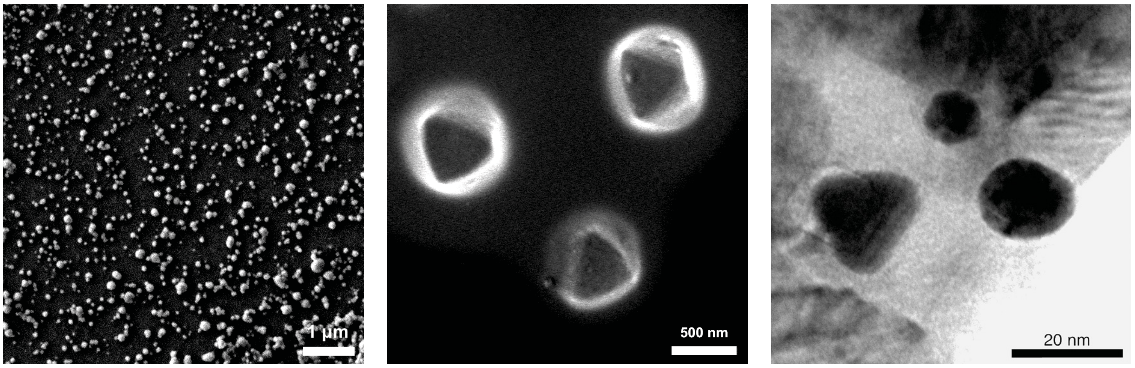

(a) Typical SEM micrograph.

(b) SEM micrograph of larger particles.

(c) TEM micrograph of ultra-fine nanoparticles.

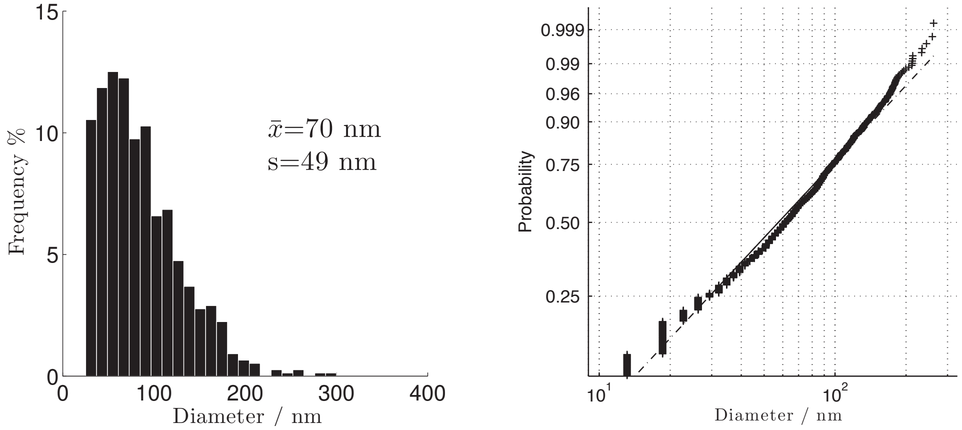

(d) Frequency histogram of size distribution.

(e) Weibull probability plot of size distribution.

Figure 6.6.: Electron micrographs (6.6(a)-6.6(c)) and size distribution analysis (6.6(d)-6.6(e)) of nickel nanoparticles synthesized in 2 M H_2SO_4 + 0.5 M Et + 2.5 mg/ml of PVP40 discharged at 36 V during 3 hours.

V during 3 hours are shown in Figure 6.6. Figure 6.6(a) shows a representative scanning electron micrograph of the obtained particles after being centrifuged, washed with DI water and ethanol and deposited on a copper grid. The size of the dispersed particles is within the interval with upper and lower limits of approximatively 300 and 25 nm respectively. However, some larger octahedral particles as illustrated in Figure 6.6(b) are also observed in some areas of the same imaging sample. At higher magnifications, from the TEM micrograph of Figure 6.6(c), it is shown that with the electrochemical discharges it is also possible to obtain

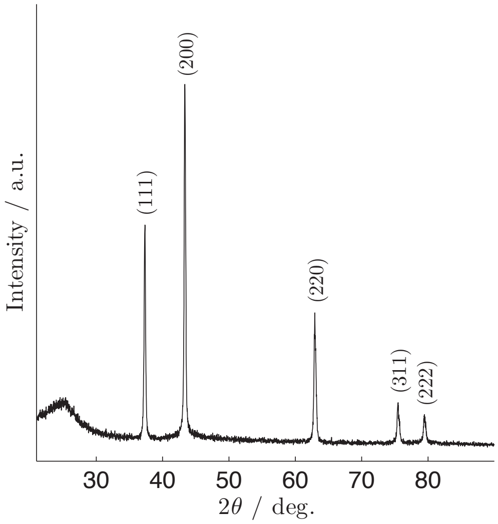

Figure 6.7.: Powder X-ray diffraction patterns of carbon black coated-NiO nanoparticles synthesized in 2 M H_2SO_4 + 0.5 M Et + 2.5 mg/ml of PVP40 discharged at 36 V during 3 hours.

ultra-fine particles of size smaller than 20 nm. The frequency bar plot of the size distribution of the synthesized nanoparticles illustrated in Figure 6.6 is shown in Figure 6.6(d), where the sample mean $\bar{x}$ is found to be 70 nm and the sample variance s is estimated at 49 nm. The particle size distribution is adequately described by the Weibull distribution (*172–174*) as shown in Figure 6.6(e). This is indicated by the good linearity of the plot of the probabilities versus their correspondent particles size diameter in logarithmic scale. From the probability plot, 75 % of the particles are of sizes less than or equal to 100 nm.

For the analysis of phase purity and crystallinity, Figure 6.7 shows the powder X-ray diffraction pattern of the as-prepared powder of carbon-coated nanoparticles fabricated at 36 V. The extraction of the materials out of the solution follows the same method as described by Baranova et al. (*175*). In short, this step consists in adding a predefined quantity of carbon black Vulcan XC72 to the colloidal solution and then stir it for several hours. The collected powder is rinsed and dried for powder X-ray diffraction analysis (see Figure 6.1). The pattern shows a small hump for 2θ less than 30° because of the amorphous structure of the carbon powder added to the solution of nanoparticles during the extraction step. The pattern is characterized by sharp well-defined peaks with strong intensity indicating the high crystallinity of the obtained powder. The typical peaks of the PDF-4+ (ICDD) 04-011-8441 file corresponding to the crystal *hkl* planes (111), (200), (220), (311) and (222) of cubic NiO (bunsenite, NaCl type structure) are perfectly indexed. Nickel oxide is the stable state of the metal at the operating pH as shown previously in Pourbaix diagram of Figure 6.3. The crystallite size is estimated by using Scherrer's formula:

$$d = \frac{K\lambda}{\beta \cos\theta} \tag{6.11}$$

The shape factor K is taken 0.89 and the X-ray wavelength is 1.5405 Å. The estimation uses the full width at half-maximum β of the most intense peak corresponding to the plane (200) and the size of the crystallite is found to be 35 nm

The electrochemical activity of the obtained powder of nickel oxide is analyzed by cyclic voltammetry. Note that the tested products during the electrochemical measurements consist of the nanoparticles of nickel oxide only, without the addition of carbon black. The experimental setup includes a Pt rod counter electrode inserted in a fritted glass tube and an Ag/AgCl/KCl (saturated) reference electrode. In a voltammetric arrangement, the potential between the working and reference electrodes is controlled while no current flows through the reference electrode. The voltage scan rate is 15 mV/s between 0 and 0.6 V vs Ag/AgCl electrode. The voltammogram, in a 1 M KOH solution being continuously deaerated with argon, of the as-synthesized nickel oxide nanoparticles at 36 V and deposited on a freshly polished graphite electrode is shown in Figure 6.8. The y-axis shows the current density per unit mass of the synthesized nanoparticles which are weighted with a quartz crystal microbalance. Such precision is needed because the yield of the process is in the milligram per hour. The voltammogram shows the two characteristic

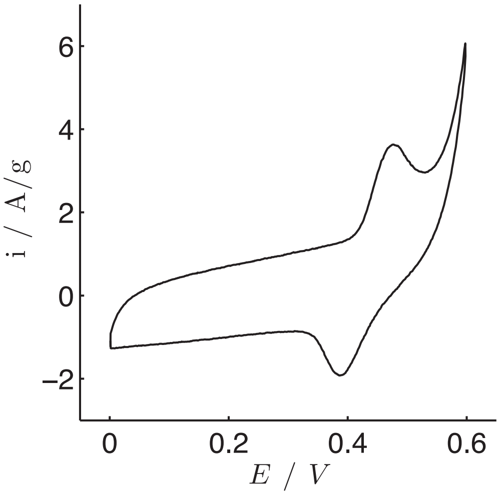

Figure 6.8.: Cyclic voltammogram at 15 mV/s vs. Ag/AgCl of NiO nanoparticles synthesized in 2 M H_2SO_4 + 0.5 M Et + 2.5 mg/ml of PVP40 discharged at 36 V during 3 hours.

peaks of anodic oxidation of NiO to NiOOH and cathodic reduction of the reverse process, which by using the hydroxyl ion from the alkaline solution as the active ion can be written as (*159*, *176*, *177*):

$$\mathrm{NiO} + \mathrm{OH}^- \rightleftharpoons \mathrm{NiOOH} + \mathrm{e}^- \tag{6.12}$$

The shapes and intensities of the peaks did not change significantly after some 8 to 10 cycles indicating the stability of the synthesized nickel oxide particles.

6.3.2.1. Effect of Voltage

Three voltages are chosen from the current-voltage characteristics of Figure 6.4 and based on the difference in the time parameters of their current timeseries signals. Figure 6.9 illustrates the current signals recorded in an aqueous solution of 2 M H_2SO_4 + 0.5 M Et + 2.5 mg/ml of PVP40 at the three terminal voltages: 30, 36 and 42 V. The signal at 42 V is clearly very intense with its dense discharge activity when compared to the other two voltages, while the one at 30 V shows intermittent

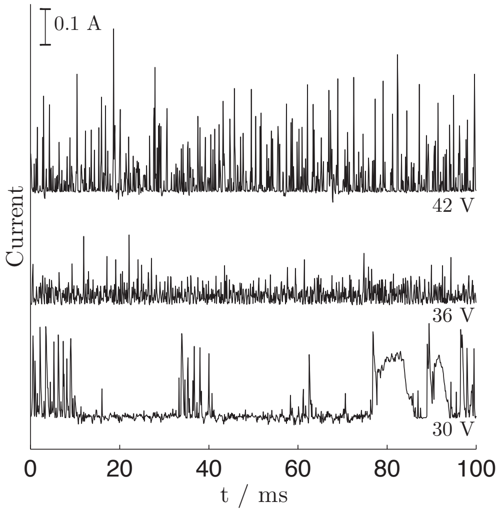

Figure 6.9.: Current timseries at 30, 36 and 42 V during electrochemical discharges in 2 M H_2SO_4 + 0.5 M Et + 2.5 mg/ml of PVP40. Cathode and anode are both made of Ni and are of geometric surfaces 5 mm^2 and 20 cm^2 respectively.

packets of high intensity with pretty long *zero-current* flow. Note that this is in close agreement with the results obtained in Chapters 3 and 4 about the gas film stability and dynamics, respectively.

A comparison of the effect of cell terminal voltage on the obtained particles is illustrated by the micrographs of Figure 6.10 together with Figure 6.6(a). SEM image of NiO nanoparticles synthesized at 30 V is illustrated by Figure 6.10(a) which shows that the size of nanoparticles ranges from 500 nm down to a few tens of nanometers. Spherical particles are obtained at 42 V and are shown in Figure 6.10(b). They are organized in a sort of chain-like network. The high local temperature due to the high discharge activity at this voltage is probably responsible of the sintering of the particles (*178*). The size distribution statistics of the obtained particles are summarized in Table 6.2 which shows the sample mean and sample variance of the size distribution of NiO nanoparticles. At 36 V, these statistics are the lowest with comparison with the other two terminal voltages, 30 and 42 V.

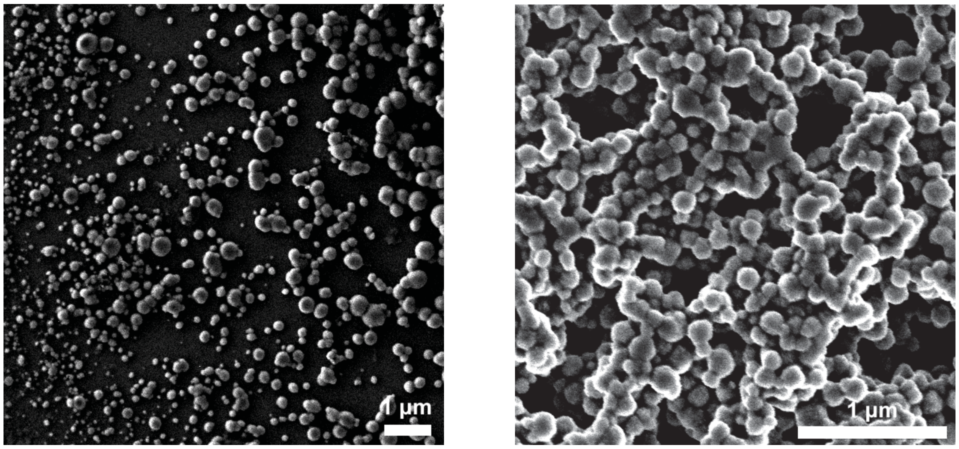

(a) 30 V (b) 42 V

Figure 6.10.: SEM micrographs of NiO nanoparticles synthesized in 2 M H_2SO_4 + 0.5 M Et + 2.5 mg/ml of PVP40 discharged at 30 V (6.10(a)) and 42 V (6.10(b)) during 3 hours.

Table 6.2.: Sample mean and sample variance of NiO nanoparticles synthesized by electrochemical discharges in 2 M H_2SO_4 + 0.5 M Et + 2.5 mg/ml of PVP40 during 3 hours at 30, 36 and 42 V.

Voltage / V	30	36	42
$\bar{x}$ / nm	91	70	107
s / nm	97	49	53

Powder XRD patterns of carbon coated-NiO fabricated at the voltages 30, 36 and 42 V are shown in Figure 6.11. The quantitative analysis of the (200) peak intensity shows a relative variation by factors 0.85 and 4.7, for the samples synthesized at 30 and 42 V respectively, with respect to the intensity computed from samples manufactured at 36 V. The added quantity of the carbon black to the colloidal solutions of nanoparticles is the same for all experiments.

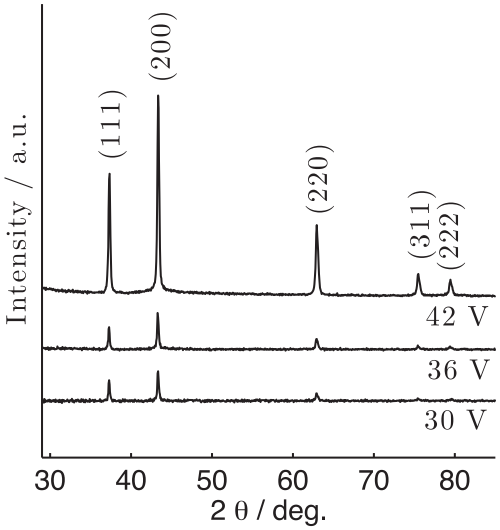

Figure 6.11.: Powder X-ray diffraction patterns of carbon black coated-NiO nanoparticles synthesized in 2 M H_2SO_4 + 0.5 M Et + 2.5 mg/ml of PVP40 discharged at 30, 36 and 42 V during 3 hours.

Two conclusions are drawn from the comparison of the effect of voltage. The first is that low current intensity discharges generate smaller sizes of nanoparticles because of the low concentration of building blocks. From Figure 6.9, an average discharge has a current intensity of 0.14, 0.07 and 0.13 A at 30, 36 and 42 V respectively. Particle size at these respective voltages are 91, 70 and 107 nm. However, one may ask why the particles synthesized at 42 V are larger than those of 30 V? This can be explained by the fact that at the higher voltage, the process generates more reducing species, that will be discussed in Chapter 7 in detail, and thus higher concentration of building units. Although the intensity of the discharges at 30 V are comparable to those of 42 V, they are more stable and with higher frequency of appearance in the later case because the gas film is more stable. This yields to higher nucleation and growth rates which are responsible for this trend.

The second conclusion is that when the discharge activity is globally more stable from the frequency and magnitude point of view, as it is the case of the experiments at 36 and 42 V, the overall process tends to homogenize the sizes of the obtained nanoparticles. This can be seen in their respective sample standard deviations of 49 and 53 nm in Table 6.2. On the contrary, when the operating conditions generate discharges of higher intermittence and variability, like it is the case of the experiment at 30 V, the size of the obtained products are more disperse with $s = 97$ nm. Indeed, in this later case, the discharge regime alternates back and forth with the conventional electrolysis more frequently because the gas film is less stable. This induces a relatively higher convective environment for the clusters in the vicinity of the cathode an thus a forced nucleation process. Additionally, one can remark from the current signal at 30 V that some of the discharges are of low intensities and others are of high intensities, which in connection with the fist conclusion, should give small and large particles in the same time, and thus a broad size distribution of the particles.

6.3.2.2. Effect of Experiment Duration

Under the same electrochemical conditions and sample preparation and characterization but by changing the experiment duration, it is remarked that there is a change in the quantity of the obtained material, as shown in Figure 6.12 (compare with figure 6.6(a)) where the experiment duration is set to 1 hour and to 5 hours. The micrograph in Figure 6.12(a) shows more dispersed nano-sized nickel oxides on the copper grid, whereas the SEM image in Figure 6.12(b) shows higher concentration of the synthesized products when compared to the synthesis during 3 hours. Table 6.3 shows the sample mean and sample variance of NiO nanoparticles for the various experiment durations at a fixed terminal voltage of 36 V. The average size of particles increases with the manufacturing time suggesting that the coalescence and growth are key parameters during the synthesis of colloids by electrochemical discharges. More details will be given in Section 7.2. The corresponding powder XRD patterns are shown in Figure 6.13 where there is as well a relative change of the (200) peak

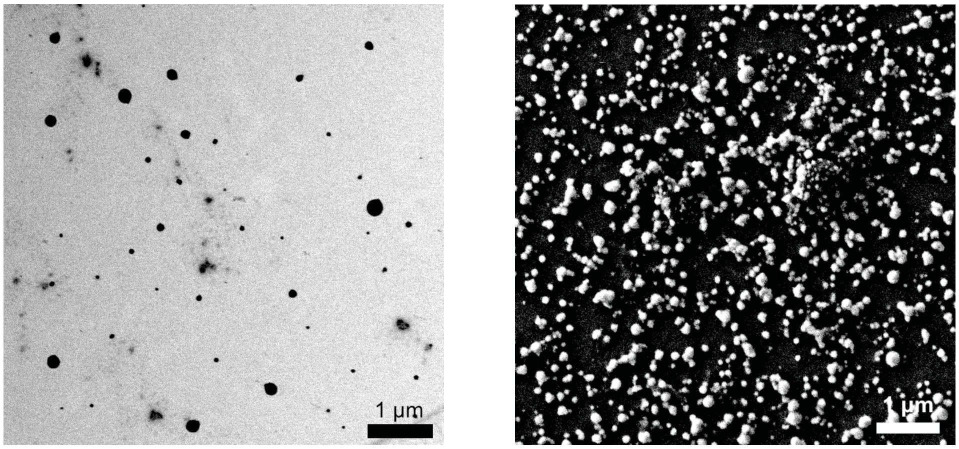

(a) 1 hour. (b) 5 hours.

Figure 6.12.: SEM micrographs of NiO nanoparticles synthesized in 2 M H_2SO_4 + 0.5 M Et + 2.5 mg/ml of PVP40 discharged at 36 V during 1 hour (6.12(a)) and 5 hours (6.12(b)).

Table 6.3.: Sample mean and sample variance of NiO nanoparticles synthesized by electrochemical discharges in 2 M H_2SO_4 + 0.5 M Et + 2.5 mg/ml of PVP40 at 36 V during 1, 3 and 5 hours.

Time / hours	1	3	5
$\bar{x}$ / nm	60	70	79
s / nm	63	50	65

intensity by factors 0.2 and 1.35 for the samples synthesized of NiO during 1 and 5 hours respectively, with respect to the one of sample manufactured during 3 hours.

6.4. Conclusion

The successful synthesis of nickel oxide nanoparticles in acidic medium using the electrochemical discharges is presented where the main steps are as follows:

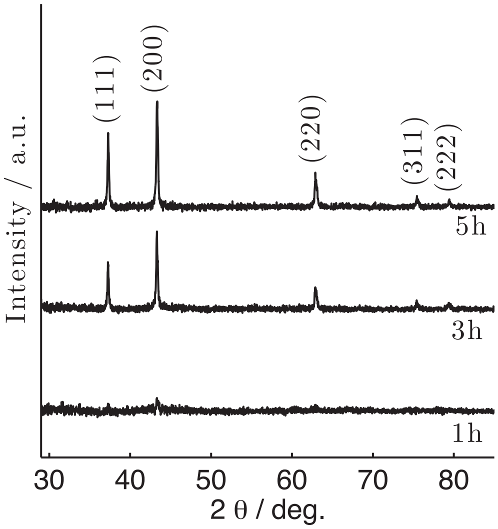

Figure 6.13.: Powder X-ray diffraction patterns of carbon black coated-NiO nanoparticles synthesized in 2 M H_2SO_4 + 0.5 M Et + 2.5 mg/ml of PVP40 discharged at 36 V during 1, 3 and 5 hours.

1. prepare an electrochemical solution based on the stability of the metal phases from its Pourbaix diagram: metal ions to be reduced during the process and the subsequent products shall be stable in solution,
2. add stabilizing agents to the solution,
3. add $OH^{\cdot}$ scavengers to prevent the back reactions of oxidation,
4. apply a voltage larger than the mid-point voltage, estimated from the *i*-*U* characteristics, and taking into account the stability of the gas film,
5. adjust the penetration depth of the cathode into the solution to globally control the current intensity,
6. make the right compromise between the targeted size distribution and the quantity when choosing the duration of the manufacturing process.

The stability of the gas film and discharge activity, from the frequency and intensity viewpoints, are the direct parameters to be controlled to obtain specific sizes and quantities of nanoparticles by the electrochemical discharges. Stabilizing agents and experiment duration are yet important reaction variables to adjust to fully explore the potential of this promising technique. The mechanisms behind the fabrication of nano-materials by electrochemical discharges in aqueous solutions are treated in detail in Chapter 7. The application of the obtained nickel oxide materials are tested for energy storage purposes in Chapter 8.

Chapter 7

Mechanism and Yield

> *He who loves practice without theory is like the sailor who boards ship without a rudder and compass and never knows where he may cast.*
>
> *(Leonardo da Vinci)*

Results of the nanoparticles synthesis by electrochemical discharges presented in Chapter 6 and other supporting evidences to be presented hereafter suggest two possible reaction mechanisms for this technique. Each of the two interfaces surrounding the gas film during the discharge regime, i.e. *i)* the gas-liquid interface and *ii)* the electrode-gas interface, are believed to play some roles in the early stages of manufacturing process of the fine particles. The self-assemblance, from the zero-valent atomic units to the aggregation by coalescence of the elemental nuclei, completes the proposed mechanisms for this synthesis route. Supersaturation and nucleation theory as well as crystal growth followed by the different used techniques for the stabilization of colloidal clusters are also included in the discussion.

7.1. Formation of Zero-valent Metal Atoms

Two mechanisms are proposed for the synthesis of nanoparticles by electrochemical discharges. The same concepts can be readily extended for the comprehension of the other applications of the phenomenon such as micro-machining, wastewater treatment and surface engineering. Firstly, a mechanism based on the metal ion reduction down to the zero-valent state is discussed. Inspired from radiation chemistry, this model considers the reactions at the gas film-electrolyte interface. The possible reactions of reduction and oxidation by the hydrated electron and $H^{\cdot}$ and $OH^{\cdot}$ radicals are treated in detail. The second mechanism considers the physics of the electrode sputtering process. The disintegration or erosion of the electrode is a surface effect which generates clusters by complex cascade collisions of the ionic species at the upper atom planes of the electrode.

7.1.1. Gas-liquid Interface

With the formation of the gaseous envelope covering the cathode, the discharges from the electrode towards the electrolyte are somehow similar to radiative beams generated from a particle beam at the top of a solution. A similar assumption was already proposed by Hickling and Ingram (*35*) for the anodic GDE mechanism, where the charges were carried out by the superoxide ion H_2O^+. The same assumption by Sengupta and Singh (*19*) was extended to the cathodic GDE. Firstly, a brief reminder of the principles of this division of high energy chemistry is introduced, emphasizing the hydrated electron roles and reactions. As the $H^{\cdot}$ and $OH^{\cdot}$ radicals are respectively strong reducing and oxidizing agents of cations in aqueous solutions, they will be given special attention as far as it concerns their chemistry. Naturally, this will be followed by the possible reactions to produce the zero-valent particles in the gas-liquid interface.

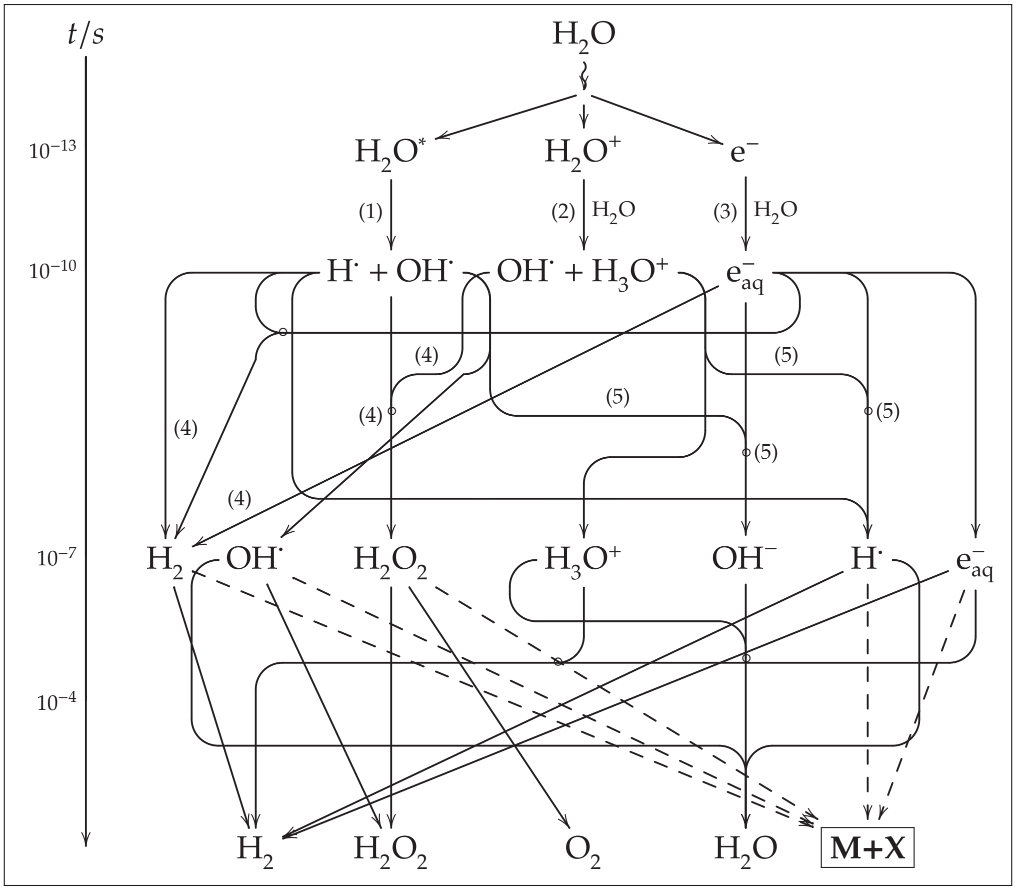

$^{(1)}$ Dissociation; $^{(2)}$ Ion-molecule; $^{(3)}$ Solvation; $^{(4)}$ Dimerization; $^{(5)}$ Recombination.

Figure 7.1.: Water irradiation mechanism, adapted from Buxton (*171*).

The current state of knowledge of radiation chemistry of aqueous solutions containing the ions M is summarized in its general reactional mechanism in Figure 7.1 (*171*). It also includes the time scale at which the various reactions are happening. The first reaction with this process gives birth to the ionized state of the water molecule, H_2O^+ and one electron e^-, in addition to the electronically excited state, H_2O^*:

$$H_2O \rightsquigarrow H_2O^+, e^-, H_2O^* \tag{7.1}$$

The ion-molecule reaction of H_2O^+ with water molecule gives both $OH^\cdot$ radical and the hydronium cation H_3O^+ such as:

$$H_2O^+ + H_2O \longrightarrow OH^\cdot + H_3O^+ \tag{7.2}$$

while the dissociation of the H_2O^* gives the $H^\cdot$ and $OH^\cdot$ radicals, with the possible reaction giving H_2 and oxygen radical, as follows:

$$H_2O^* \longrightarrow H^\cdot + OH^\cdot,\ H_2 + O\cdot \tag{7.3}$$

On the other hand, within this series of ultra fast reactions occurring in the times span of the electronic transition*, e^- will undergo a solvation reaction. With water as the solvent, the solvation or more specifically the hydration reaction is written as:

$$e^- + nH_2O \longrightarrow e^-_{aq} \tag{7.4}$$

The solvated electron was for the first time observed by transient optical absorption measurements by Hart and Boag (*179*) in 1962. It is a transient chemical species where the electron e^- is surrounded by solvent molecules. This trapping process happens once the electron reaches its thermal equilibrium with the liquid, which is achieved in less than a picosecond (see Figure 7.1). A schematic representation of the solvated electron e^-_s is illustrated in Figure 7.2, where the size of the lengths of the arrows represent the characteristics of the vector electron-dipolar molecule interaction. Hart and Boag have successfully produced the solvated electrons by means of pulse radiolysis of aqueous solutions. Other ways to produce the e^-_s are known, such as chemical and electrochemical methods as well as the photolysis using flash lamps or lasers (*171*, *180*).

---

*In the order of picoseconds.

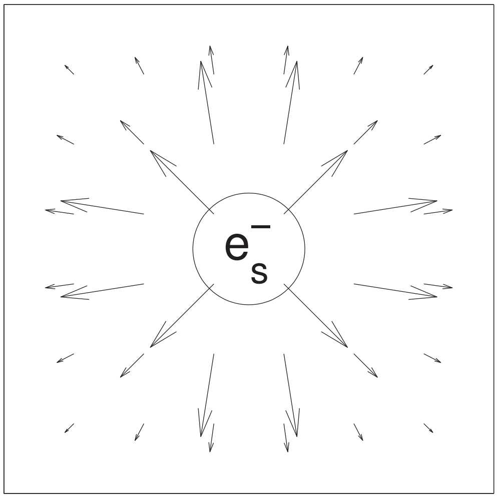

Figure 7.2.: Schematic representation of hydrated electron trapped by the surrounding solvent molecules represented by outward arrows.

In a second step, depending on their kinetic energies, the products $H^{\cdot}$, $OH^{\cdot}$, H_3O^+ and e^-_{aq} can react together by dimerization and recombination reactions as well as off themselves. Table 7.1 lists the possible reactions at this step where the ones involving the cations M are shown in Figure 7.1 with dashed lines. From results of water radiolysis at 0.23 eV/nm, products from radiated water molecule, up to the 10^{-7} s time period, can be described by the following overall reaction (*171*):

$$H_2O \rightsquigarrow 0.28\ e^-_{aq},\ 0.063\ H^{\cdot},\ 0.28\ OH^{\cdot},\ 0.047\ H_2,\ 0.073\ H_2O_2,\ 0.28\ H_3O^+ \qquad (7.5)$$

where the numbers represent the radiation chemical yield in 10^{-6} mol/J, reported generally in terms of the *G*-values[†]. One can remark that the main chemical yields in reactions 7.5 are the hydrated e^-_{aq}, the hydroxyl radical $OH^{\cdot}$ and the hydronium cation H_3O^+, where the reactions give about 2.7 molecule/100 eV of each of these products. These transient reactions are then followed in time by several other

---

[†] $G(X)$ is known as the number of molecules of product X formed per 100 eV energy absorbed. Note that commonly the unit molecule/100 eV is used where 1 mol.J^{-1} equals to $9.6490 \cdot 10^6$ molecule/100 eV.

Table 7.1.: Dimerization and recombination reactions durring water irradiation, adapted from Buxton (*171*).

Chemical reaction	**Reaction rate constant k**[†]
$e^{-}_{aq} + e^{-}_{aq} \longrightarrow H_2 + 2\,OH^{-}$	0.54
$e^{-}_{aq} + OH^{\cdot} \longrightarrow OH^{-}$	3.0
$e^{-}_{aq} + H_3O^{+} \longrightarrow H^{\cdot} + H_2O$	2.3
$e^{-}_{aq} + H^{\cdot} \longrightarrow H_2 + OH^{-}$	2.5
$H^{\cdot} + H^{\cdot} \longrightarrow H_2$	1.3
$OH^{\cdot} + OH^{\cdot} \longrightarrow H_2O_2$	0.53
$OH^{\cdot} + H^{\cdot} \longrightarrow H_2O$	3.2
$H_3O^{+} + OH^{-} \longrightarrow 2\,H_2O$	14.3

[†] k × ∽ 10^{10} $M^{-1}.s^{-1}$ (zero-order reactions).

reactions due to the diffusion of the products toward the bulk. Several molecular and secondary radical products are obtained such as H_2, H_2O_2, O_2, H_2O and stable products of reactions with metallic ions M present in the aqueous solution (*171*).

7.1.1.1. Mechanism

Despite its short life-time, the solvated electron in aqueous solutions or the hydrated electron is considered as a strong reducing element (*37*, *171*, *179–181*). Indeed, it has a standard reduction potential with respect to the standard hydrogen electrode (SHE) of $E°(H_2O/e^{-}_{aq}) = -2.87$ V. The $H^{\cdot}$ atom is also a powerful reductant species in acidic solution with E°($H^+/H^\cdot$) = -2.31 V, and is formed following the reaction 7.6 (*171*):

$$e^-_{aq} + H^+ \longrightarrow H^\cdot \tag{7.6}$$

Therefore, the first proposed mechanism to synthesize the metal particles is based on the high efficiency of reduction of metal ions M with valency *z*+ by the hydrated electron e^-_{aq} and follows the scheme of Reactions 7.7-7.9 (*21–23*, *116*, *182*):

$$\begin{aligned} H_2O + e^- &\rightsquigarrow e^-_{aq}, H^\cdot, OH^\cdot, H_2, H_2O_2, H_3O^+ && (7.7)\\ e^-_{aq} + M^{z+} &\longrightarrow M^{(z-1)+} && (7.8)\\ &\cdots \\ e^-_{aq} + M^+ &\longrightarrow M^0 && (7.9) \end{aligned}$$

Similarly, with the $H^\cdot$ atoms, generated from the reaction of e^-_{aq} and H^+, the reduction of metal ions can be written:

$$\begin{aligned} H_2O + e^- &\rightsquigarrow e^-_{aq}, H^\cdot, OH^\cdot, H_2, H_2O_2, H_3O^+ && (7.10)\\ H^\cdot + M^{z+} &\longrightarrow M^{(z-1)+} + H^+ && (7.11)\\ &\cdots \\ H^\cdot + M^+ &\longrightarrow M^0 + H^+ && (7.12) \end{aligned}$$

These Reactions are then followed by:

$$n\,M^0 \longrightarrow M_2 \longrightarrow \cdots\ M_n\ \cdots \longrightarrow M_{agg} \tag{7.13}$$

where the zero-valent atoms M^0 progressively grow to form M_2, M_3, …, until reaching a stable M_n nucleus. They actually represent the nucleation phase of the colloids. Nucleation will be then followed by coalescence to form the nano-sized aggregates. More details are given in Section 7.2.

On the other hand, the $OH^{\cdot}$ radical is the strongest oxidizing agent among the species generated from water radiolysis, with $E°(OH^{\cdot}/OH^{-}) = 1.90$ V in neutral solution and $E°(H^{+},OH^{\cdot}/H_2O) = 2.72$ V in acidic solution. Both e^{-}_{aq} and $H^{\cdot}$ atom are able to reduce metal ions quite easily to the zero-state of valence but in the same time the $OH^{\cdot}$ radicals are able to oxidize them back to a higher level of oxidation as has been demonstrated by Kelm et al. (*183*). Reactions 7.8-7.9 and 7.11-7.12, where the metal precursor is reduced to M^0, which will nucleate to a nucleus and then aggregate progressively to the final nano-sized state, can be interrupted and reversed by oxidation at any stage, such that (*181*):

$$OH^{\cdot} + M^{z+} \longrightarrow M^{(z+1)+} + OH^{-} \tag{7.14}$$

This reaction can be prevented by adding scavenger species of $OH^{\cdot}$ radicals, such as primary or secondary alcohols or formate anions (*171*). The formed radicals are strong reducing species and take over the reduction reaction instead of the oxidation reaction by the $OH^{\cdot}$ radical. This reaction has been prevented in the experimental section of Chapter 6 by adding ethanol to the solution which generates the α-hydroxyethyl radical able to reduce the metal ions following the reactions:

$$CH_3CH_2OH + OH^{\cdot} \text{ or } H^{\cdot} \longrightarrow CH_3C^{\cdot}HOH + H_2O \text{ or } H_2 \tag{7.15}$$

$$CH_3C^{\cdot}HOH + M^{z+} \longrightarrow M^{(z-1)+} + CH_3COH + H^{+} \tag{7.16}$$

The yield of nanoparticles manufactured by the electrochemical discharges can be adjusted to a certain extent by the control of the added quantities of scavengers of oxidizing species generated by the process.

7.1.1.2. Arguments

Goodman et al. (*184*) have measured the yield of the hydrated electrons in glow discharge electrolysis. The study was based on the measurement of the yield of chloride using the scavenging property of monochloroacetic acid for the hydrated electron:

$$\mathrm{ClCH_2COOH} + \mathrm{e^-_{aq}} \longrightarrow \mathrm{Cl^-} + {}^{\cdot}\,\mathrm{CH_2COOH} \tag{7.17}$$

They have found a primary yield $G(\mathrm{e_{aq^-}})$ of 3.3 mol/mol when varying the concentration of the chloroacetic acid in 0.5 M H_2SO_4 aqueous solution. Acetone is also a very strong scavenger of the hydrated electron with reaction rate of 0.63 $\times$ 10^{10} $M^{-1}.s^{-1}$ (*185, 186*). Acetone reacts with the hydrated electrons to form the 2-propanol radical which does not react with metal ions (*183*). Indeed, three hours of cathodic discharging in 2 M H_2SO_4 + 1 M of acetone + PVP gave very low quantities of metallic particles when compared to the experiments presented in Section 6.3. A solution with 3 M of acetone decreased even further the expected quantity of materials so that it made the collection of the powder very sensitive and difficult. The current timeseries signal was monitored and was found to be very comparable to the discharges containing ethanol instead of acetone.

Further evidence is to compare the chemical characterizations of nano-materials synthesized by electrochemical discharges under the two following experimental conditions. The first is what has been investigated previously in Section 6.3 i.e. 2 M H_2SO_4 + 0.5 M Et. + PVP40 where both electrodes made of nickel, while in the second experiment, electrochemical discharges are conducted with a platinum cathode and a nickel anode in the same electrolytic solution and at 36 V during 3 hours. Figures 6.6 , 6.7 and 6.8 have shown the morphological, chemical and electrochemical characteristics of NiO nano-materials. On the other hand, Figure 7.3 shows the different characterization results of the obtained products when the

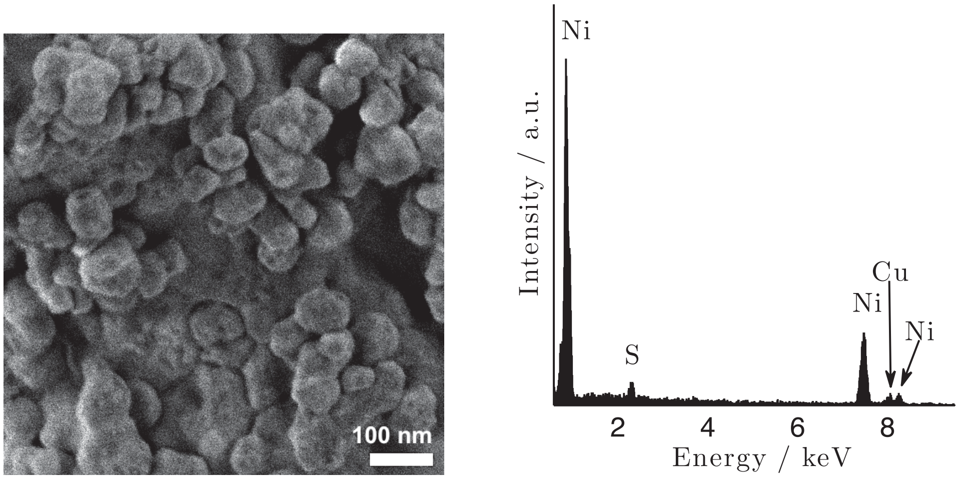

(a) SEM micrograph.

(b) EDX spectrum.

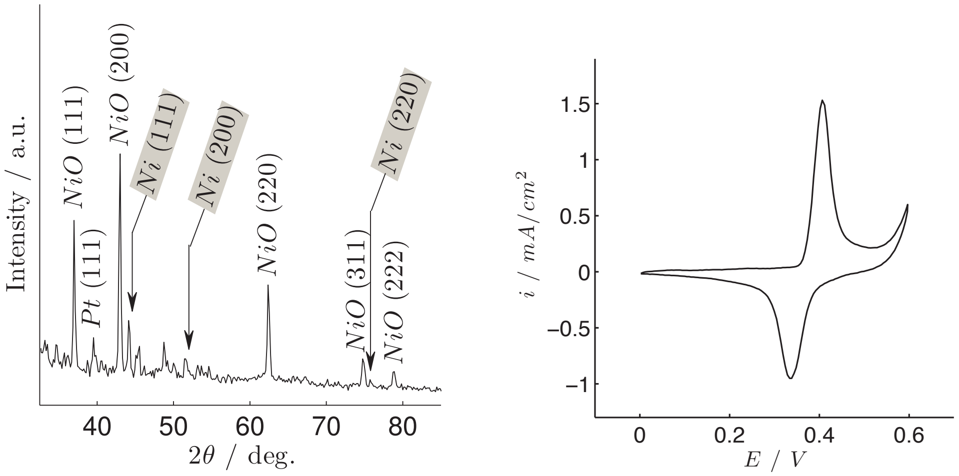

(c) Powder XRD patterns.

(d) Cyclic voltammetry.

Figure 7.3.: SEM micrograph (7.3(a)), EDX spectrum (7.3(b)), powder X-ray diffraction patterns (7.3(c)) and cyclic voltammogram (7.3(d)) of the as-prepared nanoparticles synthesized with Pt cathode vs. Ni anode in 2 M H_2SO_4 + 0.5 M Et + PVP40 at 36 V during 3 hours.

used cathode is a platinum wire. The energy-dispersive X-ray spectrum in Figure 7.3(b) shows the energies of the two L- and K-peaks of emission lines of nickel. The detected copper is the background copper of the grid while the traces of sulfur are from the operating solution in which the nanoparticles are synthesized. The powder X-ray diffraction pattern in Figure 7.3(c) shows mainly nickel-based materials. All phases of Ni and NiO are perfectly indexed with the referred ones from the JCPDS Cards # 04-0850 and # 78-0643 respectively:

- the (111), (200) and (220) planes of pure nickel material (JCPDS Card # 04-0850), and
- the (111), (200), (220), (311) and (222) planes of nickel oxide (JCPDS Card # 78-0643).

A tiny fraction of the (111) plane of platinum is also detected in the XRD pattern but it represents less than 2% of the overall counts. Note that the XRD results of Section 6.3 for the different voltages (Figure 6.11) and duration of the experiments (Figure 6.13) do not show the nickel element. It is believed that it is probably the presence of platinum which inhibits the formation of a comparable fraction of NiO nanoparticles. Additionally, from the work of Guilpin and Garbarz-Olivier (*44*), the recorded spectrochemical results of Pt cathode in a virgin sulphuric acid solution at unit molarity show the emission lines of Pt(I), Pt(II), H and OH, which is in line with the detected fraction of platinum in the XRD patterns[‡]. The electrochemical activity in shown with the 50 mV/s voltammogram in Figure 7.3(d) which is typical for nickel in the positive window 0.0 to 0.6 V vs. Ag/AgCl reference electrode.

The characterization results of this sample, when compared with the ones in Section 6.3, confirm that metal ions provided by the anodic dissolution of the nickel plate are reduced *in situ* by the strong reducing species generated from water radiolysis reactions. It also witnesses of the dual combination of both proposed mechanisms due to the presence of the Pt element believed to be provided from the sputtering process of the platinum cathode.

In summary, this so-called gas-liquid interface mechanism explains the reduction of the metal cations M in the primary reaction zone of Hickling and Ingram (*35*)

[‡] More details will be given in Section 7.1.2 with the second proposed mechanism based on the electrode material sputtering.

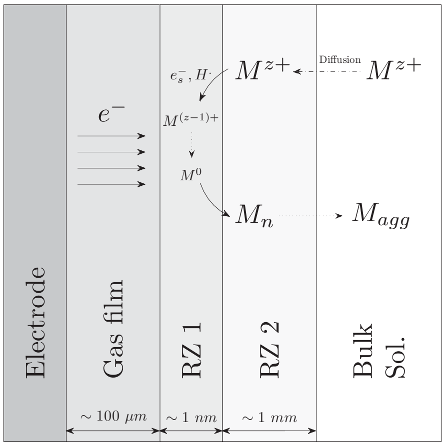

Figure 7.4.: Metal ion reduction mechanism for the synthesis of nanoparticles by electrochemical discharges. *RZ 1* and *RZ 2* represent the primary and secondary reaction zones of Hickling and Ingram (*35*).

as illustrated in Figure 7.4 (compare with Figure 2.5 in Section 2.3). The reduction reactions where the metal cations M become zero-valent atoms involve the e^-_{aq} and $H^\cdot$ radical as well as the radicals formed if a scavenger of $OH^\cdot$ is added to the solution to prevent the oxidation reaction. Otherwise, it is the oxidation process which shall take place to oxidize the ions M or their atomic versions to a higher state of oxidation.

7.1.2. Electrode-gas Interface

The second proposed mechanism is a surface effect and is based on the work and discovery of Grove (*187*) in 1852. Through a number of experiments, Grove concluded with the possible disintegration of negatively polarized electrodes by cation impacts using gas discharges. The sputtered materials from the cathode were then deposited on the inner wall of the discharge tube. This observation led to numerous experimental investigations and theoretical attempts to explain the phenomenon knowing that initially it was an undesired phenomenon as the electrode material is destroyed. A historical overview, from the considerable works of Kingdon and Langmuir in 1923 up to Thompson in 2004, among others, is presented. It is believed that this should give a brief introduction to the electrode sputtering phenomenon in the attempt to explain what could be happening at the electrode surface during the electrochemical discharges so that colloidal nanoparticles are obtained.

In 1923, experimental evidence was presented by Kingdon and Langmuir (*188*) of a special case of sputtering when they bombarded thoriated tungsten with different kinds of ions in a glow discharge tube. Indeed, they remarked during their experiments the disintegration of the thin film of thorium on the tungsten substrate rather than the tungsten itself. In addition to that, they concluded that the sputtering rate, which represents the atoms removed by incident ion impact, increases with the incident ion mass and ion energy. Kingdon and Langmuir proposed, at that time, the so-called *momentum transfer model*, an ejection mechanism for the electrode sputtering phenomenon. They proposed that two successive bombardments on the same thorium atom of the thoriated tungsten filament or electrode are necessary for its disintegration. The first impact should generate atomic size crater at the electrode surface while the second impact of the ion, in the bottom of this depression, should remove one of the surrounding thorium atoms by reflection. The second impact will be able remove the thorium atom if the energy transferred is still greater than its atomic heat of vaporization (*190*).

An important contribution to the field was the findings showing deposit patterns from sputtering single crystal planes made by Wehner (*191*). The author remarked high density spots at the electrode surface which is in accordance with the momentum transfer theory proposed by Kingdon and Langmuir (*188*). The work of Henschke (*192*) reported in 1957 is based on mechanical collision theory and took into account oblique and normal incidence sputtering phenomena. In summary,

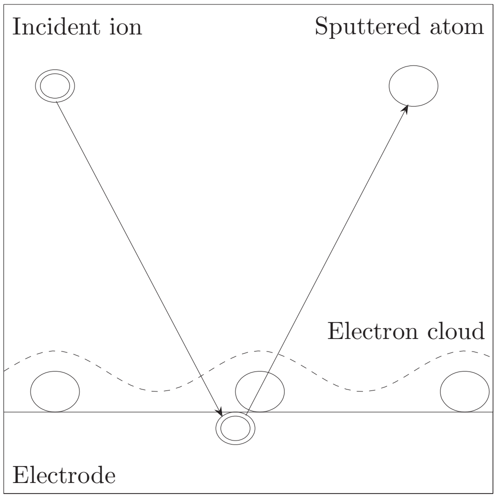

Figure 7.5.: Mechanism of nanoparticles synthesis by electrochemical discharges via electrode sputtering by incident ion collision, adapted from Henschke (*192*).

the oblique impact sputtering involves the atoms belonging to the outermost plane of the electrode surface and therefore it is a two-body collisional process. The incident ion penetrates the surface plane with an angular momentum and hit the atom on its inside hemisphere to obtain an *impulse* momentum oriented outward normal to the surface. Figure 7.5 is an illustration of the oblique ion incidence at an atom belonging to the outermost plane causing the sputtering of that atom. The more complex multi-body collisional process of ions normally incident to the electrode surface can be found in Henschke (*192*). With an energy superior than the heat of vaporization, which corresponds to the bounding energy necessary to the atom to repose on the surface, the atom could be ejected. Minimum threshold energies for different contact angles and surface atom separations were calculated by the Henschke. Additional reviews and relevant works about sputtering and cluster formation are available elsewhere (*189*, *193–200*), where in summary, it is to be retained that the sputtering yield is influenced by:

- the energy and incident angles of ions, and

- the nature and crystal arrangement of target material.

7.1.2.1. Mechanism

The discharge regime during the electrochemical discharges is qualitatively similar to the material sputtering under ionic bombardment in gas discharges. Different researchers, especially in the field of micro-machining structures with electrochemical discharges and standard electrochemical techniques, pointed out this electrode erosion effect (*2*, *47*, *178*, *201–204*). According to these authors, the electrode is subject to local chemical etching process and, to a certain extent, to heating effects. Naturally, it is understood that the chemical etching rate is enhanced by the microscopic kinetic temperature generated at the electrode surface by the discharges themselves. The ion bombardment, during electrode sputtering phenomenon, unifies these explanations, by referring to the different parameters controlling the sputtering rate from the overview of Massey and Burhop (*205*).

More specifically for the nanoclusters fabrication by electrochemical discharges, positively charged ions present in the solution are accelerated towards the gas film and then cross it, due to the high electric field gradient, to strike the electrode surface. The ions present is the solution come either from the dissolution of the anode or from the solute. These ions are required to have an energy superior than the heat of vaporization of the target atom at the surface, which in general does not surpass the 10 eV for most of the transition metals (*192*). For example, ΔH_v at 25°C of Ni is 4.41 eV and of Pt is 5.86 eV (*192*), knowing that the cathodic electrochemical discharges in aqueous solutions carry energies of several tens of electronvolts . Micro-hollow cathode discharges operating at atmospheric pressure for the synthesis of nanoparticles are pretty similar to this concept. The cathode micro-hole plays the role of a confined micro-reactor of discharges in which the ions generate the nano-materials by cathode sputtering (*118*, *206*). Once the zero-valent

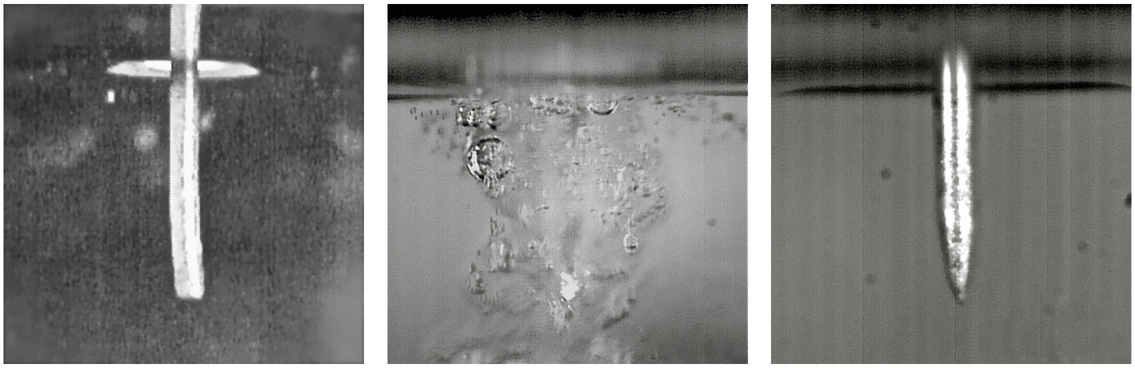

(a) Initial shape of cathode.

(b) Discharges emitted from the tip of the cathode.

(c) Cathode after a few hours of discharging.

Figure 7.6.: Evolution from cylindrically- to conically-shaped ⌀0.5 mm Ni cathode after a few hours of discharges at 45 V in 3 M KOH aqueous solution, courtesy of Zahra Ghorbani.

atoms are diffused out of the gas film towards the bulk solution, nucleation reactions and coalescence follow the same scheme as Reactions 7.13.

7.1.2.2. Arguments

The first argument in favor of this proposed mechanism can be verified with naked eye. Figure 7.6 shows how the 0.5 mm diameter nickel wire looks like after a few hours of discharging at 45 V in 3 M of KOH aqueous solution. The high concentration of glow discharges visible at the tip of the electrode, as illustrated in Figure 7.6(b), shows that the disintegration of the electrode material is related to the density of discharges.

In the experimental arrangement where both electrodes are made of nickel and the electrolyte is a 5 M KOH aqueous solution, there are no stable Ni^{+}/Ni^{2+} ions possible. This is clear from the Pourbaix diagram of nickel shown previously in Figure 6.3. The potassium hydroxide is dissociated to positively charged K^{+} ions and to OH^{-}. Thus, one cannot expect metal reduction by the solvated electron and/or the hydrogen radical presented in the first proposed mechanism in Section

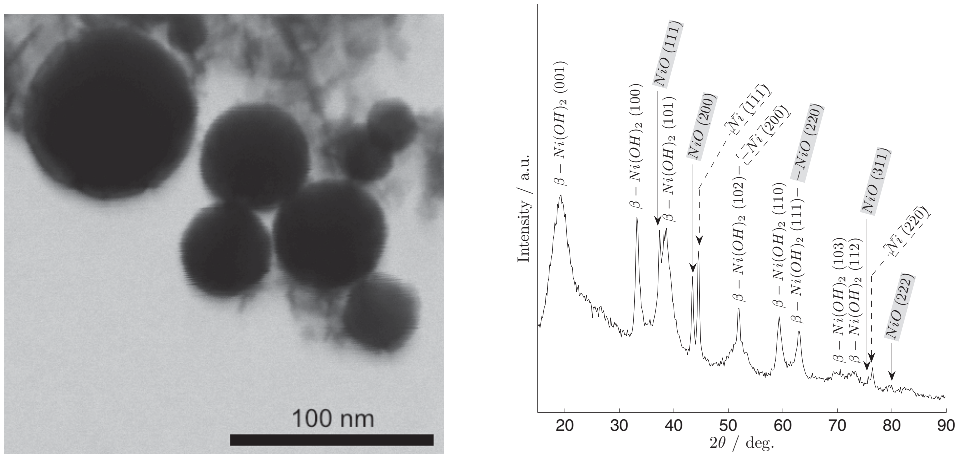

(a) STEM micrograph.

(b) Powder XRD patterns.

Figure 7.7.: STEM micrograph (7.7(a)) and powder X-ray diffraction patterns (7.7(b)) of the as-prepared nanoparticles synthesized with Ni cathode vs. Ni anode in 5 M KOH 50 V during 1 hour.

7.1.1. Within a few minutes of experiment, one can observe a layer starting to develop from the vicinity of the electrode at the top of the solution. This layer is cloudy and of a dark gray to black color, typical for nickel nanoparticles, and gets more and more thick and dense with time. Figure 7.7(a) shows a micrograph of nickel nano-materials from this sample as well as their crystal identification from the powder XRD patterns in the adjacent Figure 7.7(b). The particles are of spherical shapes and of size less than 100 nm. The powder XRD has different phases of nickel including:

- the (111), (200) and (220) planes of pure nickel material (JCPDS Card # 04-0850),
- the (111), (200), (220), (311) and (222) planes of nickel oxide (JCPDS Card # 78-0643), and
- the (001), (100), (101), (102), (110), (111), (103) and (112) of β-phase of nickel hydroxide (JCPDS Card # 01-1047).

All these elements are identified in the Ni-O-H Pourbaix diagram at high alkaline pH, as previously shown in Figure 6.3.

Another supporting evidence of the sputtering mechanism in electrochemical discharges is the characterization of the particles manufactured in 5 M KOH as in the previous experiement but with Pt cathode instead, and still vs. Ni anode. The SEM image of Figure 7.8 shows agglomerated nanoparticles of Pt of less than 10 nm average size. The chemical composition is confirmed by the EDX spectrum in Figure 7.8(b), in which the detected copper element is the background copper of the SEM carbon-coated cupper grid. The element S is mainly due to remaining impurities in the glassware from other experiments of nanoparticles synthesis. The powder XRD patterns of Figure 7.8(c) which are perfectly defining the peaks of planes (111) at 39.79°, (200) at 46.19°, (220) at 67.48°, (311) at 81.25° and (222) at 85.89° of face-centered cubic lattice structure of the platinum crystal. No traces of nickel or its oxide/hydroxide are found. The broadening of the XRD peaks is an indication of the small size of the crystallite which is found to be 8.7 nm by applying Scherrer's formula using the most intense peak (111) which is in line with the measurements from the SEM micrograph in Figure 7.8(a). A fourth characterization of the obtained particles is done by cyclic voltammetry vs. the Ag/AgCl reference electrode in the -0.2 to 1.2 V potential range of the as-synthesized nanoparticles of platinum deposited onto a freshly polished graphite electrode. The supporting electrolyte is a 0.5 M H_2SO_4 aqueous solution and the scan rate is 50 mV/s. Figure 7.8(d) show the obtained voltammogram, typical of polycrystalline platinum, which exhibits different reactions according to four regions separated by dashed lines. The first region marks the overall anodic and cathodic peaks of adsorption and desorption of hydrogen on the different planes of platinum. Region *2* corresponds to the double-layer capacity region, while Region *3* and its subsequent peaks marks the formation of Pt-oxides during the anodic polarization and their reduction durring the opposite

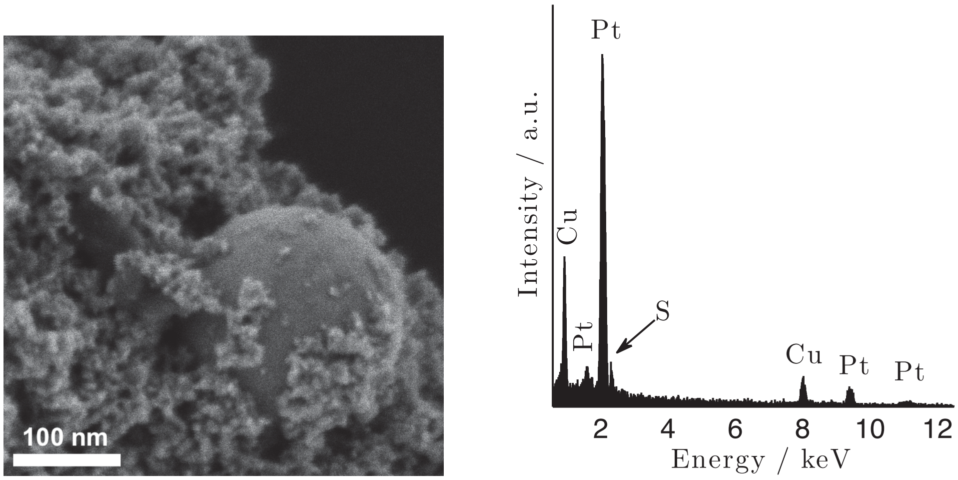

(a) SEM micrograph.

(b) EDX spectrum.

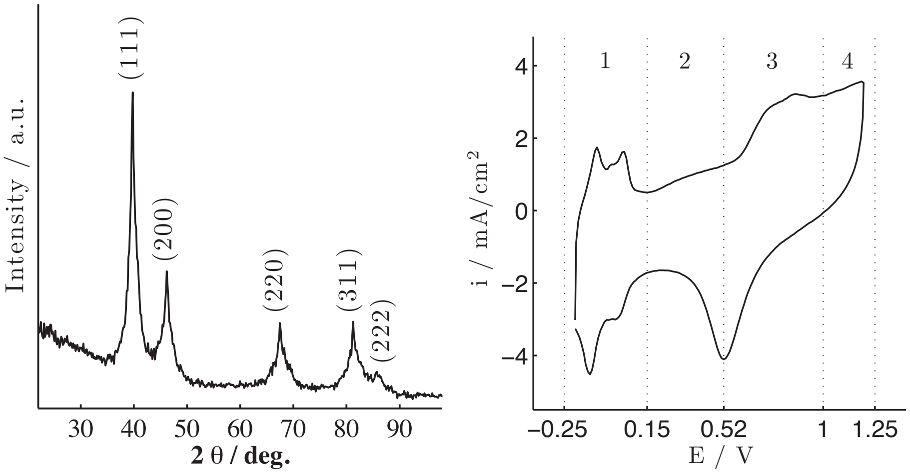

(c) Powder XRD patterns.

(d) Cyclic voltammetry.

Figure 7.8.: SEM micrograph (7.8(a)), EDX spectrum (7.8(b)), powder X-ray diffraction patterns (7.8(c)) and cyclic voltammogram (7.8(d)) of the as-prepared nanoparticles synthesized with Pt cathode vs. Ni anode in 5 M KOH 50 V during 3 hours.

scan. The last region in the Pt voltammogram corresponds to a flat plateau preceding the oxygen evolution reaction. In addition to these series of characterizations, from the recorded spectra of the cathodic electrochemical discharges at a platinum electrode in KOH solution, Guilpin and Garbarz-Olivier (*44*) found the emission rays of Pt(I), Pt(II), K(I), K(II), H and OH. This spectrochemical analysis suggests

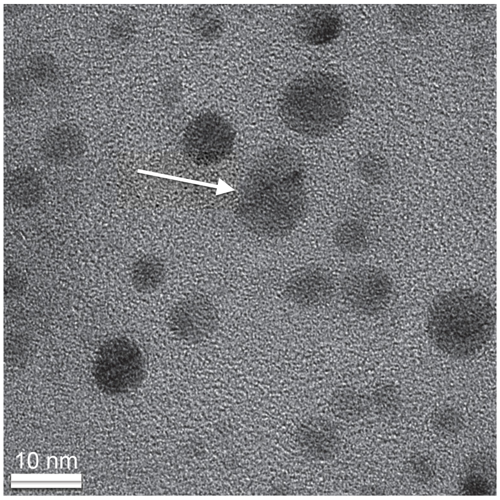

Figure 7.9.: TEM micrograph of the as-prepared nanoparticles synthesized with Ni cathode vs. Ni anode in 1 M H_2SO_4 at 32 V.

conclusively that the electrode is under bombardment by potassium ions and the platinum is being ejected progressively from the electrode surface.

Remark 7.1. Dislocation type of defects are observed in some of the particles as illustrated by the arrow in the TEM image of Figure 7.9. The arrow points to a nanocluster of nickel in which the planes of atoms are not in a straight line, which suggests that there is also the possibility to obtain the particles by melting followed by rapid cooling of the electrode material (*21*, *161*). This has been also confirmed by the results of Toriyabe et al. (*6*), where the authors have shown spherical particles of several hundreds of nanometers at the surface of the working cathode itself. These crystallographic defects are caused by high current densities discharges and it represents a negligible fraction of the synthesis mechanism. The presented technique in Toriyabe et al.'s work operates at some tens of electronvolts only.

In conclusion, it is shown that the synthesis of zero-valent atoms by electrochemical discharges follows a weighted combination of the two models proposed in this Section. Several parameters and constraints may favor one mechanism over the other, such as the electrolyte and its composition, the electrode material and the applied terminal voltage. This technique is compared to other methods for the synthesis of nano-sized materials in Table 7.2. The electrochemical methods in two- and three-electrode setups, radiolysis and electric discharges have been reviewed previously in Chapter 5. The main advantage of the electrochemical discharges when applied to nanoscience is its low cost when compared to the electric discharges or the radiolysis technique. Its simplicity in setting up the operating conditions makes it a very useful route for laboratory needs. However, because the synthesis of nano-materials is locally restricted to the vicinity of the cathode, using one single working electrode and of small diameter does not produce large quantities of products. For example, the mass of nickel oxide nanoparticles synthesized at 30, 36 and 42 V during 3 hours in 2 M H_2SO_4 + 0.5 M Et. + PVP40 with 0.5 mm diameter Ni cathode vs. Ni anode is around 1.1, 1.6 and 2.9 mg. The difference between this technique and low current electrochemical methods is that the process produces naturally high local temperatures at the surface of the cathode. This feature could be suitable in the manufacturing of shapes other than the natural ones of the targeted material.

The control of the initial number of particles and their subsequent growth with time is crucial in achieving the desired size and its monodipersity as well as the overall production yield. Therefore, some general statements about supersaturation and the classical nucleation theory as well as crystal growth processes are treated hereafter in the aim to present a global picture of the process from the early building blocks to the stable nano-materials.

Table 7.2.: Comparison of some synthesis techniques of nano-sized metals in aqueous solutions with the cathodic electrochemical discharges.

	Electrochemical methods	**Radiolysis**	**Electric discharges**	**Electrochemical discharges**
Precursors	Anodic dissolution	Metal salts	Electrode disintegration	Anodic dissolution, metal salts, electrode disintegration
Reducing agents	e^-, stabilizers	e^-_{aq}, $H^\cdot$, secondary radicals	N/A	e^-_{aq}, $H^\cdot$, secondary radicals
Power	∽ 1 mW	∽ 10-20 kW	∽ 5-10 W	∽ 0.1-1 W
State	Colloids	Colloids	Colloids, aerosols	Colloids
Yield	∽ g/hr	∽ g/hr	∽ mg/hr	∽ mg/hr
Initial cost	Low	High	Medium–High	Low

7.2. Nucleation and Crystal Growth

Firstly, the thermodynamic analysis of nucleation theory is recalled and adapted to the electrochemical discharges where the formed nucleus is supposed to be in its equilibrium static state without any details about its time-dependent evolution. Naturally this is an insignificant event in real situations, thus in a second part, the kinetics of the classical nucleation theory are considered. Conceptual description of crystal growth, from LaMer and Dinegar diagram is reviewed to draw the overall picture of the synthesis of colloidal nanoparticles by electrochemical discharges: from ions to atoms and nuclei to clusters and nano-sized particles. In short, this Section treats in detail the following consecutive series of Reactions of nucleation and coalescence to crystal growth:

$$\mathrm{n\,M^0} \longrightarrow \mathrm{M_2} \longrightarrow \cdots\ \mathrm{M_n}\ \cdots \longrightarrow \mathrm{M_{agg}} \tag{7.18}$$

7.2.1. Thermodynamics of Nucleation

The thermodynamic driving force for the nucleation process leading to colloidal nanoparticles, is the degree of supersaturation $\Delta\mu$, the difference between the liquid and solid chemical potentials μ (*208*, *209*). The chemical potential is by definition the change in Gibbs free energy with respect to the number of particles n in the system at constant pressure p and constant temperature T (*11*, *58*, *64*):

$$\mu = \left(\frac{\partial G}{\partial n}\right)_{p,T} \tag{7.19}$$

In other words, the supersaturation $\Delta\mu$ corresponds to the gain in free energy per molecule due to the transition from the thermodynamic potential of higher Gibbs free energy to lower Gibbs free energy. For simplicity, the formation of a spherical liquid droplet in a bulk gaseous phase is considered, which will be then generalized

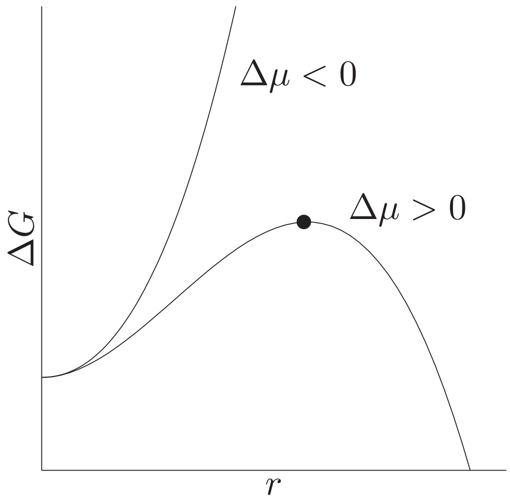

Figure 7.10.: Gibbs free energy of nucleation of nuclei.

to the nucleation from other supersaturated phases. Assume that the gas phase is composed of n_g moles with a chemical potential μ_g. A spherical liquid droplet of radius r and with chemical potential μ_l formed from n_l moles of gas will generate a change in the Gibbs free energy such that (*210*, *211*):

$$\Delta G = G_2 - G_1 = -n_l(\mu_g - \mu_l) + 4\pi r^2 \gamma \tag{7.20}$$

with γ the surface tension of the liquid droplet. By writing the number of moles of the liquid droplet n_l be equal to the fraction of its volume $4\pi r^3/3$ by the molecular volume v_l, one obtains the following expression of Gibbs free energy:

$$\Delta G(r) = -\frac{4\pi r^3}{3v_l}\Delta\mu + 4\pi r^2 \gamma \tag{7.21}$$

Depending on the sign of the supersaturation value $\Delta\mu$, Figure 7.10 shows two different behaviors of the variation of $\Delta G(r)$ with r. The case when $\Delta\mu$ is negative, which means that the gaseous phase is more stable than the liquid phase, leads to the infinite increase of $\Delta G(r)$. Therefore, the nucleation of the liquid droplet is thermodynamically impossible. In the contrary case, when $\Delta\mu$ is positive, Figure 7.10

shows that the Gibbs free energy variation has an unstable equilibrium at the critical radius value r_c:

$$r_c = \frac{2\gamma v_l}{\Delta\mu} \tag{7.22}$$

Equation 7.22 is known as the Thomson-Gibbs Equation for the equilibrium of a nucleus in its ambient environment. Physically, this is to say that if more atoms or molecules join a nucleus of critical radius r_c, the nucleus will have the tendency to grow further.

Now consider the case of a colloidal dispersion of materials prepared with electrochemical discharges. From Figure 6.6, one can observe a large population of nanoparticles with mean diameter of 70 nm. In the same sample nanoparticles of 10 nm and over 500 nm are also observed. The small particles have more geometric curvatures and more important surface energies, and therefore a diffusional flow is expected from the small particles to the large ones to diminish the total energy of the system. In other words, the mixture of small and large particles initially present in the solution is not at thermodynamic equilibrium and the total energy of the system will tend to be diminished by decreasing the surface area i.e. increasing the size of the larger particles (*212*). The spontaneous process due to the random energy fluctuations in the solution and known as the Ostwald ripening takes place. The concept of Ostwald ripening can be illustrated by Figure 7.11.

From the steady state nucleation, the main conclusion is that the formed building units will nucleate progressively according to the very early stages of Reactions 7.18 to form clusters of a minimum size. At the late stages of nucleation, these colloidal clusters will then have the tendency to diffuse and contribute to increase the size of larger particles, according to the Ostwald ripening theory. The stabilization of the size of manufactured particles is a continuous competition between the nucleation and the stopping of growth with, for example, stabilizing polymers, organic and charged molecules.

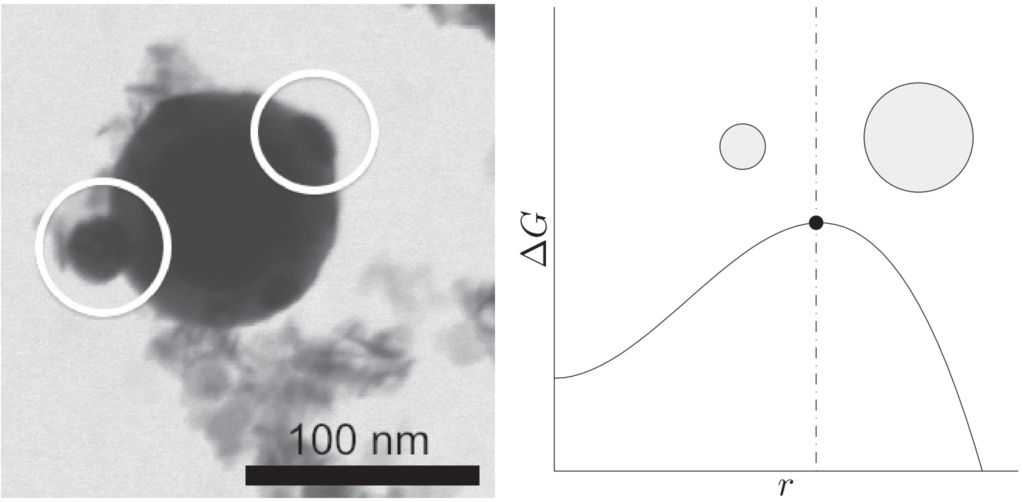

(a) Coalescence of nanoparticles.

(b) Oswald ripening.

Figure 7.11.: Coalescence of nanoparticles synthesized with electrochemical discharges with Ni cathode vs. Ni anode in 5 M KOH at 50 V during 1 hour.

7.2.2. Kinetics of Nucleation

The concepts of nucleation of atoms to form stable clusters from the reduced M^0 atoms to M_2 until M_n, has been considered from the thermodynamic point of view which describes the steady-state static process. In real situations, the kinetic analysis of nucleation is the only significant result. More specifically, as the number of building units, the M^0 atoms, generated by both proposed mechanisms for the formation of nanoparticles by electrochemical discharges is a random quantity, the kinetic considerations of nucleation are required to fully explain the process (*209*, *210*, *213*–*215*).

Prior to that, let us recall the reactions of dimerization and recombination during the electrochemical discharges. The reactions to be considered are ones involving the strong reducing agents, the hydrated electron e^-_{aq} and the $H^{\cdot}$ radical, and the strong oxidizing agent, the $OH^{\cdot}$ radical (see Table 7.1):

$$e^-_{aq} + e^-_{aq} \longrightarrow H_2 + 2\,OH^- \tag{7.23}$$

$$e^-_{aq} + H^{\cdot} \longrightarrow H_2 + OH^- \tag{7.24}$$

$$e^-_{aq} + OH^{\cdot} \longrightarrow OH^- \tag{7.25}$$

$$H^{\cdot} + H^{\cdot} \longrightarrow H_2 \tag{7.26}$$

$$H^{\cdot} + OH^{\cdot} \longrightarrow H_2O \tag{7.27}$$

$$OH^{\cdot} + OH^{\cdot} \longrightarrow H_2O_2 \tag{7.28}$$

With the aqueous solution containing the metal ions M^{z+}, the following Reactions take place:

$$e^-_{aq} + M^{z+} \longrightarrow M^{(z-1)+} \tag{7.29}$$

$$H^{\cdot} + M^{z+} \longrightarrow M^{(z-1)+} + H^+ \tag{7.30}$$

$$OH^{\cdot} + M^{z+} \longrightarrow M^{(z+1)+} + OH^- \tag{7.31}$$

Referring to Figure 7.4, it is understood that Reactions 7.29 to 7.31 occur in the primary reaction zone. With the assumption that the concentration of ions M^{z+} is high enough, it can be assumed that mutual reactions of radicals from the set $\left\{e^-_{aq}, H^{\cdot}, OH^{\cdot}\right\}$ will happen at low rates in comparison with the ones involving the ions M^{z+} (*51*, *216*). This can be justified from the early experiments of Fricke et al. (*217*) where the irradiation of solutions of acetone in sulfuric acid produced very little amounts of H_2O_2 and the yield of H_2 decreased with the increased concentrations of acetone. This can be explained by the continuous competition of acetone and H^+ for the hydrated electron (*218*). Baxendale and Dixon (*219*) have shown strong reducing yield of H_2 in neutral aqueous methanol solutions containing a small concentration of ions such as Pb^{2+}, Cd^{2+} and Ni^{2+}. For example, adding some 10^{-4} M of Ni^{2+} to a 0.1 M aqueous solution of methanol, decreased G(H_2) of the irradiated solutions by more than 50%.

In the secondary reaction zone, *RZ 2*, cascade coalescence lead to the nucleation process. The master equation is derived by considering the following simplifying assumptions (*209*, *210*):

1. The cluster geometrical shape does not change with time.
2. The supersaturation value $\Delta\mu$ between the solid and liquid phase does not change with time.
3. The nucleation process is a series of reversible binary reactions, analogous to the birth-death process (*220*, *221*) and can be written (*210*):

$$\begin{aligned}
\mathrm{M_1} + \mathrm{M_1} &\underset{k_2^-}{\overset{k_1^+}{\rightleftharpoons}} \mathrm{M_2} \\
\mathrm{M_2} + \mathrm{M_1} &\underset{k_3^-}{\overset{k_2^+}{\rightleftharpoons}} \mathrm{M_3} \\
&\cdots \\
\mathrm{M_{n-1}} + \mathrm{M_1} &\underset{k_n^-}{\overset{k_{n-1}^+}{\rightleftharpoons}} \mathrm{M_n} \\
\mathrm{M_n} + \mathrm{M_1} &\underset{k_{n+1}^-}{\overset{k_n^+}{\rightleftharpoons}} \mathrm{M_{n+1}} \\
&\cdots
\end{aligned}$$

where k_n^+ and k_n^- ($n = 1, 2, \ldots$) represent, respectively, the constant rates of reactions of attachment and detachment of a single atom $\mathrm{M_1}$[§] to and from the cluster composed of n atoms $\mathrm{M_1}$ and denoted by $\mathrm{M_n}$. This can be schematized as follows:

$$\mathrm{M_{n-1}} \xleftarrow[-\mathrm{M_1},\ k_n^-\ \text{(detachment)}]{} \mathrm{M_n} \xrightarrow{+\mathrm{M_1},\ k_n^+\ \text{(attachment)}} \mathrm{M_{n+1}} \tag{7.32}$$

[§] $\mathrm{M_1}$ is what has been previously denoted by $\mathrm{M^0}$, and for seek of coherence in the indices of parametric equations, it is the former that will be in use in this Section.

4. Many-body collisions are not considered.

From kinetic chemistry, the time change of the concentration of the nuclei formed by n times M_1 can be expressed as follows (*210*):

$$\frac{d[\mathrm{M_n}]}{dt} = \left(k^+_{n-1}[\mathrm{M_{n-1}}] - k^-_n[\mathrm{M_n}]\right) - \left(k^+_n[\mathrm{M_n}] - k^-_{n+1}[\mathrm{M_{n+1}}]\right) \tag{7.33}$$

which in terms of net fluxes can be rewritten as:

$$\frac{d[\mathrm{M_n}]}{dt} = J_n - J_{n+1} \tag{7.34}$$

In the time-independent state, $d[\mathrm{M_n}]/dt = 0$, which defines the frequency of formation of clusters of a given class n (*210*):

$$J_n = J_{n+1} = J_0 \tag{7.35}$$

From Appendix B the nucleation rate J_0 is expressed by (*210*):

$$J_0 = 4\pi r_c^2 C\nu\lambda \exp\left(\frac{-\Delta G_{des}}{k_B T}\right)\Gamma \exp\left(\frac{-\Delta G_c}{k_B T}\right) \tag{7.36}$$

with C the concentration of clusters of class n present in the solution, ν a frequency factor, λ the mean free path of clusters in the solution, ΔG_{des} the energy of desolvation, Γ the Zeldovich factor and ΔG_c the critical Gibbs free energy. In summary, from Equation 7.36, engaging the zero-valent atoms, generated from the reactions with reducing species or from the sputtering of the electrode, into the nucleation of more clusters requires the following:

- larger critical radius value of clusters which is an intrinsic property of the material,

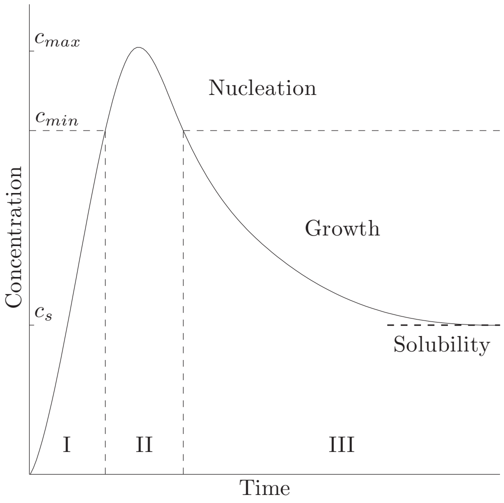

Figure 7.12.: LaMer and Dinegar diagram.

- higher concentration of the generated zero-valent atoms, which can be done at more stable situations of the gas film and at higher voltages,
- higher bulk temperature,
- lower energy barrier of desolvation which is due to the encapsulation of the small nuclei by the molecules of the electrolyte, or in other words lower viscosity of the electrolyte, and
- lower critical Gibbs free energy which is also related to targeted material and to the electrolytic solution.

7.2.3. Crystal Growth and Stabilization

The growth process of the colloidal particles is conceptually discussed in this section based on LaMer and Dinegar diagram (*207*, *222*). The diagram is illustrated in Figure 7.12 and shows schematically the extent of the nucleation process and the subsequent growth with time, which is the case for the colloidal clusters synthesized by electrochemical discharges. In its first region *I*, it shows that the continuous supply of atoms M^0 to the solution makes its concentration proportional to time until reaching the critical supersaturation c_{min}. It corresponds to the minimum supersaturation value for the nucleation process to start which is above the equilibrium solubility concentration. It is actually related to the energy barrier that has to be surpassed so that the nucleation can effectively take place.

Indeed, region *II* in the diagram is the time interval of nucleation which takes place at concentrations of the M^0 precursors between c_{min} and c_{max}. To ensure the monodispersity of the colloids, the nucleation process in region *II* should be as short as possible by controlling, for instance, the initial concentration of the supplied building blocks M^0 and the supersaturation of the medium. In the ideal case, the monodispersity of nano-sized materials fabricated by electrochemical discharges in aqueous solutions can be assured if actually all the nuclei are formed exactly at the same time with the same number of building blocks, so that statistically, they will all have the same growth. This could be technically challenging because this technique is characterized by the local production of particles in the vicinity of the working electrode, which is opposite to the case of wet chemistry or radiolysis techniques where the products are synthesized uniformly in the whole bulk solution. The growth process is already slightly active in this second region when there are of course some nuclei in the solution, but when the concentration reaches the maximum value c_{max} the growth rate gets higher and the concentration of nuclei tends to decrease to the concentration c_{min}.

As the system is still supersaturated, the generated stable nuclei in region *II* undergo the growth process by diffusion and contribute to the growth of larger particles already in region *III* as illustrated in Figure 7.11(a) or previously shown in Figure 6.6(b). The encircled left part in Figure 7.11(a) shows the adsorption of a particle onto the surface of a larger one. The right encircled part shows a more advanced process where another particle which has been already adsorbed on the growth surface is undergoing its irreversible adhesion or incorporation within the large central particle. That is what explains, for instance, the values in Table 6.3, where the mean diameter of NiO nanoparticles increases with the experiment duration from 60 to 70 to 79 nm at 1, 3 and 5 hours respectively, giving more time to the growth process. Here, there is another window where the nanoparticles size distribution can be adjusted by controlling the diffusion growth process using some stabilizing agents, for example.

The stabilization procedure should make sure to stop further agglomerations by countering the van der Waals forces ($\mathbf{F}_W$) and the magnetic dipole-dipole interactions ($\mathbf{F}_M$) once a desired nanometric size is reached. The stabilizing agent can ensure either or both of these two functions: electrostatic stabilization ($\mathbf{F}_E$) or steric stabilization ($\mathbf{F}_S$) (*95*). The total attractive and repulsive forces acting on a colloidal dispersion of nanoparticles can be written as:

$$\mathbf{F}_T = \underbrace{(\mathbf{F}_W + \mathbf{F}_M)}_{Attraction} + \underbrace{(\mathbf{F}_E + \mathbf{F}_S)}_{Repulsion} \tag{7.37}$$

The electrostatic or Coulombic repulsion can be explained by repulsion of the electric layers built by the adsorbed ions on the surface of the colloidal nanoparticles. The steric stabilization, however, is ensured by the addition of long chain polymeric molecules or surfactants to the solution which will be adsorbed on the particles surfaces and prevent them from agglomerating. Two ways can explain the steric repulsion function of these high molecular weight molecules (*95*). The first is due to the overlapping chains of the macro-molecules between two particles approaching each others which restricts their motion and decreases the total entropy of the system. The second phenomenon related to the steric repulsion can be explained by the osmotic effect due to the high gradient of macro-molecules concentrations between the inter-particles space and the rest of the solution (*95*). The system will tend to dilute the polymer or surfactants to return back to the equilibrium state which will naturally separate the nanoparticles. Several sorts of polymer are used in nanoscience and colloidal chemistry such as gelatin, cellulose acetate, cellulose nitrate and poly(vinyl-pyrrolidone), which has been used for this work to slow down the growth process of the synthesized nanoparticles.

7.3. Conclusion

This Chapter on the mechanisms of nanoparticles synthesis by electrochemical discharges can be summarized by Figure 7.13, where the successive reactions and processes can be enumerated as follows:

1. Electrons emitted by the cathode cross the gas film to irradiate the water molecules in the first reaction zone, *RZ 1*, and positively charged ions cross it in the opposite direction to hit the cathode and diffuse zero-valent atoms to *RZ 1*,
2. Reducing and oxidizing species are generated by water irradiation in *RZ 1* and in which they will compete when reacting with the metal ions M^{z+},
3. Zero-valent M^0 precursors generated by metal ions reduction and electrode sputtering undergo the nucleation process and Ostwald ripening in the secondary reaction zone,
4. Nano-sized materials are generated by coalescence and crystal growth in the bulk solution.

The synthesis of nanoparticles by electrochemical discharges is punctual where all key time-dependent steps occur around the cathode insulated by the gas film. This makes the nanoparticle size control and their quantitative yield to be a compromise between the following parameters:

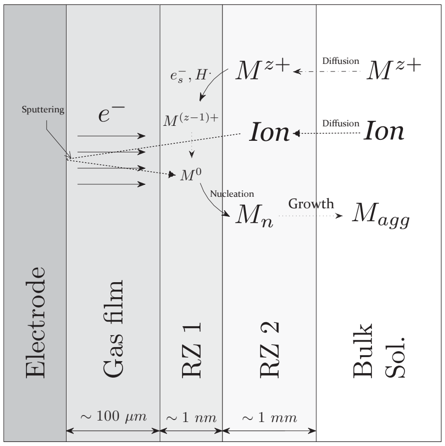

Figure 7.13.: General mechanism of nanoparticles synthesis by the electrochemical discharge phenomenon in aqueous solutions.

- The gas film stability and the applied terminal voltage,
- The quantity of reducing versus oxidizing species available in the solution,
- The extent of the nucleation and growth processes times, and
- The growth stabilization technique.

Chapter 8

Nickel Oxide Supercapacitors

> *We see portability in electronics being a continuing requirement, higher functionality, better battery life, requiring lower power for the actual electronics.*
>
> *(David Milne)*

The continuous increase of consumption and demand for the non-ecologically friendly fossil fuel has pushed more and more towards the development of other sustainable sources of energy (*223*). Electric energy generated from solar radiation and wind turbines fields, for example, is not continuous in time and thus there is a need to implement reliable energy storage systems along with these power production processes (*160*). The electric energy can be directly stored by applying electrostatic charges at the poles of a capacitor or indirectly stored in a battery. In the later case, the energy is in fact stored in terms of chemical energy that is converted to the electric energy when faradic redox reactions are imposed on the system. This Chapter aims to present the electrochemical energy storage capability of the synthesized nickel oxide nano-materials by electrochemical discharges.

8.1. Electrochemical Energy Storage

By applying a voltage on the poles of a capacitor, the system will be charged and will store energy by means of static charges. Capacitors are usually categorized function of their capacitance strength into three groups as follows (*224*, *225*). The first is the electrostatic capacitor which is a device consisting of two plates separated by a dielectric medium or sometimes vacuum and is characterized by a low capacitance C, usually in the range of pico- to nano-farads in actual applications. The storage energy for a given potential difference between the electrodes is expressed by $\Delta G = \frac{1}{2}Q\Delta V$ and normally it is limited only by the electric breakdown of the dielectric element at high enough ΔV values (*224*). The second category is for the electrolytic capacitor which is the conventional electrochemical energy storage arrangement in a galvanic cell-type and is known for its mid-values capacitance in the micro-farad range. The storage energy is expressed by $\Delta G = -Q\Delta V$ and is normally limited by intrinsic variables of the chemical redox reactions in the cell i.e. electrode materials and its electro-activity, mass of reactants and electric characteristics of the electrochemical cell (*224*). The third group of capacitors are called electrochemical supercapacitors after the patent of Graig (*226*) or ultracapacitors which can accept charges per potential difference in the farads to tens and even hundreds of farads. This last type of capacitors is used in energy storage applications with functionalities and performances between the regular dielectric capacitors and the rechargeable batteries. Indeed, from Conway and Gileadi (*227*), with this electrochemical process there are chemical modifications of the electrode-reacting material under the action of faradic or redox charge transfer. However, it exhibits properties more close to the ones of a capacitor rather than a galvanic cell arrangement, when it is subject to charge-discharge tests. Supercapacitors can be classified into two types depending on their charge-storage mechanism (*156*, *224*, *227–231*):

- the electric double-layer capacitor, which is based on the capacitance due to the very small distance between the charges on the electrode surface and their opposite charges provided by the electrolyte, which is a true capacitive non-faradic process, and
- the pseudocapacitor, which is based on the charge-transfer generated by the close-to-reversible faradic reactions at the electrode surface and formed during the anodic polarization. The origin of the capacitance in this case is faradic and not electrostatic.

The capacitance of a supercapacitor is therefore the sum of the double-layer capacitance C_{dl} with the pseudocapacitance C_{Φ} (*231*):

$$C_{sc} = C_{dl} + C_{\Phi} \tag{8.1}$$

with $C_{dl} = \epsilon A/4\pi d$, ϵ being the dielectric constant of the double-layer, A the surface of the electrode and d thickness of the double-layer. C_{Φ}, however, is due the redox reaction (*228*):

$$\mathrm{Ox_{ad}} + \mathrm{ze^-} \longrightarrow \mathrm{Red_{ad}} \tag{8.2}$$

Supercapacitors are the subject of intense research activity, as they exhibit higher power density and higher degree of reversibility i.e. longer cycle life when compared to batteries and higher energy density when compared to electric double-layer capacitors (*227*, *229*–*231*). Figure 8.1 shows Ragone plot of power density versus the energy density of the major categories of energy storage devices: conventional capacitors (CC), supercapacitors (SC), batteries and fuel cells. The main criteria supercapacitor materials should ensure are stability, high life cycle and high electroactive surface area. RuO_2 and IrO_2 are known for higher specific capacitances per unit mass of several hundreds of farads per gram. For example, Kim et al. have reported 620 F/g of composites of carbon nanotube with RuO_2 nanoparticles

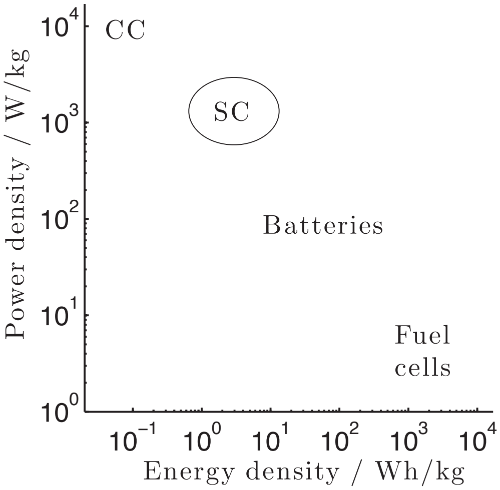

Figure 8.1.: Ragone plot of usual energy storage devices. CC refers to conventional capacitors and SC to supercapacitors.

synthesized by microwave-polyol (*232*), while Zheng et al. reported values as high as 720 F/g for IrO_2 prepared by the sol-gel technique (*233*). Due to the rarity and high cost of these noble metals, alternative solutions based on oxides of more abundant and less expensive materials such as nickel, cobalt and manganese are under extensive investigations (*229*, *230*, *234*–*238*). Carbon-based materials and conductive polymers have also promising features for energy storage applications (*239*–*242*). Table 8.1 gives some selected examples of the most used electrode materials as well as their working conditions and reported specific capacitances values.

8.2. Materials and Experimental Procedures

The synthesis of nickel oxide nanoparticles by electrochemical discharges and their subsequent characterizations are the same as detailed in Section 6.3: two electrodes of nickel in a solution of 2 M H_2SO_4 + 0.5 M of ethanol + 2.5 mg/ml of PVP40 under a constant terminal voltage. The preparation of electrodes for electrochemical

Table 8.1.: Specific capacitance of some electrode materials.

Materials	**Working conditions**	**c_{sc} / F.g^{-1}**
NiO nanoparticles (*176*)	0 – 0.5 V in 1 M KOH	370
NiO_x xerogels (*237*)	0 – 0.6 V in 7 M KOH	696
β-$Ni(OH)_2$ nanoparticles (*230*)	0 – 0.55 V in 1 M KOH	740
$Ni(OH)_2$ film (*229*)	0 – 0.65 V in 0.5 M KOH	578
MnO_2 film (*234*)	-0.2 – 0.75 V in 0.1 M Na_2SO_4	698
Co_3O_4 aerogels (*236*)	-0.1 – 0.55 V 1 M NaOH	623
Activated carbon (AC) (*239*)	0 – 1.5 V in 1 M $EMImBF_4$	48
Graphite (*240*)	0 – 3 V in 1 M Et_4NBF_4 + propylene carbonate	12
Poly(3-methylthiophene)/AC (*241*)	1.5 – 3.6 V in $PYR_{14}TFSI$	15
Polypyrrole/AC (*242*)	0 – 0.9 V in 6 M KOH	588

measurement is done by depositing 20 *μ*l from the ethanol solution, in which the nanoparticles are conserved, onto the cross section of the graphite electrode freshly polished and washed with DI water (*22*, *23*, *161*, *236*). It is then dried for 5 min in the oven preset at 70 °C. All of the potentiometric experiments are conducted at room temperature with the Amel Electrochemistry's potentiostat model 7050 in

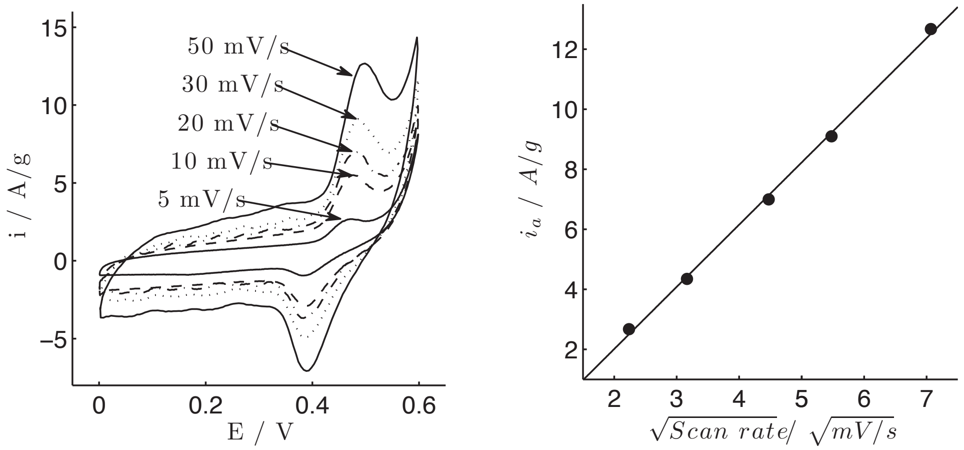

(a) Cyclic voltammograms.

(b) Anodic peak vs. square root of scan rate.

Figure 8.2.: Cyclic voltammograms (8.2(a)) and evolution of anodic peak with the square root of the the scan rate (8.2(b)) of NiO nanoparticles synthesized with Ni cathode vs. Ni anode in 2 M H_2SO_4 + 0.5 M Et + 2.5 mg/ml of PVP40 at 36 V 3 hours and deposited on carbon graphite electrode.

a multi-neck round-bottom flask with Pt as counter electrode and Ag/AgCl/KCl (saturated) as reference electrode.

8.3. Results and Discussion

8.3.1. Cyclic voltammetry

The cyclic voltammograms of the prepared electrodes are performed in the potential range 0 to 0.6 V vs. Ag/AgCl in 1 M of KOH at the scan rates 5, 10, 20, 30 and 50 mV/s. Figure 8.2(a) illustrates the voltammograms of nickel oxide prepared by electrochemical discharges in acidic medium at 36 V and deposited on graphite electrode for the different set scan rates. The y-axis shows the current density per unit mass of the synthesized products weighted with a quartz crystal microbalance. The shown voltammograms are the last ones of series of cycling where the electrochemical responses of the electrodes are stable and do not change subsequently from one cycle to another. The stabilization of the electrode behavior is usually achieved after some 8 to 10 cycles.

The voltammograms are different from the rectangular one specific for the electric double-layer capacitance, and they also conserve their shapes with the variation of scan rates which are typical characteristics of pseudocapcitance behavior (*158*, *159*, *176*). However, there is a slight positive shift of the anodic peak with the increase of the scan rate which indicates some irreversibility in the system (*224*, *243*). In the used alkaline solution, the following surface faradic charge-discharge reactions occur (*159*, *176*, *177*, *244*, *245*):

$$\mathrm{NiO} + \mathrm{zOH}^- \underset{\text{discharge}}{\overset{\text{charge}}{\rightleftharpoons}} \mathrm{zNiOOH} + (1 - \mathrm{z})\mathrm{NiO} + \mathrm{ze}^- \tag{8.3}$$

where $0 < z < 1$ is the fraction of available sites at NiO for the reaction with OH^- ions. Additionally, the quasi-perfect linearity of current density of the anodic peak versus the square root of the scan rate illustrated in Figure 8.2(b) confirms that the redox reactions are diffusion-limited according to Randle-Sevcik equation, and also the pseudocapcitance behavior of the electrode materials (*157*, *176*, *229*, *246*). Randle-Sevcik equation for one electron transfer writes (*247*):

$$i_a = 2.69 \times 10^5 AC\sqrt{Ds_r} \tag{8.4}$$

with i_a being the current of the anodic peak, A the electro-active surface area, C the concentration of the electro-active species, D the diffusion coefficient and s_r the scan rate.

The average capacitance per unit mass or the specific capacitance, c_{sc}, of the nano-materials can be estimated from the cyclic voltammograms by graphically integrating the total charge over the voltage window according to the Equation

(*176*, *230*, *242*, *245*):

$$c_{sc} = \frac{1}{m s_r (V_a - V_c)} \int_{V_c}^{V_a} I dV \tag{8.5}$$

where m is the mass of deposited NiO nanoparticles, s_r the voltage scan rate, and $V_a - V_c = \Delta V$ the potential window. The specific current densities of the anodic peaks in Figure 8.2(b) are 12.7, 9.1, 7.0, 4.4 and 2.7 A/g for the scan rates of 50, 30, 20, 10, and 5 mV/s respectively, to which correspond the calculated specific capacities of 134, 155, 182, 199 and 233 F/g. The inverse variation of c_{sc} with the scan rate is due to the fact that smaller fractions of the OH^- ions will reach the electro-active nickel oxides at deposited the electrode surface. In the contrary, with low voltammetric scan rates, higher fraction of OH^- involved in Reaction 8.3 will have favorable conditions to access the NiO nanoparticles and thus more of the available capacitance (*248*). These values are in agreement to what is reported in the literature (*177*, *243*, *246*, *249*) which are still far, however, from the theoretical value of the capacitance of NiO: approximatively 2570 F/g within the 0 to 0.5 potential difference window (*250*–*252*).

8.3.2. Chronopotentiometry

Chronopotentiometry is the galvanostatic constant current charge-discharge measurements at the electrode surface. Charge-discharge curves at different current densities of NiO nanoparticles synthesized at 36 V in acidic medium are illustrated in Figure 8.3. The potential window is set to 0 to 0.5 V versus the Ag/AgCl reference electrode in 1 M KOH. For the different imposed current densities, the charging step shows two stages: the first linear one corresponds to the oxidation of the NiO whereas the second one corresponds to the charging process itself. On the other hand, the discharging curve shows first a sharp negatively slopped segment due to the potential drop and a second part related to the capacitive behavior. The

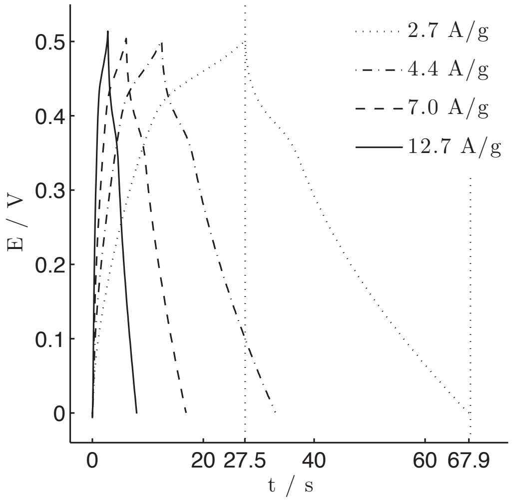

Figure 8.3.: Constant current charge-discharge response of NiO nanoparticles synthesized with Ni cathode vs. Ni anode in 2 M H_2SO_4 + 0.5 M Et + 2.5 mg/ml of PVP40 at 36 V during 3 hours and deposited on carbon graphite electrode.

chronopotentiometry measurements of Figure 8.3 is typical for pseudocapacitive types of materials (*156*, *157*, *229*, *243*, *244*, *246*, *249–252*).

The specific capacitance is calculated from the discharge curves as follows (*176*, *230*, *242*, *245*):

$$c_{sc} = \frac{I\Delta t}{m\Delta V} \tag{8.6}$$

where I is the applied current, Δt the discharge time, m the mass of deposited NiO nanoparticles and ΔV the potential window. For example, at I/m = 2.7 A/g, $c_{sc} = 2.7 \times (67.9 - 27.5)/0.5 = 218.16$ F/g. For the same current densities of 12.7, 9.1, 7.0, 4.4 and 2.7 A/g, the specific capacitances from the charge-discharges curves are found to be 131, 143, 169, 182 and 218 F/g respectively. Again, because of the diffusion-controlled redox reaction between the OH^- ions and the NiO nanoparticles, the specific capacitance increases for lower charge-discharge rates. The values of c_{sc} are in line with the ones estimated from the cyclic voltammetry measurements.

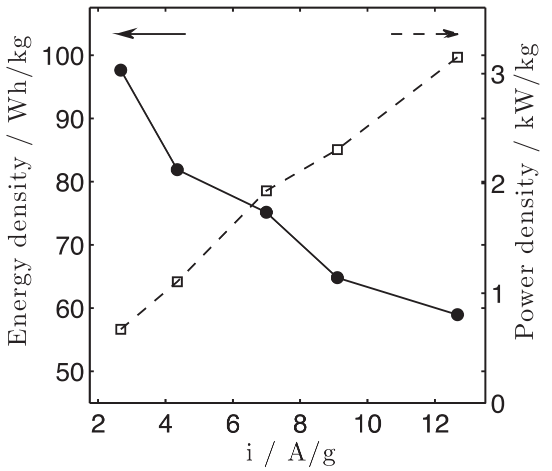

Figure 8.4.: Energy density and power density vs. current density of NiO synthesized with Ni cathode vs. Ni anode in 2 M H_2SO_4 + 0.5 M Et + 2.5 mg/ml of PVP40 at 36 V during 3 hours and deposited on carbon graphite electrode.

8.3.3. Ragone plots

As stated previously in Section 8.1, some of the features of supercapacitors is that they exhibit high energy density when compared to double-layer capacitors and high power density when compared to regular batteries. The energy density d_e of the electrode materials, calculated as $d_e = c_{sc}(\Delta V)^2/2$ and the power density d_p, calculated as $d_p = d_e/\Delta t$ from the chronopotentiometric results are plotted in Figure 8.4 with respect to the applied current density. The energy density of double layer capacitors is in the order of 0.1 Wh/kg or less, while the power densities of batteries are in the range of 50 to 200 W/kg (*228*). The performance of the synthetized NiO nanomaterials by electrochemical discharges are clearly those of a supercapacitor with energy densities varying from almost 100 to 54 Wh/kg at current densities varying from 2.7 to 12.7 A/g, which are over two orders of magnitude greater than those of double layer capacitors. The power density increases from 0.7 to over 3.1 kW/kg within the same current density window while the NiMH or the NiCd battery are able to handle power just in the range 0.01 to 0.2 kW/kg (*228*).

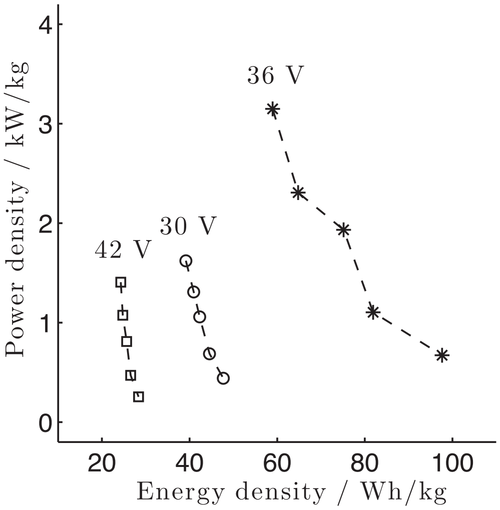

Figure 8.5.: Ragone plot of NiO synthesized with Ni cathode vs. Ni anode in 2 M H_2SO_4 + 0.5 M Et + 2.5 mg/ml of PVP40 at 30, 36 and 42 V during 3 hours and deposited on carbon graphite electrode.

Following the same procedure for the calculation of the specific capacitances from the charge-discharge plots, the power and energy performances of nickel oxides nanoparticles prepared by electrochemical discharges in acidic medium at 30, 36 and 42 V are compared. Ragone plot of the analyzed NiO nano-materials are shown in Figure 8.5. It is clear that the particles synthesized at 36 V exhibit the highest energy and power densities when compared to the ones synthesized at 30 V and 42 V. Therefore, they are more advantageous for energy storage applications. From the SEM characterizations of Table 6.2, the average size is found to be 70, 91 and 107 nm for the NiO nanoparticles synthesized at 36, 30 and 42 V respectively. Additionally, the samples synthesized at 42 V (Figure 6.10(b)) are severely sintered and agglomerated, when compared to the two other samples (Figures 6.6(a) and 6.10(a)), due to the high local discharge activity at these electric conditions. The OH^- ions during the redox Reaction 8.3 have better accessibility to the NiO for small size and less agglomerated particles, due to their high active surfaces, than the larger ones. This is in good line with the obtained results in Ragone plots of Figure 8.5.

8.4. Conclusion

Nickel oxide prepared by electrochemical discharges in acidic medium are suitable to be used as supercapacitors for energy storage purposes. The pseudocapacitance of the nickel oxide products is based on faradic charge-transfer reaction with the hydroxide ions and is dependent to the accessibility of OH^-. Therefore, smaller size and well dispersed particle can increase the reaction mechanism for higher specific capacitance values. For example, NiO particles manufactured by electrochemical discharges and with average size of 70 nm are able to store charges with high specific capacitance of 218 F/g. Their correspondent energy and power densities are as high as 98.1 Wh/kg and 0.7 kW/kg. On the other hand, NiO manufactured at 30 V with average size of 91 nm have a specific capacitance of 106 F/g with $d_e = 47.7$ Wh/kg and $d_p = 0.44$ kW/kg. Larger particles manufactured at 42 V and with average size of 107 nm still exhibit pseudocapacitance behavior with $c_s = 63$ F/g, $d_e = 28.4$ Wh/kg and $d_p = 0.25$ kW/kg but less than the smaller ones.

Part III.

Conclusions & Outlook

Chapter 9

Conclusions

The electrochemical discharge phenomenon is a complex high current-density electrolysis precess. The main objectives of this work were to compact the description of the system to some measurable thermodynamic variables. Additionally, as its stability issues are crucial for its various applications, both the mechanics and dynamics of the repeatability of the process constituted a task for this project. In a second part, the application of the phenomenon to the synthesis of nano-sized materials has been investigated in detail, including a comprehensive methodology for the manufacturing process as well as an overall picture of the microscopic mechanisms behind it.

9.1. Highlights

The key achievements and contributions of this work are enumerated as follows:

1. The application of nonequilibrium thermodynamics to the electrochemical discharges condenses its macroscopic description to an entropy flow as:

$$\mathbf{J}_s = \frac{1}{T}\left(\mathbf{J}_q - \sum_{k=1}^{n} \mu_k \mathbf{J}_k\right)$$

and an entropy production as a sum-product of the conjugated thermal and electrochemical fluxes and forces as:

$$\sigma = -\frac{\nabla T}{T^2} \cdot \mathbf{J}'_q - \frac{1}{T}\sum_{k=1}^{n} \mathbf{J}_k \cdot \nabla \mu_{k,T} - \frac{1}{T}\mathbf{i} \cdot \nabla U - \frac{1}{T} P \nabla \cdot \mathbf{v}$$

These relations express the essential thermodynamic features of the process which are sufficient to its analysis.

2. From the excess entropy production, with $-\delta S^2$ as a Lyapunov function, the discharge regime is always stable beyond the inflection mid-point voltage of the current-voltage characteristics.

3. The wavelet-based algorithm, with the discrete Meyer wavelet as mother function, is a strong and reliable signal processing tool designed and tested for the quantification of the gas film time parameters. By ensuring the non-alteration of the time and frequency features of the original signal, it is verified experimentally that the electrochemical discharge phenomenon is increasingly stable with the temperature and the applied terminal voltage, as predicted by the nonequilibrium thermodynamics analysis. The gas film life-time is at least ten times greater than the gas film formation-time, which is in the order of the millisecond.

4. Nickel oxide/hydroxide and platinum nanoparticles are successfully manufactured by electrochemical discharges in aqueous solutions of H_2SO_4, ethanol and PVP as well as in alkaline solutions of KOH at different electric conditions and time of experiments.

5. The crystal composition of nickel-based nano-materials prepared by electrochemical discharges are in connection with their stable phases in the Ni−O−H

Pourbaix diagram: NiO nanoparticles are obtained in an acidic medium while Ni, NiO and β-Ni(OH)$_2$ are obtained in an alkaline environment.

6. Two mechanisms explain the synthesis process of nano-sized materials by electrochemical discharges: *i)* the reduction to zero-valent atoms by the reducing species generated from the radiation of water such as the hydrated electron, the H$^{\cdot}$ radical and secondary formed radicals, and *ii)* the electrode material sputtering by positively charges ions. The colloidal clusters are then subject to nucleation process and crystal growth in the bulk solution.

7. The recommended operating procedure to manufacture nano-sized materials by electrochemical discharges is as follows:

   a) design an electrochemical solution while taking into account:
      - the origin and stability of metal precursors,
      - a minimum electric conductivity suitable for the discharges regime, and
      - the stability of the manufactured products.

   b) set the operating electric conditions knowing that one has to make a compromise between the size distribution and the yield as follows:
      i. for particles of smaller sizes and narrower dispersity:
         - set the electric conditions at which the the gas film is more stable and the discharges are globally comparable in intensities,
         - minimize the overall current density by adjusting the penetration depth of the cathode,
         - operate the electrochemical discharges for shorter times.

      ii. for a higher yield:

  - increase the overall current density,
  - operate at larger voltages
  - operate the electrochemical discharges for longer times,

8. Nickel oxide nanoparticles synthesized by electrochemical discharges exhibit very suitable characteristics for energy storage applications. The maximum achieved capacitance surpasses the 200 F/g for nanoparticles of NiO of 70 nm size. Their mass density of energy from 60 to close to 100 Wh/kg and of power in the range of 1 to 3 kW/kg are those of high performance supercapacitors.

9.2. Outlook

There still remain many unresolved questions regarding the electrochemical discharges. For example, by analyzing the gas film with naked eye when the applied terminal voltage is downgraded to values very close to the discharges threshold, it is observed that its physical boundaries are more and more perturbed. In other words, a formed gas film will be followed by a discharge activity during a short period of time, and then will be broken so that the system starts to operate under conventional electrolysis, and reformed again and so on. Of course the same occurs at higher voltages but not as easily observed. Knowing that the phenomenon is globally stable and that the discharges are self-sustainable by an avalanche process, the factor behind this instability is probably related to the production and emission of electrons from the cathode. If so, is there a critical ionization value of the gas film? What are the dynamics of the local parameters stabilizing or destabilizing the discharge regime? What are their time scales or in other words, are they slow or fast stabilizing processes? Can we extend the nonequilibrium thermodynamics description of the phenomenon by implementing fluctuation theory into the entropy

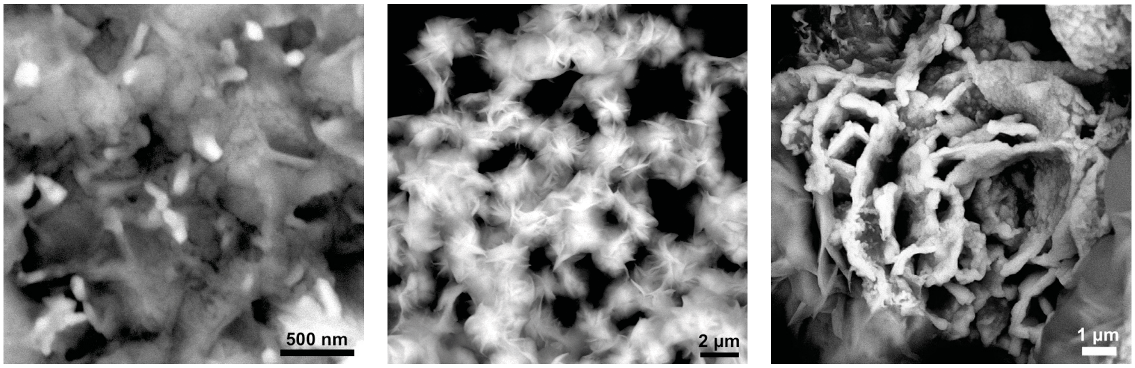

(a) (b) (c)

Figure 9.1.: SEM micrograph of nickel-based nanoflowers prepared in 100 ml aqueous solution of H_3PO_4 30 % wt. + 0.5 M Et + 2.5 mg/ml of PVP40 discharged at 60 V during 3 hours.

production? In short, many other issues are still unclear about the physics of the electrochemical discharges.

On another note, it has been shown throughout this work that the phenomenon has great potential when applied to nanotechnology. However, there are still many questions to be accounted for. For example, how to further enhance its productivity and efficiency? Are its power density and high energy inputs capable of reshaping the manufactured particles? For example, Figure 9.1 shows electron micrographs of nano-flowers of nickel-based materials synthesized in an aqueous solution of H_3PO_4 30 % wt. + 0.5 M Et + 2.5 mg/ml of PVP40 at 60 V. Why does the process give such structures? Also, how effective would the technique be if one synthesizes and deposits nanoparticles in online machined micro-fluidic channels by SACE technology which is based on the same operating parameters shown in this work? Certainly, the doors are still open for many further investigations.

Part IV.

Appendices

Appendix A

Computation of Gas Film Life-time and Building-time

The random variables T_f representing the gas film-life time and T_g representing the gas film building-time in the denoised current signal are computed as follows (*88*). Let n_{GF} denotes the number of the gas film formations in the time-current signal after denoising by wavelet transformation. The time intervals between two successive gas film formation peaks , $GF^{(i)}$ and $GF^{(i+1)}$, allow the analysis in appropriate variable width windows w_i ($i = 1, 2, \cdots, n_{GF-1}$) to be performed. For each window w_i, a matrix $M_i(2, k_i)$ is built containing in one row all the times of the local minima and in second row their corresponding current values. The first column corresponds to the end of the previous gas film formation and the last one corresponds to the beginning of the next one.

Considering the two successive time windows w_i and $w_{(i+1)}$ and their corresponding constructed matrices $M_i(2, m)$ and $M_{i+1}(2, n)$, T_{f_i}, the gas film life time numbered (i), is calculated as follows:

$$T_{f_i} = M_i(1, m) - M_i(1, 1) \tag{A.1}$$

and, $T_{g_{i+1}}$, the gas film formation time numbered $(i + 1)$ is calculated by:

$$T_{g_{i+1}} = M_{i+1}(1, 1) - M_i(1, m) \tag{A.2}$$

Appendix B

Nucleation Rate

This Appendix aims to show the derivation of the rate of nucleation J_0. The master equation is derived by considering the following simplifying assumptions (*209*, *210*):

1. The cluster geometrical shape does not change with time.
2. The system supersaturation value $\Delta\mu$ between the solid and liquid phase does not change with time.
3. The nucleation process is a series of reversible binary reactions, analogous to the birth-death process (*220*, *221*) and can be written (*210*):

$$\begin{aligned}
\mathrm{M_1} + \mathrm{M_1} &\underset{k_2^-}{\overset{k_1^+}{\rightleftharpoons}} \mathrm{M_2} \\
\mathrm{M_2} + \mathrm{M_1} &\underset{k_3^-}{\overset{k_2^+}{\rightleftharpoons}} \mathrm{M_3} \\
&\cdots \\
\mathrm{M_{n-1}} + \mathrm{M_1} &\underset{k_n^-}{\overset{k_{n-1}^+}{\rightleftharpoons}} \mathrm{M_n} \\
\mathrm{M_n} + \mathrm{M_1} &\underset{k_{n+1}^-}{\overset{k_n^+}{\rightleftharpoons}} \mathrm{M_{n+1}} \\
&\cdots
\end{aligned}$$

where k_n^+ and k_n^- ($n = 1, 2, \ldots$) represent, respectively, the constant rates of reactions of attachment and detachment of a single atom $\mathrm{M_1}$ to and from the cluster composed of *n* atoms M_1 and denoted by M_n. This can schematized as follows:

$$M_{n-1} \xleftarrow[-M_1,\ k_n^-\ \text{(detachment)}]{} M_n \xrightarrow{+M_1,\ k_n^+\ \text{(attachment)}} M_{n+1} \tag{B.1}$$

4. Many-body collisions are not considered.

From kinetic chemistry, the time change of the concentration of the nuclei formed by *n* times M_1 can be expressed as follows:

$$\frac{d[M_n]}{dt} = \left(k_{n-1}^+[M_{n-1}] - k_n^-[M_n]\right) - \left(k_n^+[M_n] - k_{n+1}^-[M_{n+1}]\right) \tag{B.2}$$

which in terms of net fluxes can be rewritten as:

$$\frac{d[M_n]}{dt} = J_n - J_{n+1} \tag{B.3}$$

In the time-independent state, $d[M_n]/dt = 0$, which defines the steady state rate or also known as the frequency of formation of clusters of a given class *n* (*210*):

$$J_n = J_{n+1} = J_0 \tag{B.4}$$

The result expressed by Equation B.4 gives the system of algebraic equations:

$$J_0 = k_{n-1}^+[M_{n-1}] - k_n^-[M_n], \quad \forall n = 2, 3, \cdots, N \tag{B.5}$$

with $[M_N] = 0$ as stated in the second assumption of this analysis. Summing up the Equations B.5 and with further analytical arrangements (see Ball et al. (*215*)), one obtains the general expression for the rate of nucleation at steady state situations as follows:

$$J_0 = [M_1]\left[\sum_{n=1}^{N-1}\left(\frac{1}{k_n^+}\frac{k_2^-k_3^-\cdots k_n^-}{k_1^+k_2^+\cdots k_{n-1}^+}\right)\right]^{-1} \tag{B.6}$$

At equilibrium state, in absence of molecular flux ($J_0 = 0$ in Equation B.5), one obtains the equation of detailed balance as:

$$k^+_{n-1}[\mathrm{M}_{\mathrm{n-1}}]_{eq} = k^-_n[\mathrm{M}_{\mathrm{n}}]_{eq} \iff \frac{[\mathrm{M}_{\mathrm{n}}]_{eq}}{[\mathrm{M}_{\mathrm{n-1}}]_{eq}} = \frac{k^+_{n-1}}{k^-_n} \tag{B.7}$$

from which it can be written that:

$$\prod_{i=2}^{n}\left(\frac{[\mathrm{M}_{\mathrm{i}}]_{eq}}{[\mathrm{M}_{\mathrm{i-1}}]_{eq}}\right) = \frac{[\mathrm{M}_{\mathrm{n}}]_{eq}}{[\mathrm{M}_{1}]_{eq}} = \prod_{i=2}^{n}\left(\frac{k^-_i}{k^+_{i-1}}\right)^{-1} \tag{B.8}$$

From kinetic theory, the growth of a cluster from the class $n-1$ to the class n obeys the reaction rate (*210*):

$$k^+_{n-1} = \frac{P}{\sqrt{2\pi m k_B T}} a_{n-1} \tag{B.9}$$

which is equal to the product of the density of number of collisions $P/\sqrt{2\pi m k_B T}$ by the surface area of the cluster, a_{n-1}, with P the vapor pressure of the system. An analogous expression can be written for rate constant of the detachment reaction so that a cluster from class n goes back to class $n-1$ (*210*):

$$k^-_n = \frac{P_n}{\sqrt{2\pi m k_B T}} a_{n-1} \tag{B.10}$$

with P_n the equilibrium vapor pressure of cluster of class n. Applying the Thomson-Gibbs Equation leads to the expression:

$$\frac{k^-_n}{k^+_{n-1}} = \frac{P_n}{P} = \exp\left[\frac{2\gamma v_l}{k_B T}\left(\frac{1}{r_n} - \frac{1}{r_c}\right)\right] \tag{B.11}$$

from which the following relation can be obtained :

$$\prod_{i=2}^{n}\left(\frac{k_i^-}{k_{i-1}^+}\right) = \exp\left[\frac{2\gamma}{k_B T}\left(\frac{4\pi v_l^2}{3}\right)^{1/3}\sum_n\left(\frac{1}{n^{1/3}} - \frac{1}{n_c^{1/3}}\right)\right] \tag{B.12}$$

where $nv_l = 4\pi r^3/3$ has been used. Equation B.12 contains a summation part which can be converted to simple integration by calling the capillary approximation where the number of atoms or molecules n_c in the critical size nucleus is much more grater that unit. After integration one obtains the following Relation (*210*):

$$\prod_{i=2}^{n}\left(\frac{k_i^-}{k_{i-1}^+}\right) = \exp\left\{\frac{\gamma}{k_B T}\left(\frac{4\pi v_l^2 n_c^2}{3}\right)^{1/3}\left[3\left(\frac{n}{n_c}\right)^{2/3} - 2\left(\frac{n}{n_c}\right)\right]\right\} \tag{B.13}$$

By substituting the expression of supersaturation $\Delta\mu$ from Equation 7.22 into Equation 7.21 and considering the expressing of Gibbs free energy function of the critical radius, one obtains:

$$\Delta G(r) = \Delta G_c\left[3\left(\frac{r}{r_c}\right)^3 - 2\left(\frac{r}{r_c}\right)^3\right] \tag{B.14}$$

$$\Delta G(n) = \Delta G_c\left[3\left(\frac{n}{n_c}\right)^{2/3} - 2\left(\frac{n}{n_c}\right)\right] \tag{B.15}$$

Equation B.13 can be rewritten then as:

$$\prod_{i=2}^{n}\left(\frac{k_i^-}{k_{i-1}^+}\right) = \exp\left(\frac{\Delta G(n)}{k_B T}\right) \tag{B.16}$$

Finally, based on Equation B.8, the equilibrium concentration of clusters from the class n is expressed by the remarkable thermodynamical form:

$$[\mathrm{M_n}]_{eq} = [\mathrm{M_1}]_{eq}\exp\left(-\frac{\Delta G(n)}{k_B T}\right) \tag{B.17}$$

The integration of the sum product of Equation B.6 can be found in Markov (*210*) and the rate of nucleation at steady state situations can be written as follows:

$$J_0 = [\mathrm{M}_1]k^+ \left(\frac{\Delta G_c}{3\pi k_B T n_c^2}\right)^{1/2} \exp\left(-\frac{\Delta G_c}{k_B T}\right) \tag{B.18}$$

which can be rewritten as the product of the frequency of attachment of atoms or molecules to the critical nucleus k^+ by the Zeldovich factor Γ and by the equilibrium concentration of the critical nucleus $[\mathrm{M_n}]_{eq}$ (*209*, *210*):

$$J_0 = k^+ \Gamma [\mathrm{M_n}]_{eq} \tag{B.19}$$

For colloidal solutions, the flux of atoms to the critical nucleus is determined by the diffusion and the frequency parameter k^+ is proportional to the concentration C of the particles present in the solution, which give the expression:

$$k^+ = 4\pi r_c^2 C \nu \lambda \exp\left(\frac{-\Delta G_{des}}{k_B T}\right) \tag{B.20}$$

with ν a frequency factor, λ the mean free path of particles in the solution and ΔG_{des} the energy of desolvation. J_0 is then written:

$$J_0 = 4\pi r_c^2 C \nu \lambda \exp\left(\frac{-\Delta G_{des}}{k_B T}\right) \Gamma \exp\left(\frac{-\Delta G_c}{k_B T}\right) \tag{B.21}$$

Bibliography

1. Wüthrich, R.; Fascio, V. Machining of non-conducting materials using electrochemical discharge phenomenon – an overview. *International Journal of Machine Tools and Manufacture* **2005**, *45*, 1095–1108.

2. Wüthrich, R. *Micromachining using electrochemical discharge phenomenon: fundamentals and applications of spark assisted chemical engraving*; Micro & nano technologies; William Andrew, 2009.

3. Wüthrich, R.; Mandin, P. Electrochemical discharges–Discovery and early applications. *Electrochimica Acta* **2009**, *54*, 4031 – 4035.

4. Gao, J.; Wang, X.; Hu, Z.; Hou, J.; Lu, Q. A review on chemical effects in aqueous solution induced by plasma with glow discharge. *Plasma Science and Technology* **2001**, *3*, 765–774.

5. Yerokhin, A.; Nie, X.; Leyland, A.; Matthews, A.; Dowey, S. Plasma electrolysis for surface engineering. *Surface and Coatings Technology* **1999**, *122*, 73–93.

6. Toriyabe, Y.; Watanabe, S.; Yatsu, S.; Shibayama, T.; Mizuno, T. Controlled formation of metallic nanoballs during plasma electrolysis. *Applied Physics Letters* **2007**, *91*, 041501–041503.

7. Kawamura, H.; Moritani, K.; lto, Y. Discharge electrolysis in molten chloride: formation of fine silver particles. *Plasmas & Ions* **1998**, *1*, 29–36.

8. Oishi, T.; Kawamura, H.; Ito, Y. Formation and size control of titanium particles by cathode discharge electrolysis of molten chloride. *Journal of Applied Electrochemistry* **2002**, *32*, 819–824.

9. Lal, A.; Bleuler, H.; Wüthrich, R. Fabrication of metallic nanoparticles by electrochemical discharges. *Electrochemistry Communications* **2008**, *10*, 488–491.

10. Fizeau, H.; Foucault, L. Recherches sur l'intensité de la lumière émise par le charbon dans l'expérience de Davy. *Comptes Rendus des Séances de l'Académie des Sciences* **1844**, *18*, 746–754.

11. Glansdorff, P.; Prigogine, I. *Thermodynamic theory of structure, stability and fluctuations*; New York: Wiley-Interscience, 1971.

12. Fizeau, H.; Foucault, L. Recherches sur l'intensité de la lumière émise par le charbon dans l'expérience de Davy. *Comptes Rendus des Séances de l'Académie des Sciences* **1844**, *18*, 860–862.

13. Hoho, P. Phénomène calorifique produit par le courant électrique au contact d'un solide et un liquide. *La Lumière Electrique* **1894**, *52*, 113–120.

14. Hoho, P. Phénomène calorifique produit par le courant électrique au contact d'un solide et un liquide. *La Lumière Electrique* **1894**, *52*, 165–169.

15. Bagard, H. A. Wehnelt. – Ein elektrolytischer stromunterbrecher (Interrupteur électrolytique) – Wied. Ann., LXVIII, p.233-272. *Journal de Physique Théorique Appliquée* **1899**, *8*, 438–444.

16. Kellogg, H. H. Anode effect in aqueous electrolysis. *Journal of The Electrochemical Society* **1950**, *97*, 133–142.

17. Hickling, A.; Newns, G. R. Glow-discharge electrolysis. Part V. The contact glow-discharge electrolysis of liquid ammonia. *Journal of the Chemical Society* **1961**, 5186–5191.

18. Hickling, A.; Ingram, M. Contact glow-discharge electrolysis. *Transactions of the Faraday Society* **1964**, *60*, 783–793.

19. Sengupta, S. K.; Singh, O. P. Contact glow discharge electrolysis: a study of its chemical yields in aqueous inert-type electrolytes. *Journal of Electroanalytical Chemistry* **1994**, *369*, 113–120.

20. Gao, J.; Wang, A.; Fu, Y.; Wu, J.; Ma, D.; Guo, X.; Li, Y.; Yang, W. Analysis of energetic species caused by contact glow discharge electrolysis in aqueous solution. *Plasma Science and Technology* **2008**, *10*, 30–38.

21. Wüthrich, R.; Allagui, A. Building micro and nanosystems with electrochemical discharges. *Electrochimica Acta* **2010**, *55*, 8189 – 8196.

22. Wüthrich, R.; Allagui, A. In *Electrolysis: Theory, Types and Applications*; Kuai, S., Meng, J., Eds.; Nova Science Publishers Inc., 2010; Chapter 5.

23. Wüthrich, R.; Allagui, A. *Electrolysis in aqueous solutions under extreme current densities – fundaments and applications of electrochemical discharge phenomenon*; Nova Science Publishers Inc., 2010.

24. Rudorff, D. Principles and applications of spark machining. *Proceedings of the Institution of Mechanical Engineers* **1957**, *17*, 495–507.

25. Kurafuji, H.; Suda, H. Electrical discharge drilling of glass. *Annals of the CIRP* **1968**, *16*, 415–419.

26. Harada, K.; Igari, S.; Takasaki, M.; Shimoyama, A. Reductive fixation of molecular nitrogen by glow discharge against water. *Journal of the Chemical Society, Chemical Communications* **1986**, *17*, 1384–1385.

27. Harada, K.; Iwasaki, T. Syntheses of amino acids from aliphatic carboxylic acid by glow discharge electrolysis. *Nature* **1974**, *250*, 426–428.

28. Harada, K.; Suzuki, S. Formation of amino acids from elemental carbon by contact glow discharge electrolysis. *Nature* **1977**, *266*, 275–276.

29. Efrima, S. Morphology of quasi-two-dimensional electrodeposits - a generalized Wagner number. *Langmuir* **1997**, *13*, 3550–3556.

30. Mandin, P.; Wüthrich, R.; Roustan, H. Polarization curves for an alkaline water electrolysis at a small pin vertical electrode to produce hydrogen. *AIChE Journal* **2010**, *56*, 2446–2454.

31. Roussenq, J.; Clerc, J.; Giraud, G.; Guyon, E.; Ottavi, H. Size dependence of the percolation threshold of square and triangular network. *Journal de Physique Lettres* **1976**, *37*, 99–101.

32. Wüthrich, R.; Bleuler, H. A model for electrode effects using percolation theory. *Electrochimica Acta* **2004**, *49*, 1547–1554.

33. Azumi, K.; Mizuno, T.; Akimoto, T.; Ohmori, T. Light emission from Pt during high-voltage cathodic polarization. *Journal of The Electrochemical Society* **1999**, *146*, 3374–3377.

34. Gao, J.; Liu, Y.; Yang, W.; Pu, L.; Yu, J.; Lu, Q. Oxidative degradation of phenol in aqueous electrolyte induced by plasma from a direct glow discharge. *Plasma Sources Science and Technology* **2003**, *12*, 533.

35. Hickling, A.; Ingram, M. D. Glow-discharge electrolysis. *Journal of Electroanalytical Chemistry* **1964**, *8*, 65–81.

36. Allen, A. O. Radiation chemistry of aqueous solutions. *The Journal of Physical and Colloid Chemistry* **1948**, *52*, 479–490.

37. Allen, A. O. Radiation chemistry. *Annual Review of Physical Chemistry* **1952**, *3*, 57–80.

38. Allen, A. O. The yields of free H and OH in the irradiation of water. *Radiation Research* **1954**, *1*, 85–96.

39. Allen, A. O. Radiation yields and reactions in dilute inorganic solutions. *Radiation Research Supplement* **1964**, *4*, 54–73.

40. Fricke, H.; Thomas, J. K. Pulsed electron beam kinetics. *Radiation Research Supplement* **1964**, *4*, 35–53.

41. Dewhurst, H. A.; Samuel, A. H.; Magee, J. L. A theoretical survey of the radiation chemistry of water and aqueous solutions. *Radiation Research* **1954**, *1*, 62–84.

42. Hummel, A.; Allen, A. O.; Freddie H. Watson, J. Ionization of Liquids by Radiation. II. Dependence of the Zero-Field Ion Yield on Temperature and Dielectric Constant. *The Journal of Chemical Physics* **1966**, *44*, 3431–3436.

43. Allen, A. O. *Yields of free ions formed in liquids by radiation*; NSRDS-NBS 57; U.S. Dept. of Commerce, National Bureau of Standards, 1976.

44. Guilpin, C.; Garbarz-Olivier, J. Analyse de la lumière émise aux électrodes pendant les effects d'électrode, dans des solutions aqueuses d'électrolyte. *Spectrochimica Acta Part B: Atomic Spectroscopy* **1977**, *32*, 155–164.

45. Yerokhin, A. L.; Snizhko, L. O.; Gurevina, N. L.; Leyland, A.; Pilkington, A.; Matthews, A. Discharge characterization in plasma electrolytic oxidation of aluminium. *Journal of Physics D: Applied Physics* **2003**, *36*, 2110–2120.

46. Valognes, J. C.; Bardet, J. P.; Mergault, P. Contribution à l'étude des effets d'électrode. *Spectrochimica Acta Part B: Atomic Spectroscopy* **1987**, *42*, 445–458.

47. Kobayashi, K.; Tomita, Y.; Sanmyo, M. Electrochemical generation of hot plasma by pulsed discharge in an electrolyte. *The Journal of Physical Chemistry B* **2000**, *104*, 6318–6326.

48. Maximov, A.; Khlustova, A. Optical emission from plasma discharge in electrochemical systems applied for modification of material surfaces. *Surface and Coatings Technology* **2007**, *201*, 8782–8788.

49. Maximov, A. I.; Khlyustova, A. V. Physical chemistry of plasma-solution systems. *High Energy Chemistry* **2009**, *43*, 149–155.

50. Griem, H. R. High-density corrections in plasma spectroscopy. *Physical Review* **1962**, *128*, 997.

51. Denaro, A. A model for glow discharge electrolysis. *Electrochimica Acta* **1975**, *20*, 669 – 673.

52. Mazza, B.; Pedeferri, P.; Re, G. Hydrodynamic instabilities in electrolytic gas evolution. *Electrochimica Acta* **1978**, *23*, 87–93.

53. Vogt, H. Heat transfer at gas evolving electrodes. *Electrochimica Acta* **1978**, *23*, 1019–1022.

54. Vogt, H. Mechanisms of mass transfer of dissolved gas from a gas-evolving electrode and their effect on mass transfer coefficient and concentration overpotential. *Journal of Applied Electrochemistry* **1989**, *19*, 713–719.

55. Wüthrich, R.; Fascio, V.; Bleuler, H. A stochastic model for electrode effects. *Electrochimica Acta* **2004**, *49*, 4005–4010.

56. Sengupta, S. K.; Srivastava, A. K.; Singh, R. Contact glow discharge electrolysis: a study on its origin in the light of the theory of hydrodynamic instabilities in local solvent vaporisation by Joule heating during electrolysis. *Journal of Electroanalytical Chemistry* **1997**, *427*, 23 – 27.

57. Vogt, H.; Aras, O.; Balzer, R. J. The limits of the analogy between boiling and gas evolution at electrodes. *International Journal of Heat and Mass Transfer* **2004**, *47*, 787 – 795.

58. Nicolis, G.; Prigogine, I. *Self-organization in non-equilibrium systems*; New York: Wiley-Interscience, 1977.

59. Glansdorff, P.; Prigogine, I. Sur les propriétés différentielles de la production d'entropie. *Physica* **1954**, *20*, 773–780.

60. Prigogine, I. Time, structure, and fluctuations. *Science* **1978**, *201*, 777–785.

61. Glansdorff, P.; Nicolis, G.; Prigogine, I. The thermodynamic stability theory of non-equilibrium states. *Proceedings of the National Academy of Sciences of the United States of America* **1974**, *71*, 197–199.

62. de Groot, S.; Mazur, P. *Non-equilibrium thermodynamics*; New York: Interscience Publishers, 1962.

63. Wilf, H. *Mathematics for the physical sciences*; New York and London: John Wiley and Sons Inc., 1962.

64. Kondepudi, D.; Prigogine, I. *Modern thermodynamics, from heat engine to dissipative structures*; New York: Wiley-Interscience, 1999.

65. Planck, M. *Treatise on thermodynamics*, 3rd ed.; Courier Dover Publications, 1945.

66. Fermi, E. *Thermodynamics*; Dover Publications, 1956.

67. Griffiths, D. *Introduction to electrodynamics*, 3rd ed.; New Jersey: Prentice Hall, 1999.

68. Allagui, A.; Wüthrich, R. *Contact glow discharge electrolysis: a far from thermodynamic equilibrium system*; 60th Meeting of the International Society of Electrochemistry: Beijing, China, 2009.

69. Chapman, S.; Cowling, T. *The mathematical theory of non-uniform gases*, 2nd ed.; New York: Cambridge University Press, 1953.

70. Kjelstrup, S.; Bedeaux, D. *Non-equilibrium thermodynamics of heterogeneous systems*; Advances in Statistical Mechanics; World Scientific Publishing, 2008; Vol. 16.

71. Onsager, L. Reciprocal relations in irreversible processes. I. *Physical Review* **1931**, *37*, 405–426.

72. Onsager, L. Reciprocal relations in irreversible processes. II. *Physical Review* **1931**, *38*, 2265–2279.

73. Hangos, K.; Bokor, J.; Szederkényi, G. *Analysis and control of nonlinear process systems*; Springer, 2004.

74. Khalil, H. *Nonlinear systems*, 2nd ed.; Prentice Hall, 1996.

75. Orlov, Y. *Discontinuous systems: Lyapunov analysis and robust synthesis under uncertainty conditions*; Springer, 2008.

76. Allagui, A.; Wüthrich, R. *The gas film on the onset of non-equilibrium plasma electrolysis*; 1st Concordia University Multiphysics Workshop: Montreal, Canada, 2009.
77. Allagui, A.; Wüthrich, R. *On the modelling of non-equilibrium plasma electrolysis:gas film stability*; 8th World Congress of Chemical Engineering: Montreal, Canada, 2009.
78. Wüthrich, R.; Baranova, E. A.; Bleuler, H.; Comninellis, C. A phenomenological model for macroscopic deactivation of surface processes. *Electrochemistry Communications* **2004**, *6*, 1199–1205.
79. Fowler, R. H.; Nordheim, L. Electron emission in intense electric fields. *Proceedings of the Royal Society of London. Series A* **1928**, *119*, 173–181.
80. Stern, T. E.; Gossling, B. S.; Fowler, R. H. Further studies in the emission of electrons from cold metals. *Proceedings of the Royal Society of London. Series A* **1929**, *124*, 699–723.
81. Murphy, E. L.; Good, R. H. Thermionic emission, field emission, and the transition region. *Physical Review* **1956**, *102*, 1464–1473.
82. Wüthrich, R.; Hof, L. The gas film in spark assisted chemical engraving (SACE) – a key element for micro-machining applications. *International Journal of Machine Tools and Manufacture* **2006**, *46*, 828–835.
83. Wüthrich, R. Spark assisted chemical engraving - a stochastic modelling approach. Ph.D. thesis, Ecole Polytechnique Fédérale de Lausanne, 2003.
84. Wüthrich, R.; Spaelter, U.; Bleuler, H. The current signal in spark-assisted chemical engraving (SACE): what does it tell us? *Journal of Micromechanics and Microengineering* **2006**, *16*, 779–785.

85. Daubechies, I. *Ten lectures on wavelets*; SIAM, 1992.

86. Holschneider, M. *Wavelets: an analysis tool*; Oxford Mathematical Monographs; Oxford University Press, 1995.

87. Mallat, S. *A wavelet tour of signal processing*; Academic Press, 1998.

88. Allagui, A.; Wüthrich, R. Gas film formation time and gas film life time during electrochemical discharge phenomenon. *Electrochimica Acta* **2009**, *54*, 5336–5343.

89. Vogt, H.; Thonstad, J. Review of the causes of anode effects. *Aluminium* **2003**, *77*, 98–102.

90. Feynman, R. There's plenty of room at the bottom [data storage]. *Journal of Microelectromechanical Systems* **1992**, *1*, 60–66.

91. Halperin, W. P. Quantum size effects in metal particles. *Reviews of Modern Physics* **1986**, *58*, 533–606.

92. Kubo, R.; Kawabata, A.; Kobayashi, S. Electronic properties of small particles. *Annual Review of Materials Science* **1984**, *14*, 49–66.

93. Bansmann, J. et al. Magnetic and structural properties of isolated and assembled clusters. *Surface Science Reports* **2005**, *56*, 189–275.

94. Stewart, G. R. Size effects in the electronic heat capacity of small platinum particles embedded in silica. *Physical Review B* **1977**, *15*, 1143–1150.

95. Bradley, J. In *Cluster and colloids. From theory to applications*; Schmid, G., Ed.; VCH, Weinheim, 1994; Chapter 6.

96. Haruta, M.; Yamada, N.; Kobayashi, T.; Iijima, S. Gold catalysts prepared by coprecipitation for low-temperature oxidation of hydrogen and of carbon monoxide. *Journal of Catalysis* **1989**, *115*, 301 – 309.

97. Haruta, M. Size- and support-dependency in the catalysis of gold. *Catalysis Today* **1997**, *36*, 153 – 166.

98. Buffat, P.; Borel, J.-P. Size effect on the melting temperature of gold particles. *Physical Review A* **1976**, *13*, 2287–2298.

99. Shvartsburg, A. A.; Jarrold, M. F. Solid clusters above the bulk melting point. *Physical Review Letters* **2000**, *85*, 2530–2532.

100. Mulvaney, P. Not all that's gold glitter. *MRS Bulletin* **2001**, *26*, 1009–1014.

101. Ung, T.; Liz-Marzán, L.; Mulvaney, P. Gold nanoparticle thin film. *Colloids and Surfaces A* **2002**, *202*, 119–126.

102. McCarter, S.; Harris, C. *Nanotechnology now used in nearly 500 everyday products*; 2007.

103. Chin, N. *Nanotech-enabled Consumer Products Top the 1,000 Mark*; 2009.

104. 2010; `http://www.nanotechproject.org/`.

105. Pérez, J.; Bax, L.; Escolano, C. *Roadmap report on nanoparticles*; 2005.

106. Nagarajan, R. In *Nanoparticles: synthesis, stabilization, passivation, and functionalization*; Nagarajan, R., Hatton, T. A., Eds.; American Chemical Society, 2008; Chapter 1.

107. Reetz, M. T.; Helbig, W. Size-selective synthesis of nanostructured transition metal clusters. *Journal of the American Chemical Society* **1994**, *116*, 7401–7402.

108. Reetz, M. T.; Helbig, W.; Quaiser, S. A. Electrochemical preparation of nanostructural bimetallic clusters. *Chemistry of Materials* **1995**, *7*, 2227–2228.

109. Reetz, M. T.; Winter, M.; Breinbauer, R.; Thurn-Albrecht, T.; Vogel, W. Size-selective electrochemical preparation of surfactant-stabilized Pd-, Ni- and Pt/Pd colloids. *Chemistry* **2001**, *7*, 1084–1094.

110. Yu, Y.-Y.; Chang, S.-S.; Lee, C.-L.; Wang, C. R. C. Gold nanorods: electrochemical synthesis and optical properties. *The Journal of Physical Chemistry B* **1997**, *101*, 6661–6664.

111. Mohamed, M. B.; Ismail, K. Z.; Link, S.; El-Sayed, M. A. Thermal reshaping of gold nanorods in micelles. *The Journal of Physical Chemistry B* **1998**, *102*, 9370–9374.

112. Yin, B.; Ma, H.; Wang, S.; Chen, S. Electrochemical synthesis of silver nanoparticles under protection of poly(N-vinylpyrrolidone). *The Journal of Physical Chemistry B* **2003**, *107*, 8898–8904.

113. Ma, H.; Yin, B.; Wang, S.; Jiao, Y.; Pan, W.; Huang, S.; Chen, S.; Meng, F. Synthesis of silver and gold nanoparticles by a novel electrochemical method. *ChemPhysChem* **2004**, *5*, 68–75.

114. Tian, N.; Zhou, Z.-Y.; Sun, S.-G.; Ding, Y.; Wang, Z. L. Synthesis of tetrahexahedral platinum nanocrystals with high-index facets and high electro-oxidation activity. *Science* **2007**, *316*, 732–735.

115. Fujita, H.; Izawa, M.; Yamakazi, H. γ-Ray induced formation of gold sol from chloroauric acid solution. *Nature* **1962**, *196*, 666–667.

116. Marignier, J. L.; Belloni, J.; Delcourt, M. O.; Chevalier, J. P. Microaggregates of non-noble metals and bimetallic alloys prepared by radiation-induced reduction. *Nature* **1985**, *317*, 344–345.

117. Remita, H.; Khatouri, J.; Tréguer, M.; Amblard, J.; Belloni, J. Silver-palladium alloyed clusters synthesized by radiolysis. *Zeitschrift fur Physik D Atoms Molecules Clusters* **1997**, *40*, 127–130.

118. Sankaran, R. M.; Holunga, D.; Flagan, R. C.; Giapis, K. P. Synthesis of blue luminescent Si nanoparticles using atmospheric-pressure microdischarges. *Nano Letters* **2005**, *5*, 537–541.

119. Burakov, V.; Savastenko, N.; Tarasenko, N.; Nevar, E. Synthesis of nanoparticles using a pulsed electrical discharge in a liquid. *Journal of Applied Spectroscopy* **2008**, *75*, 114–124.

120. Lung, J.-K.; Huang, J.-C.; Tien, D.-C.; Liao, C.-Y.; Tseng, K.-H.; Tsung, T.-T.; Kao, W.-S.; Tsai, T.-H.; Jwo, C.-S.; Lin, H.-M.; Stobinski, L. Preparation of gold nanoparticles by arc discharge in water. *Journal of Alloys and Compounds* **2007**, *434-435*, 655 – 658.

121. Schwarz, J. A.; Contescu, C.; Contescu, A. Methods for preparation of catalytic materials. *Chemical Reviews* **1995**, *95*, 477–510.

122. Kung, H. H.; Ko, E. I. Preparation of oxide catalysts and catalyst supports – a review of recent advances. *The Chemical Engineering Journal and the Biochemical Engineering Journal* **1996**, *64*, 203 – 214.

123. Hench, L. L.; West, J. K. The sol-gel process. *Chemical Reviews* **1990**, *90*, 33–72.

124. Chen, D.-H.; He, X.-R. Synthesis of nickel ferrite nanoparticles by sol-gel method. *Materials Research Bulletin* **2001**, *36*, 1369 – 1377.

125. Bharathi, S.; Fishelson, N.; Lev, O. Direct synthesis and characterization of gold and other noble metal nanodispersions in sol-gel-derived organically modified silicates. *Langmuir* **1999**, *15*, 1929–1937.

126. Turkevich, J.; Stevenson, P. C.; Hillier, J. A study of the nucleation and growth processes in the synthesis of colloidal gold. *Discussions of the Faraday Society* **1951**, *11*, 55–75.

127. Enüstün, B. V.; Turkevich, J. Coagulation of colloidal gold. *Journal of the American Chemical Society* **1963**, *85*, 3317–3328.

128. Hirai, H.; Nakao, Y.; Toshima, N. Preparation of colloidal transition metals in polymers by reduction with alcohols or ethers. *Journal of Macromolecular Science, Part A: Pure and Applied Chemistry* **1979**, *13*, 727 – 750.

129. Boutonnet, M.; Kizling, J.; Stenius, P.; Maire, G. The Preparation of monodisperse colloidal metal particles from microemulsions. *Colloids and Surfaces* **1982**, *5*, 209–225.

130. Danielsson, I.; Lindman, B. The definition of microemulsion. *Colloids and Surfaces* **1981**, *3*, 391 – 392.

131. López-Quintela, M.; Rivas, J.; Blanco, M.; Tojo, C. In *Nanoscale Materials*; Liz-Marzán, L. M., Kamat, P. V., Eds.; Springer US, 2004; pp 135–155.

132. Chen, D.-H.; Wu, S.-H. Synthesis of nickel nanoparticles in water-in-oil microemulsions. *Chemistry of Materials* **2000**, *12*, 1354–1360.

133. Pillai, V.; Kumar, P.; Multani, M. S.; Shah, D. O. Structure and magnetic properties of nanoparticles of barium ferrite synthesized using microemulsion processing. *Colloids and Surfaces A: Physicochemical and Engineering Aspects* **1993**, *80*, 69 – 75.

134. Touroude, R.; Girard, P.; Maire, G.; Kizling, J.; Boutonnet-Kizling, M.; Stenius, P. Preparation of colloidal platinum/palladium alloy particles from non-ionic microemulsions: Characterization and catalytic behaviour. *Colloids and Surfaces* **1992**, *67*, 9 – 19.

135. Wu, M.-L.; Chen, D.-H.; Huang, T.-C. Preparation of Pd/Pt bimetallic nanoparticles in water/AOT/isooctane microemulsions. *Journal of Colloid and Interface Science* **2001**, *243*, 102 – 108.

136. Sangregorio, C.; Galeotti, M.; Bardi, U.; Baglioni, P. Synthesis of Cu_3Au nanocluster alloy in reverse micelles. *Langmuir* **1996**, *12*, 5800–5802.

137. Zhang, D.-E.; Ni, X.-M.; Zhang, X.-J.; Zheng, H.-G. Synthesis and characterization of Ni-Co needle-like alloys in water-in-oil microemulsion. *Journal of Magnetism and Magnetic Materials* **2006**, *302*, 290 – 293.

138. Suslick, K. S. The chemical effects of ultrasound. *Scientific American* **1989**, *260*, 80–86.

139. Suslick, K. Sonochemistry. *Science* **1990**, *247*, 1439–1445.

140. Suslick, K.; Price, G. Applications of ultrasound to materials chemistry. *Annual Review of Materials Science* **1999**, *29*, 295–326.

141. Flint, E. B.; Suslick, K. S. The temperature of cavitation. *Science* **1991**, *253*, 1397–1399.

142. Putterman, S. Sonoluminescence: sound into light. *Scientific American* **1995**, *272*, 46–51.

143. Suslick, K. S.; Didenko, Y.; Fang, M. M.; Hyeon, T.; Kolbeck, K. J.; McNamara, W. B.; Mdleleni, M. M.; Wong, M. Acoustic cavitation and its chemical

consequences. *Philosophical Transactions of the Royal Society of London. Series A* **1999**, *357*, 335–353.

144. Suslick, K.; Choe, S.; Cichowlas, A.; Grinstaff, M. Sonochemical synthesis of amorphous iron. *Nature* **1991**, *353*, 414–416.

145. Suslick, K. S.; Fang, M.; Hyeon, T. Sonochemical synthesis of iron colloids. *Journal of the American Chemical Society* **1996**, *118*, 11960–11961.

146. Hyeon, T.; Fang, M.; Suslick, K. S. Nanostructured molybdenum carbide: sonochemical synthesis and catalytic properties. *Journal of the American Chemical Society* **1996**, *118*, 5492–5493.

147. Okitsu, K.; Bandow, H.; Maeda, Y. Sonochemical preparation of ultrafine palladium particles. *Chemistry of Materials* **1996**, *8*, 315–317.

148. Liu, K.; Grinstaff, M.; Jiang, J.; Suslick, K.; Swartz, H.; Wang, W. In vivo measurement of oxygen concentration using sonochemically synthesized microspheres. *Biophysical Journal* **1994**, *67*, 896–901.

149. Niklasson, G. A.; Granqvist, C. G. Ultrafine nickel particles for photothermal conversion of solar energy. *Journal of Applied Physics* **1979**, *50*, 5500–5505.

150. Setoguchi, T.; Okamoto, K.; Eguchi, K.; Arai, H. Effects of anode material and fuel on anodic reaction of solid oxide fuel cells. *Journal of The Electrochemical Society* **1992**, *139*, 2875–2880.

151. Yoshinaga, M.; Yamamoto, K.; Sato, N.; Aoki, K.; Morikawa, T.; Muramatsu, A. Remarkably enhanced photocatalytic activity by nickel nanoparticle deposition on sulfur-doped titanium dioxide thin film. *Applied Catalysis B: Environmental* **2009**, *87*, 239–244.

152. Lee, S. G.; Lee, S.; Lee, H.-I. Photocatalytic production of hydrogen from aqueous solution containing CN- as a hole scavenger. *Applied Catalysis A: General* **2001**, *207*, 173 – 181.

153. Escudero, M.; Nóvoa, X.; Rodrigo, T.; Daza, L. Study of a Li–Ni oxide mixture as a novel cathode for molten carbonate fuel cells by electrochemical impedance spectroscopy. *Journal of Applied Electrochemistry* **2002**, *32*, 929–936.

154. Ando, M.; Kobayashi, T.; Haruta, M. Enhancement in the optical CO sensitivity of NiO film by the deposition of ultrafine gold particles. *Journal of the Chemical Society, Faraday Transactions* **1994**, *90*, 1011–1013.

155. Ando, M.; Zehetner, J.; Kobayashi, T.; Haruta, M. Large optical CO sensitivity of NO2-pretreated Au-NiO composite films. *Sensors and Actuators B: Chemical* **1996**, *36*, 513 – 516.

156. Liang, K.; Chen, A.; He, L.; Wang, W. Nickel oxide as an electrode material for supercapacitors. *Journal of Materials Science & Technology* **2002**, *18*, 383–384.

157. Fu, G. R.; Hu, Z. A.; Xie, L. J.; Jin, X. Q.; Xie, Y. L.; Wang, Y. X.; Zhang, Z. Y.; Yang, Y. Y.; Wu, H. Y. Electrodeposition of nickel hydroxide films on nickel foil and its electrochemical performances for supercapacitor. *International Journal of Electrochemical Science* **2009**, *4*, 1052 – 1062.

158. Chang, J.; Park, M.; Ham, D.; Ogale, S.; Mane, R. S.; Han, S.-H. Liquid-phase synthesized mesoporous electrochemical supercapacitors of nickel hydroxide. *Electrochimica Acta* **2008**, *53*, 5016 – 5021.

159. zhen Zheng, Y.; yang Ding, H.; lin Zhang, M. Preparation and electrochemical properties of nickel oxide as a supercapacitor electrode material. *Materials Research Bulletin* **2009**, *44*, 403 – 407.

160. Lu, Q.; Lattanzi, M. W.; Chen, Y.; Kou, X.; Li, W.; Fan, X.; Unruh, K. M.; Chen, J. G.; Xiao, J. Q. Supercapacitor electrodes with high-energy and power densities prepared from monolithic NiO/Ni nanocomposites. *Angewandte Chemie International Edition* **2011**, *50*.

161. Allagui, A.; Wüthrich, R.; Baranova, E. *Copper and nickel nanoparticles: synthesis by electrochemical discharges*; Microsystems and Nanoelectronics Research Conference: Ottawa, Canada, 2008; pp 65–68.

162. Allagui, A.; Wüthrich, R. *Nanostructures fabriquées par décharges électrochimiques*; 78e Congrés de l'Acfas: Montreal, Canada, 2010.

163. Itagakia, M.; Nakazawaa, H.; Watanabea, K.; Nodab, K. Study of dissolution mechanisms of nickel in sulfuric acid solution by electrochemical quartz crystal microbalance. *Corrosion Science* **1997**, *39*, 901–911.

164. Sato, N.; Kudo, K. An ellipsometric study of anodic passivation of nickel in borate buffer solution. *Electrochimica Acta* **1974**, *19*, 461 – 470.

165. Ohtsuka, T.; Heusler, K. Potential-dependent properties of the passivating film on nickel in sulphuric acid solution from multiple-angle-of-incidence reflectivity measurements. *Journal of Electroanalytical Chemistry* **1979**, *102*, 175 – 187.

166. Bockris, J.; Drazic, D.; Despic, A. The electrode kinetics of the deposition and dissolution of iron. *Electrochimica Acta* **1961**, *4*, 325–361.

167. Sato, N.; Okamoto, G. Anodic passivation of nickel in sulfuric acid solutions. *Journal of The Electrochemical Society* **1963**, *110*, 605–614.

168. Sato, N.; Okamoto, G. Kinetics of the anodic dissolution of nickel in sulfuric acid solutions. *Journal of The Electrochemical Society* **1964**, *111*, 897–903.

169. National Institute of Advanced Industrial Science and Technology, Research Center for Deep Geological Environments, *Atlas of Eh-pH diagrams: Intercomparison of thermodynamic databases - Geological Survey of Japan Open File Report No.419*; 2005.

170. Beverskog, B.; Puigdomenech, I. Revised Pourbaix diagrams for nickel at 25-300 °C. *Corrosion Science* **1997**, *39*, 969 – 980.

171. Buxton, G. V. In *Radiation chemistry: from basics to applications in material and life sciences*; Spotheim-Maurizot, M., Douki, T., Mostafavi, M., Belloni, J., Eds.; L'Actualité Chimique Livres; EDP Sciences, 2008; Chapter 1.

172. Mazumder, S.; Bhagwat, K. V.; Sequeira, A. Estimation of particle size distribution in multiple small-angle scattering. *Journal of Physics: Condensed Matter* **1995**, *7*, 9737.

173. Fang, Z.; Patterson, B. R.; Jr., M. E. T. Modeling particle size distributions by the Weibull distribution function. *Materials Characterization* **1993**, *31*, 177 – 182.

174. Calandra, P.; Longo, A.; Turco Liveri, V. Synthesis of ultra-small ZnS nanoparticles by solid–solid reaction in the confined space of AOT reversed micelles. *The Journal of Physical Chemistry B* **2003**, *107*, 25–30.

175. Baranova, E.; Amir, T.; Mercier, P.; Patarachao, B.; Wang, D.; Le Page, Y. Single-step polyol synthesis of alloy Pt7Sn3 versus bi-phase Pt/SnOx nano-catalysts of controlled size for ethanol electro-oxidation. *Journal of Applied Electrochemistry* **2010**, *40*, 1767–1777.

176. Meher, S. K.; Justin, P.; Ranga Rao, G. Microwave-mediated synthesis for improved morphology and pseudocapacitance performance of nickel oxide. *ACS Applied Materials & Interfaces* **2011**, *3*, 2063–2073.

177. Xing, W.; Li, F.; feng Yan, Z.; Lu, G. Q. Synthesis and electrochemical properties of mesoporous nickel oxide. *Journal of Power Sources* **2004**, *134*, 324 – 330.

178. Mousa, M.; Allagui, A.; Ng, H. D.; Wuthrich, R. The effect of thermal conductivity of the tool electrode in spark-assisted chemical engraving gravity-feed micro-drilling. *Journal of Micromechanics and Microengineering* **2009**, *19*, 015010.

179. Hart, E. J.; Boag, J. W. Absorption spectrum of the hydrated electron in water and in aqueous solutions. *Journal of the American Chemical Society* **1962**, *84*, 4090–4095.

180. Walker, D. C. The hydrated electron. *Quarterly Reviews of the Chemical Society* **1967**, *21*, 79–108.

181. Belloni, J.; Remita, H. In *Radiation chemistry: from basics to applications in material and life sciences*; Spotheim-Maurizot, M., Douki, T., Mostafavi, M., Belloni, J., Eds.; L'Actualité Chimique Livres; EDP Sciences, 2008; Chapter 7.

182. Allagui, A.; Wüthrich, R. *Nanomaterials synthesized by electrochemical discharges: qualitative and quantitative performance*; American Physical Society: Dallas, USA, 2011; Vol. 56.

183. Kelm, M.; Lilie, J.; Henglein, A.; Janata, E. Pulse radiolytic study of nickel(1+) ion. Nickel-carbon bond formation. *The Journal of Physical Chemistry* **1974**, *78*, 882–887.

184. Goodman, J.; Hickling, A.; Schofield, B. The yield of hydrated electrons in glow-discharge electrolysis. *Journal of Electroanalytical Chemistry and Interfacial Electrochemistry* **1973**, *48*, 319 – 322.

185. Hart, E. J.; Fielden, E. M.; Anbar, M. Reactions of carbonylic compounds with hydrated electrons. *The Journal of Physical Chemistry* **1967**, *71*, 3993–3998.

186. Wolff, R. K.; Bronskill, M. J.; Hunt, J. W. Picosecond pulse radiolysis studies. II. Reactions of electrons with concentrated scavengers. *The Journal of Chemical Physics* **1970**, *53*, 4211–4215.

187. Grove, W. R. On the electro-chemical polarity of gases. *Philosophical Transactions of the Royal Society of London* **1852**, *142*, 87–101.

188. Kingdon, K. H.; Langmuir, I. The removal of thorium from the surface of a thoriated tungsten filament by positive ion bombardment. *Physical Review* **1923**, *22*, 148–160.

189. Thompson, M. W. The contribution of collision cascades to sputtering and radiation damage. *Philosophical Transactions: Mathematical, Physical and Engineering Sciences* **2004**, *362*, 5–28.

190. Langmuir, I. The constitution and fundamental properties of solids and liquids. Part I. Solids. *Journal of the American Chemical Society* **1916**, *38*, 2221–2295.

191. Wehner, G. K. Momentum transfer in sputtering by ion bombardment. *Journal of Applied Physics* **1954**, *25*, 270–271.

192. Henschke, E. B. New collision theory of cathode sputtering of metals at low ion energies. *Physical Review* **1957**, *106*, 737–753.

193. Silsbee, R. H. Focusing in collision problems in solids. *Journal of Applied Physics* **1957**, *28*, 1246–1250.

194. Harrison, D. E. Theory of the sputtering process. *Physical Review* **1956**, *102*, 1473–1480.

195. Falcone, G. Ejection process in collisional sputtering. *Physical Review B* **1986**, *33*, 5054–5056.

196. Sigmund, P. Theory of sputtering. I. Sputtering yield of amorphous and polycrystalline targets. *Physical Review* **1969**, *184*, 383–416.

197. Baragiola, R. A. Sputtering: survey of observations and derived principles. *Philosophical Transactions: Mathematical, Physical and Engineering Sciences* **2004**, *362*, 29–53.

198. Facsko, S.; Dekorsy, T.; Koerdt, C.; Trappe, C.; Kurz, H.; Vogt, A.; Hartnagel, H. L. Formation of ordered nanoscale semiconductor dots by ion sputtering. *Science* **1999**, *285*, 1551–1553.

199. Colligon, J. S. Ion-assisted sputter deposition. *Philosophical Transactions: Mathematical, Physical and Engineering Sciences* **2004**, *362*, 103–116.

200. Betz, G.; Husinsky, W. Modelling of cluster emission from metal surfaces under ion impact. *Philosophical Transactions: Mathematical, Physical and Engineering Sciences* **2004**, *362*, 177–194.

201. Mohri, N.; Takezawa, H.; Furutani, K.; Ito, Y.; Sata, T. A new process of additive and removal machining by EDM with a thin electrode. *CIRP Annals - Manufacturing Technology* **2000**, *49*, 123–126.

202. Tanabe, R.; Ito, Y.; Takezawa, H.; Mohri, N. Time-resolved observation of electrode shape of a thin electrode in high-current, single discharge. *Journal of Materials Processing Technology* **2004**, *149*, 226–231.

203. Kurita, T.; Chikamori, K.; Kubota, S.; Hattori, M. A study of three-dimensional shape machining with an electrochemical micromachning system. *International Journal of Machine Tools and Manufacture* **2006**, *46*, 1311–1318.

204. Zheng, Z.-P.; Su, H.-C.; Huang, F.-Y.; Yan, B.-H. The tool geometrical shape and pulse-off time of pulse voltage effects in a Pyrex glass electrochemical

discharge microdrilling process. *Journal of Micromechanics and Microengineering* **2007**, *17*, 265–272.

205. Massey, H.; Burhop, E. *Electronic and ionic impact phenomena*; Clarendon Press, Oxford, 1952.

206. Becker, K. H.; Schoenbach, K. H.; Eden, J. G. Microplasmas and applications. *Journal of Physics D: Applied Physics* **2006**, *39*, R55.

207. LaMer, V. K.; Dinegar, R. H. Theory, production and mechanism of formation of monodispersed hydrosols. *Journal of the American Chemical Society* **1950**, *72*, 4847–4854.

208. Guggenheim, E. A. *Thermodynamics*; Amsterdam: North-Holland, 1967.

209. Kashchiev, D. *Nucleation: Basic Theory with Applications*; Oxford: Butterworth-Heinemann, 2000.

210. Markov, I. V. *Crystal growth for beginners*, 2nd ed.; Singapore: World Scientific Publishing, 2003.

211. Peng, Z.; Yang, H. Designer platinum nanoparticles: Control of shape, composition in alloy, nanostructure and electrocatalytic property. *Nano Today* **2009**, *4*, 143 – 164.

212. Voorhees, P. W. The theory of Ostwald ripening. *Journal of Statistical Physics* **1985**, *38*, 231–252.

213. Frenkel, J. A general theory of heterophase fluctuations and pretransition phenomena. *The Journal of Chemical Physics* **1939**, *7*, 538–547.

214. Dreyer, W.; Duderstadt, F. On the Becker/Döring theory of nucleation of liquid droplets in solids. *Journal of Statistical Physics* **2006**, *123*, 55–87.

215. Ball, J. M.; Carr, J.; Penrose, O. The Becker-Döring cluster equations: Basic properties and asymptotic behaviour of solutions. *Communications in Mathematical Physics* **1986**, *104*, 657–692.

216. Denaro, A.; Hough, K. Polymerisation by glow discharge electrolysis. *Electrochimica Acta* **1973**, *18*, 863 – 868.

217. Fricke, H.; Hart, E. J.; Smith, H. P. Chemical reactions of organic compounds with X-Ray activated water. *The Journal of Chemical Physics* **1938**, *6*, 229–240.

218. Baxendale, J. H. Effects of oxygen and pH in the radiation chemistry of aqueous solutions. *Radiation Research Supplement* **1964**, *4*, 114–138.

219. Baxendale, J. H.; Dixon, R. S. *Proceedings of the Chemical Society*; American Chemical Society, 1963; pp 148–149.

220. Gardiner, C. W. *Handbook of stochastic methods for physics, chemistry and the natural sciences*, 2nd ed.; Berlin: Springer-Verlag, 1985.

221. Stirzaker, D. *Stochastic rocesses and models*; Oxford: Oxford University Press, 2005.

222. LaMer, V. K.; Kenyon, A. S. Kinetics of the formation of monodispersed sulfur sols from thiosulfate and acid. *Journal of Colloid Science* **1947**, *2*, 257–264.

223. Lubitz, W.; Tumas, W. Hydrogen: an overview. *Chemical Reviews* **2007**, *107*, 3900–3903.

224. Conway, B. E. Transition from ”Supercapacitor” to ”Battery” behavior in electrochemical energy storage. *Journal of The Electrochemical Society* **1991**, *138*, 1539–1548.

225. Bagotsky, V. S. *Fundamentals of Electrochemistry*, 2nd ed.; John Wiley & Sons, Inc., 2006.

226. Graig, D. R. Electric energy storage devices. 1985.

227. Conway, B. E.; Gileadi, E. Kinetic theory of pseudo-capacitance and electrode reactions at appreciable surface coverage. *Transactions of the Faraday Society* **1962**, *58*, 2493–2509.

228. Zhang, Y.; Feng, H.; Wu, X.; Wang, L.; Zhang, A.; Xia, T.; Dong, H.; Li, X.; Zhang, L. Progress of electrochemical capacitor electrode materials: A review. *International Journal of Hydrogen Energy* **2009**, *34*, 4889 – 4899.

229. Zhao, D.-D.; Bao, S.-J.; Zhou, W.-J.; Li, H.-L. Preparation of hexagonal nanoporous nickel hydroxide film and its application for electrochemical capacitor. *Electrochemistry Communications* **2007**, *9*, 869 – 874.

230. Aghazadeh, M.; Golikand, A. N.; Ghaemi, M. Synthesis, characterization, and electrochemical properties of ultrafine β-Ni(OH)$_2$ nanoparticles. *International Journal of Hydrogen Energy* **2011**, *36*, 8674 – 8679.

231. Shukla, A.; Sampath, S.; Vijayamohanan, K. Electrochemical supercapacitors: Energy storage beyond batteries. *Current Science* **2000**, *79*, 1656–1661.

232. Kim, J.-Y.; Kim, K.-H.; Park, S.-H.; Kim, K.-B. Microwave-polyol synthesis of nanocrystalline ruthenium oxide nanoparticles on carbon nanotubes for electrochemical capacitors. *Electrochimica Acta* **2010**, *55*, 8056 – 8061.

233. Zheng, J. P.; Cygan, P. J.; Jow, T. R. Hydrous ruthenium oxide as an electrode material for electrochemical capacitors. *Journal of The Electrochemical Society* **1995**, *142*, 2699–2703.

234. Pang, S.-C.; Anderson, M. A.; Chapman, T. W. Novel electrode materials for thin-film ultracapacitors: comparison of electrochemical properties of sol-gel-

derived and electrodeposited manganese dioxide. *Journal of The Electrochemical Society* **2000**, *147*, 444–450.

235. Tao, F.; Gao, C.; Wen, Z.; Wang, Q.; Li, J.; Xu, Z. Cobalt oxide hollow microspheres with micro- and nano-scale composite structure: Fabrication and electrochemical performance. *Journal of Solid State Chemistry* **2009**, *182*, 1055 – 1060.

236. Wei, T.-Y.; Chen, C.-H.; Chang, K.-H.; Lu, S.-Y.; Hu, C.-C. Cobalt oxide aerogels of ideal supercapacitive properties prepared with an epoxide synthetic route. *Chemistry of Materials* **2009**, *21*, 3228–3233.

237. Lin, C.; Ritter, J. A.; Popov, B. N. Characterization of sol-gel-derived cobalt oxide xerogels as electrochemical capacitors. *Journal of The Electrochemical Society* **1998**, *145*, 4097–4103.

238. Lokhande, C.; Dubal, D.; Joo, O.-S. Metal oxide thin film based supercapacitors. *Current Applied Physics* **2011**, *11*, 255 – 270.

239. Wei, L.; Yushin, G. Electrical double layer capacitors with sucrose derived carbon electrodes in ionic liquid electrolytes. *Journal of Power Sources* **2011**, *196*, 4072 – 4079.

240. Gomibuchi, E.; Ichikawa, T.; Kimura, K.; Isobe, S.; Nabeta, K.; Fujii, H. Electrode properties of a double layer capacitor of nano-structured graphite produced by ball milling under a hydrogen atmosphere. *Carbon* **2006**, *44*, 983 – 988.

241. Balducci, A.; Henderson, W. A.; Mastragostino, M.; Passerini, S.; Simon, P.; Soavi, F. Cycling stability of a hybrid activated carbon//poly(3-methylthiophene) supercapacitor with N-butyl-N-methylpyrrolidinium bis(trifluoromethanesulfonyl)imide ionic liquid as electrolyte. *Electrochimica Acta* **2005**, *50*, 2233 – 2237.

242. Kim, J.-H.; Lee, Y.-S.; Sharma, A. K.; Liu, C. G. Polypyrrole/carbon composite electrode for high-power electrochemical capacitors. *Electrochimica Acta* **2006**, *52*, 1727 – 1732.

243. Meher, S. K.; Justin, P.; Rao, G. R. Pine-cone morphology and pseudocapacitive behavior of nanoporous nickel oxide. *Electrochimica Acta* **2010**, *55*, 8388 – 8396.

244. Srinivasan, V.; Weidner, J. W. Studies on the capacitance of nickel oxide films: effect of heating temperature and electrolyte concentration. *Journal of The Electrochemical Society* **2000**, *147*, 880–885.

245. Srinivasan, V.; Weidner, J. W. Capacitance studies of cobalt oxide films formed via electrochemical precipitation. *Journal of Power Sources* **2002**, *108*, 15 – 20.

246. gang Wang, Y.; yao Xia, Y. Electrochemical capacitance characterization of NiO with ordered mesoporous structure synthesized by template SBA-15. *Electrochimica Acta* **2006**, *51*, 3223 – 3227.

247. Randles, J. E. B. A cathode ray polarograph. Part II.-The current-voltage curves. *Transactions of the Faraday Society* **1948**, *44*, 327–338.

248. Pell, W.; Conway, B. Voltammetry at a de Levie brush electrode as a model for electrochemical supercapacitor behaviour. *Journal of Electroanalytical Chemistry* **2001**, *500*, 121 – 133.

249. Justin, P.; Meher, S. K.; Rao, G. R. Tuning of capacitance behavior of NiO using anionic, cationic, and nonionic surfactants by hydrothermal synthesis. *The Journal of Physical Chemistry C* **2010**, *114*, 5203–5210.

250. Xiong, S.; Yuan, C.; Zhang, X.; Qian, Y. Mesoporous NiO with various hierarchical nanostructures by quasi-nanotubes/nanowires/nanorods self-assembly:

controllable preparation and application in supercapacitors. *CrystEngComm* **2011**, *13*, 626–632.

251. Gao, B.; Yuan, C.-z.; Su, L.-h.; Chen, L.; Zhang, X.-g. Nickel oxide coated on ultrasonically pretreated carbon nanotubes for supercapacitor. *Journal of Solid State Electrochemistry* **2009**, *13*, 1251–1257.

252. Yuan, C.; Zhang, X.; Su, L.; Gao, B.; Shen, L. Facile synthesis and self-assembly of hierarchical porous NiO nano/micro spherical superstructures for high performance supercapacitors. *Journal of Materials Chemistry* **2009**, *19*, 5772–5777.

Index

Curriculum Vitæ

Education

2011
- Ph.D Mechanical Engineering, Concordia University, Montreal, Canada
  Dissertation: *On the Electrochemical Discharges for Nanoparticles Synthesis*.

2007
- M.Eng. Mechanical Engineering, Ecole Polytechnique de Nantes, Nantes, France.

Grants & Awards

2011-2012
- Le Fonds québécois de la recherche sur la nature et les technologies (FQRNT) Postdoctoral fellowship, Canada. CA$ 30000 per annum.

2010
- Concurred at Québec Entrepreneurship Contest, Montreal, Canada.

2008 - 2010
- University Mission of Tunisia in North America Award, Montreal, Canada. CA$ 15000.

2009
- Concordia University Multiphysics Workshop Award, Montreal, Canada.
  Best selected paper award in non-linear dynamics, CA$ 200.

- 2009 Concordia University Graduate Seminar in University Teaching Certificate, Montreal, Canada.
- 2008 Microsystems and Nanoelectronics Research Conference (MNRC), Ottawa, Canada.

  Silver leaf certificate for best article, CA$ 600.
- 2008 Concordia University Conference Award Competition for Graduate Students and Postdoctoral Fellows, Montreal, Canada. CA$ 500.
- 2008 - 2009 Concordia University Teaching Fellowship, Montreal, Canada. CA$ 2500.
- 2006 Loire Atlantique Grant for International Internships, Nantes, France. £ 3600.

Publications

Peer-reviewed Articles

Published

1. Anis Allagui and Rolf Wüthrich. The electrochemical discharges for the synthesis of nickel oxide nanoparticles: Characterization and mechanism. *Electrochimica Acta*, In Press, Accepted Manuscript, 2011.
2. Rolf Wüthrich and Anis Allagui. Building micro and nanosystems with electrochemical discharges. *Electrochimica Acta*, 55(27):8189–8196, 2010.
3. Anis Allagui and Rolf Wüthrich. Gas film formation time and gas film life time during electrochemical discharge phenomenon. *Electrochimica Acta*, 54(23):5336–5343, 2009.

4. Malek Mousa, Anis Allagui, H. D. Ng, and Rolf Wüthrich. The effect of thermal conductivity of the tool electrode in spark-assisted chemical engraving gravity-feed micro-drilling. *Journal of Micromechanics and Microengineering*, 19(1):015010–015016, 2009.

In Progress

1. Anis Allagui and Rolf Wüthrich. Capacitance of nickel oxide nanoparticles synthesized with electrochemical discharges. 2011.
2. Anis Allagui and Rolf Wüthrich. Nonequilibrium thermodynamic analysis of the electrochemical discharges phenomenon. 2011.
3. Anis Allagui and Rolf Wüthrich. Phase transition from the conventional to high current density electrolysis. 2012.

Books

1. Rolf Wüthrich and Anis Allagui. *Electrolysis in aqueous solutions under extreme current densities – fundaments and applications of electrochemical discharge phenomenon*. Nova Science Publishers Inc., 2010.

Book Chapters

1. Rolf Wüthrich and Anis Allagui. *Electrolysis: theory, types and applications*, chapter 5. Nova Science Publishers Inc., 2010.

Papers/Abstracts in Refereed Conference Proceedings

1. Maniya Aghasibeig, Anis Allagui, and Rolf Wüthrich. Synthesis of nickel oxide nano-structures by glow discharge electrolysis. In *62th Meeting of the International Society of Electrochemistry*, Niigata, Japan, 2011.

2. Anis Allagui and Rolf Wüthrich. Nanomaterials synthesized by electrochemical discharges: qualitative and quantitative performance. In *American Physical Society March Meeting 2011*, volume 56, Dallas, USA, 2011.

3. Anis Allagui and Rolf Wüthrich. Nanostructures fabriquées par décharges électrochimiques. In *78e Congrés de l'Acfas*, Montreal, Canada, 2010.

4. Anis Allagui and Rolf Wüthrich. On the modelling of non-equilibrium plasma electrolysis:gas film stability. In *8th World Congress of Chemical Engineering*, Montreal, Canada, 2009.

5. Philippe Mandin, Rolf Wüthrich, Anis Allagui, and Hervé Roustan. Two-phase electrolysis process induced flow: from the normal earth gravity to the non gravity experiments. In *8th World Congress of Chemical Engineering*, Montreal, Canada, 2009.

6. Rolf Wüthrich and Anis Allagui. Building micro and nanosystems with electrochemical discharges. In *60th Meeting of the International Society of Electrochemistry*, Beijing, China, 2009.

7. Anis Allagui and Rolf Wüthrich. Contact glow discharge electrolysis: a far from thermodynamic equilibrium system. In *60th Meeting of the International Society of Electrochemistry*, Beijing, China, 2009.

8. Anis Allagui, Rolf Wüthrich, and Elena Baranova. Copper and nickel nanoparticles: synthesis by electrochemical discharges. In *1st Microsystems and Nanoelectronics Research Conference*, pages 65–68, Ottawa, Canada, 2008.

Conference Presentations

1. Rolf Wüthrich, Raisa El-Haddad, Jana Abou Ziki, Anis Allagui and Maniya Aghasibeig. Micro- and nano-structuring by contact glow discharge electrolysis. In *85th ACS Colloid and Surface Science Symposium*, Montreal, Canada, 2011.

2. Marie-Paule Even, Anis Allagui and Rolf Wüthrich. Determination of the electrochemical active surface area of nickel nanoparticles. In *ECS Montreal Student Symposium*, Montreal, Canada, 2011.

3. Anis Allagui and Rolf Wüthrich. Nanostructures fabriquées par décharges électrochimiques. In *78e Congrés de l'Acfas*, Montreal, Canada, 2010.

4. Anis Allagui and Rolf Wüthrich. On the mechanism of nanoparticles synthesis by electrochemical discharges. In *ISE Satellite Student Regional Symposium on Electrochemistry*, Montreal, Canada, 2010.

5. Anis Allagui and Rolf Wüthrich. On the modeling of non-equilibrium plasma electrolysis:gas film stability. In *8th World Congress of Chemical Engineering*, Montreal, Canada, 2009.

6. P. Mandin, Rolf Wüthrich, Anis Allagui, and H. Roustan. Two-phase electrolysis process induced flow: from the normal earth gravity to the non gravity experiments. In *8th World Congress of Chemical Engineering*, Montreal, Canada, 2009.

7. Rolf Wüthrich and Anis Allagui. Building micro and nanosystems with electrochemical discharges. In *60th Meeting of the International Society of Electrochemistry*, Beijing, China, 2009.

8. Anis Allagui and Rolf Wüthrich. Contact glow discharge electrolysis: a far from thermodynamic equilibrium system. In *60th Meeting of the International Society of Electrochemistry*, Beijing, China, 2009.

9. Anis Allagui and Rolf Wüthrich. The gas film on the onset of non-equilibrium plasma electrolysis. In *1st Concordia University Multiphysics Workshop*, Montreal, Canada, 2009.

10. Anis Allagui, Rolf Wüthrich, and Elena Baranova. Copper and nickel nanoparticles: synthesis by electrochemical discharges. In *1st Microsystems and Nanoelectronics Research Conference*, pages 65–68, Ottawa, Canada, 2008.

11. Anis Allagui, Andrew Morisson, T. F. Didar, and Rolf Wüthrich. Electrochemical discharges and applications. In *The TEXPO Research Competition and Exhibition*, Ottawa, Canada, 2008.

12. Mohsen Jalali, Anis Allagui, Tohid F. Didar, and Rolf Wüthrich. Synthesis and characterization of metallic nanoparticles by electrochemical discharges. In *European Society for Precision Engineering and Nanotechnology*, Zurich, Switzerland, 2008.

13. Anis Allagui and Rolf Wüthrich. Nanoparticles synthesis with electrochemical discharges. In *The Electrochemical Society, Inc. Canadian Section*, Montreal, Canada, 2008.

Invited Communications

1. Rolf Wüthrich and Anis Allagui. Building micro and nanosystems with electrochemical discharges. In *60th Meeting of the International Society of Electrochemistry*, Beijing, China, 2009.
2. Anis Allagui and Rolf Wüthrich. On the mechanism of nanoparticles synthesis by electrochemical discharges. In *ISE Satellite Student Regional Symposium on Electrochemistry*, Montreal, Canada, 2010.

Technical Reports

1. Anis Allagui and Guillaume Valette. Echauffement de reśistances électriques sur silicium. Technical report, Ecole Polytechnique de Nantes, Nantes, France, 2007.
2. Anis Allagui. Joule-thompson effect in gas pressure regulators. Technical report, RMG Regel + Messtechnik GmbH. by Honeywell, Kassel, Germany, 2007.
3. Anis Allagui. Gas pipe transient flow calculation. Technical report, Bryan Donkin RMG Ltd., by Honeywell, Chesterfield, England, 2006.
4. Anis Allagui. Acoustic pressure level in gas pressure regulators. Technical report, Bryan Donkin RMG Ltd., by Honeywell, Chesterfield, England, 2006.

Other Publications

1. Anis Allagui and Bevin Herrmann-Bell. Ask a Tunisian. Wronging Rights, January 2011.

2. Anis Allagui. *Design and publication of introduction brochures and e-Newsletters*. Allagui Business Solutions, Montreal, Canada.